ON THE MAGNETIC AND STRUCTURAL PROPERTIES OF Co AND Co-BASE NANOWIRE ARRAYS

Laura González Vivas

Advisors:Dr. Manuel Vázquez Villalabeitia and
Dr. Oksana Fesenko Morozova

UNIVERSIDAD AUTONOMA
DE MADRID

Department of Condensed Matter,
Universidad Autónoma de Madrid

Tutor: Dr. Juan José de Miguel Llorente

Manuscript submitted to reach the degree of Ph D in Physics,
2012 May

A Rosa Elvira y a Hector

Resumen

El conocimiento de los procesos de inversión de la imanación en sistemas de escala nanométrica es clave para el diseño de tecnologías avanzadas tales como medios de grabación magnética, espintrónica y dispositivos de detección y lectura de información. Los nanohilos magnéticos pueden tener importantes aplicaciones en los medios de comunicación avanzada de grabación en 3D, dispositivos lógicos y dispositivos MEMS (Sistemas-Micro-Electro-Mecánicos). Comúnmente los arreglos de nanohilos pueden ser preparados por diferentes técnicas de litografía. Sin embargo, la ruta alternativa electroquímica basada en auto ensamblajes de poros en substratos anodizados de alúmina, ha probado ser una herramienta poderosa y muy útil para la fabricación a bajo costo de arreglos ordenados de nanohilos con características magnéticas flexibles y optimizables.

La síntesis en plantillas ha demostrado recientemente ser una importante aproximación electroquímica para la fabricación de materiales en la nanoescala y una alternativa frente a otros métodos sofisticados como la microlitografía. Las plantillas auto ensambladas con ordenamiento hexagonal de alúmina (AAO) han sido seleccionadas en este trabajo para fabricar nanohilos magnéticos, una ruta eficiente para diseñar materiales con diferentes propiedades físicas. Las plantillas de alúmina son obtenidas mediante procesos electroquímicos comunes que permiten controlar y diseñar la geometría del substrato (diámetro y longitud de poros e inter-separación entre poros).

El presente trabajo trata del estudio magnético de arreglos de nanohilos de Co y con base en Co, crecidos en plantillas usando electrodeposición. Se ha hecho énfasis en el papel desempeñado por la estructura cristalina en las propiedades magnéticas de estos sistemas, y se consigue mostrar que dicha estructura cristalina depende de los parámetros particulares de fabricación y de la geometría de las plantillas. La modificación del pH en el electrolito de la electrodeposición de los nanohilos de Co, induce diferentes texturas de la fase cristalina *hcp*, lo que resulta en diferentes tipos de comportamiento magnético. Por otra parte, es posible modificar la anisotropía del sistema (sin cambiar significativamente el momento magnético de saturación) introduciendo elementos como el Ni y el Pd a través de una aleación con Co. Por otro lado, el cambio en las dimensiones de los nanohilos (como en su longitud y en su

diámetro) conlleva nuevamente a cambios en la estructura cristalina. Particularmente, para nanohilos con longitudes muy reducidas (del orden de 100 nm) se encuentra que la fase cristalina *fcc* es la dominante y que, junto con la anisotropía de forma determinan una imanación con el eje fácil en el eje de los nanohilos. En el caso de nanohilos con longitudes por encima de 1 μm, la fase cristalina dominante es la *hcp*, lo que resultará en una anisotropía magnetocristalina en el plano. Esto implicará una competición entre las anisotropías de forma y cristalina. Finalmente, en el caso de nanopilares de Co, se encuentra que para diámetros de 35 nm la fase dominante es la *fcc*. Por encima de este valor de diámetro la estructura cristalina será dominada por la fase *hcp*: el eje *c* se reorienta de paralelo a perpendicular al eje de los nanohilos cuando el diámetro supera los 44 nm.

El control en la fabricación de arreglos de nanohilos con una anisotropía magnética claramente definida constituye un mecanismo de control del proceso de inversión de la imanación. Lo anterior se ha discutido en este trabajo usando como base modelos analíticos, donde diferentes modos de inversión de la imanación, particularmente el modo de propagación de una pared transversal y de paredes de dominio tipo vórtice, son considerados frente al mecanismo de rotación homogénea coherente. Dichos modelos analíticos fueron usados con el fin de discutir y ajustar los resultados experimentales de la dependencia angular de la coercitividad en Co y en nanohilos de aleaciones basadas en Co. También se ha discutido la dependencia de las propiedades magnéticas de estos sistemas con la temperatura, con el objetivo de fortalecer la discusión sobre el papel que desempeñan las diferentes anisotropías.

Se han desarrollado cálculos micromagnéticos de la inversión de la imanación de distintos nanohilos de Co con diferentes relaciones de aspecto (longitudes desde 120 a 1000 nm y diámetros desde 35 a 75 nm). Con las simulaciones fueron obtenidos modos de inversión complejos dependiendo de la geometría y la estructura cristalina de los nanohilos. Las simulaciones muestran que los procesos histeréticos en la mayoría de los nanohilos envuelven la formación del estado vórtice. Para nanohilos con la fase *hcp* y el eje *c* transversal al eje del nanohilo, se reporta la formación de un vórtice central que se extiende a lo largo de toda su longitud en la remanencia. La desimanación continúa a través de mecanismos reversibles de rotación del nanohilo con excepción de su núcleo, el cual invertirá de ultimo.

Summary

The knowledge of magnetization reversal processes in nanoscale systems is relevant for the design of advanced technologies such as advanced magnetic recording media, spintronics and various sensing and reading devices. Magnetic nanowires can have important applications in advanced 3D recording media, logic and MEMS devices (Micro-Electro-Mechanical-Systems). Commonly, nanowires and their patterned arrays are prepared by different lithography techniques. However, the alternative electrochemical route profiting from self-assembled pores in anodic alumina templates has been proved to be very fruitful and a less-expensive reproducible method to prepare 3D ordered arrays of magnetic nanowires with tunable magnetic characteristics.

The template synthesis has recently been demonstrated to be an elegant chemical approach for the fabrication of nanoscale materials and an alternative to other sophisticated methods such as molecular beam epitaxy and microlithography. Self assembled ordered hexagonal nanoporous alumina templates (AAO) are chosen in this work for the fabrication of the nanowires, as an effective mean to create customized materials with designed physical properties. AAO templates are obtained by common electrochemical processes, with the aim to control their geometry (pore diameter, length and inter-pore distance). The latter is achieved by controlling the anodization parameters.

The present work deals with the magnetic study of Co and Co-base nanowire arrays prepared by template-assisted electroplating growth. The role played by the crystalline structure in the magnetic properties of Co and Co-base nanowire arrays is emphasized, and it is shown that the crystalline structure depends on the particular deposition and geometrical parameters. Modifying the electrolytic bath acidity, the pH, in the electrodeposition of Co nanowires, it is possible to induce different *hcp* Co phase textures, resulting in different types of magnetic behavior. Additionally, an alternative way to tune the magnetic anisotropy without extreme changes in magnetic saturation moment is through the addition of other metallic elements, such as Ni and Pd. On the other hand, by modifying the dimensions (i.e. length and diameter) of Co nanowires their crystalline structure is also modified. Particularly, for reduced lengths of nanowires, *fcc*-crystal phase is dominant which together with the shape anisotropy

usually results in longitudinal magnetization easy axis. For longer wires, *hcp*-crystal phase is formed, which determines the appearance of a magnetocrystalline anisotropy with nearly transverse orientation. In this latter case there is a competition between the shape and the crystalline anisotropies. For the case of Co nanopillars, it was found that for 35 nm of pore diameter the dominant crystal fase is the *fcc* one. Above this diameter the crystal structure is dominated by the *hcp* phase and a reorientation of the *c* axis is observed from out of plane to in plane for a pore diameter higher than 44 nm.

The controlled preparation of ordered arrays of magnetic nanowires with well-defined magnetic anisotropy constitutes a route to control the magnetization reversal process. This is discussed on the basis of analytical models, where different reversal modes, particularly propagating transverse or vortex-like domain walls were considered as alternatives to homogeneous coherent magnetization rotational mode. The analytical models were specially developed for the comparison with the experimental angular dependence of coercivity of Co and Co-based nanowire arrays. Also the temperature dependence of magnetic properties of Co and Co-base nanowire arrays were addressed in this study, with the aim to reinforce the discussion of the interplay of the different magnetic anisotropies. Finally, micromagnetic simulations of magnetization reversal of various Co nanowires with different aspect ratios (from 120 to 1000 nm in length, and 35 to 75 nm diameter) were performed.

Different complex reversal modes are obtained in micromagnetic simulations, depending on the geometry dimensions and the crystallographic structure. The simulations show that the hysteresis process in almost all nanowires involves the formation of the vortex. For long *hcp* nanowires with perpendicular c-axis, it is report the formation of central vortex which extends along its whole length at the remanence. The demagnetization proceeds with the reversible rotation of its shell and the consequent irreversible switching of the core.

Contents

Chapter 1: Introduction

1.1. Magnetic nanostructures. Magnetic nanowires

Within the last years, the nanomaterials science and technology represented one of the most attractive subjects for physicists, chemists, biologists, medical doctors and engineers. These materials present a special interest from the point of view of basic scientific understanding, but also their potential applications are very attractive. Additionally, nanomaterials and nanostructures represent the basis for the development of new technologies, systems and equipments. The continuous development of miniaturized devices for different applications is demanding novel multifunctional materials which can perform different functions simultaneously. Natural connections between physics, chemistry and life sciences are becoming much closer by means of nanotechnology, leading to complex and very useful applications.

Among the nanostructures, magnetic nanowires address both important fundamental and application aspects. Their small size and their unique and tunable properties make them attractive to be used to miniaturise conventional devices in a lot of application areas, such as optics, magnetic sensors, storage devices, thermoelectrics, as well as chemical and biological sensing.[1,2] In particular, a complete logic architecture may be constructed in spintronics (in which both the spin and charge of electrons are used for logic and memory operations) of modern high-density ultrafast data storage and logic devices involve field or current driven domain wall motion in magnetic nanowires. Domain walls in nanowires have also been suggested for use in a wide range of applications, such as atom trapping for quantum information processing.[2,3] Hence, the understanding of the growth modi and properties of ordered arrays of nanowires and nanoparticles is therefore, necessary for a variety of future applications.

Several lithography techniques are currently employed to grow magnetic nanowires, which are usually expensive and time-consuming. An alternative route to the fabrication of ordered arrays is via growth in ordered nanoporous templates, such as anodized aluminum oxide (AAO) or diblock copolymer templates which can be produced with self-ordering over a large scale.[4,5] The chemical template-based methods combined with high yield electrochemical deposition techniques, stand as a very versatile and non-expensive way to fabricate ordered arrays of magnetic nanowires, nanopillars, nanoholes or nanotubes with reproducible properties. The fabrication of such systems (specific stacks of metallic nanowires, both crystalline and amorphous, as well as wafer structures of nanowire arrays having different compositions and physical properties) by electrodeposition, mainly in polycarbonate and anodized aluminium templates, opened up new directions in what concerns the applications of such complex nanostructures in spintronics, engineering and bioengineering.

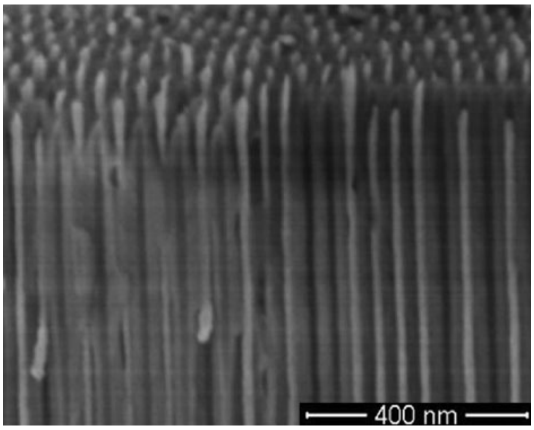

Fig.1.1. SEM image of an array of CoNi nanowire arrays inside an anodized alumina template.

1.2. About Co and Co-base nanowires

A number of studies have been reported on single element magnetic nanowire arrays, especially Ni, Fe and Co, their alloys (particularly, FeNi and CoFe) as well as magnetic/metallic multilayer systems.[6,8] Their magnetic behaviour is determined by the intrinsic magnetic character of individual nanowires together with their magnetostatic interactions, which are related to diameter and length of nanowires and to the porosity of the templates. For most purposes an effective magnetic anisotropy with easy axis parallel to the nanowires is desired. While strong shape anisotropy of the nanowires favours such magnetic configuration, interwires magnetostatic interactions result in a reduction of the effective longitudinal anisotropy. The latter translates into a decrease in the longitudinal coercive field and remanence. [9, 10] In the case of Ni and Fe nanowire arrays, typically few microns in length and tens of nanometers in diameter, the magnetic behaviour is mostly determined by the shape anisotropy that overcomes magnetocrystalline and magnetoelastic energy terms.[11] That mostly leads to an orientation of the magnetization along the nanowires axis. On the other hand, Co nanowires usually show a preferential hexagonal close packed (*hcp*) crystallographic structure, with the *c*-axis nearly perpendicular to the nanowire axis. [7, 9, 12] The presence of such a crystal phase originates a noticeable perpendicular magnetocrystalline anisotropy of the same order of magnitude as the shape anisotropy, resulting in a near energy balance, and consequently to a decrease in the effective anisotropy.

A first alternative to avoid such an unwished reduction could be to modify the electroplating parameters to achieve the growth of Co face center cubic (*fcc)* crystal phase which finally promotes an effective anisotropy parallel to the nanowires axis. Interestingly, the magnetic properties of Co nanowires can be tuned in addition by modifying the nanowires composition. For example, Co-base alloy nanowires can be grown where longitudinal anisotropy is promoted while still retaining significantly large saturation magnetization. This is the case, for example, of CoNi, CoPt or CoPd nanowire arrays.[13-16]

The magnetization reversal mode of nanowire arrays with diameter in the range of tens of nanometers has been addressed in previous works.[17-20] In many of these reports, both homogeneous coherent and curling rotational mechanisms are considered following micromagnetic classical references,[21-23] and particularly for the case of magnetically hard systems.[16] The applicability of various rotational modes depends on the geometric characteristics of the nanowires, being the experimental study of the angular dependence of coercivity possibly the most fruitful method to determine the actual magnetization mechanism. While the role of shape anisotropy and magnetostatic interactions has been thoroughly investigated in many articles, and still is not fully a closed issue, the influence of the crystalline structure has not been sufficiently addressed.

The study of the reversal mode in Co and Co-base nanowires is particularly exciting because their crystalline structure introduces a very significant energy term that makes certainly more complex the magnetization reversal mechanism. The crystal structure is confirmed here to change with length of Co nanowires as well as by adding particular metallic elements. This work collects experimental and modelling results for the magnetization reversal of Co and Co-base nanowire arrays by using classical studies in micromagnetism, trying to unveil the actual magnetization reversal process.

1.3. Ferromagnetic properties of nanowires

Magnetization hysteresis loops, which display the magnetic response of a magnetic sample to an external field, have been widely used to characterize the behavior of nanostructured magnetic materials. Fig. 2.1 shows typical magnetization hysteresis loops with the applied magnetic field parallel (//) and perpendicular ($\perp$) to the nanowire axis for an array of Co nanowires. The characteristic features of the hysteresis loop are dependent on the material, the size and shape of the entity, the microstructure, the orientation of the applied magnetic field with respect to the sample, and the magnetization history of the sample.

For arrays of nanowires, the hysteresis loop may also depend on interactions between individual wires. The common parameters used to describe the magnetic properties are the saturation magnetization M_{sat} (when all magnetic moments in the material are aligned in the same direction), the remanent magnetization M_r (the magnetization M at $H = 0$), the coercivity H_c (the applied field at M becomes zero), and the saturation field H_{sat} (the field needed to reach the saturation magnetization). Another important parameter in describing the magnetic behavior is the switching field H_{sw}, which is the field needed to switch the magnetization from one direction to the opposite direction. The switching field H_{sw} can be defined as the field in which the slope of the M–H loop is maximum (i.e., $d^2M/dH^2 = 0$). For an array of nanoparticles or nanowires, there is likely to be a distribution of switching fields due to small differences in size, shape, or microstructure. In this case, H_{sw} characterizes nanowires with a switching field near the peak in the distribution. In many cases the switching field is symmetric (e.g., gaussian), and hence $H_s = H_c$.

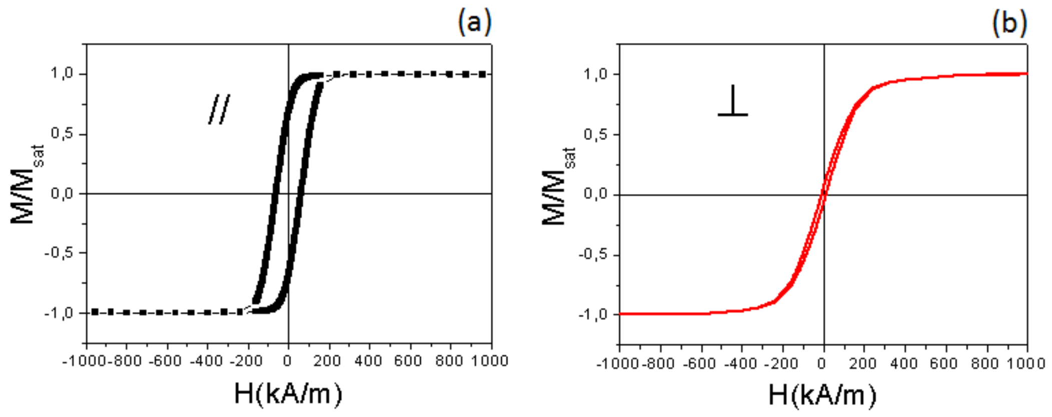

Fig.2.1. Hysteresis loops for an array of Co nanowire 35 nm diameter and 2.5 μm long with the applied field (a) // and (b) ⊥ to the wire axis.

As the temperature is increased, thermal fluctuations can overcome the ordering of the magnetic moments in a ferromagnetic material. The transition between ferromagnetic and paramagnetic behavior occurs at the Curie temperature T_c, which is a property of the material and is dependent on sample dimensions. For magnetic nanowires, all of these characteristic magnetic properties can be controlled by choice of material and dimensions. In principle, magnetization hysteresis loops for an arbitrary entity can be calculated by minimizing the total free energy in the presence of an external field. The state of magnetization is determined from the eigenvalue of the magnetization vector configuration that minimizes the total system energy.[18] The total energy E can be expressed as

$$E = E_{ex} + E_H + E_{EA} + E_{ca} + E_D \,, \tag{1.1}$$

where E_{ex} is the exchange energy, E_H is the Zeeman energy, E_{EA} is the magnetoelastic energy, E_{ca} is the crystalline anisotropy energy, and E_D is the magnetostatic energy (demagnetization energy).

The exchange energy is related to the interaction between spins that introduces magnetic ordering and can be written as

$$E_{ex} = -2\sum_{i>j} J_{ij} S^2 \cos\theta_{ij} \,, \tag{1.2}$$

where J_{ij} is the exchange integral, S is the spin associated with each atom, and θ_{ij} is the angle between adjacent spin orientations. For ferromagnetic materials, J is positive, and the minimum-energy state occurs when the spins are parallel to each other ($\theta_{ij} = 0$). Exchange interactions are inherently short-range and can be described in terms of the exchange stiffness constant A. The exchange stiffness is a measure of the force acting to keep the spins aligned and is given by $A = JS^2c/a$, where c is a geometric factor associated with the crystal structure of the material ($c = 1$ for a simple cubic structure, $c = 2$ for a body-centered cubic structure, $c = 4$ for a face-centered cubic structure, and $c = 2\sqrt{2}$ for a hexagonal close packed structure), and a is the lattice parameter.

The Zeeman energy is often referred to as the magnetic potential energy, which is simply the energy of the magnetization in an externally applied magnetic field. The Zeeman energy is always minimized when the magnetization is aligned with the applied field; it can be expressed as

$$E_H = -\boldsymbol{M} \cdot \boldsymbol{H}, \tag{1.3}$$

where **H** is the external field vector and **M** is the magnetization vector.

The magnetoelastic energy is used to describe the magnetostriction effect, which relates the influence of stress, or strain, on the magnetization of a material.

1.3.1 Shape anisotropy

The magnetization of a spherical object in an applied magnetic field is independent of the orientation of the applied field. However, it is easier to magnetize a nonspherical object along its long axis than along its short axis. If a rod-shaped object is magnetized with a north pole at one end and a south pole at the other, the field lines emanate from the north pole and end at the south pole. Inside the material the field lines are oriented from the north pole to the south pole and hence are opposed to the magnetization of the material, since the magnetic moment points from the south pole to the north pole. Thus, the magnetic field inside the material tends to demagnetize the material and is known as the demagnetizing field H_d. Stated formally, the demagnetizing field acts in the opposite direction from the magnetization M which creates it, and is proportional to it, namely

$$H_d = -N_d \tag{1.4}$$

where N_d is the demagnetizing factor and is dependent on the shape of the body, but can only be calculated exactly for an ellipsoid where the magnetization is uniform throughout the sample. The magnetostatic energy E_D associated with a particular

$$E_D = \frac{1}{2} N_d \mathbf{M}^2_s , \tag{1.5}$$

For a general ellipsoid with $c \geq b \leq a,$ where a, b, and c are the ellipsoid semi-axes, the demagnetization factors along the semi-axes are N_a, N_b, and N_c, respectively. The demagnetization factors are related by the expression $N_a + N_b + N_c = 4\pi$.

1.3.2. Magnetocrystalline anisotropy

In a magnetic material, the electron spin is coupled to the electronic orbital (spin-orbital coupling) and influenced by the local environment (crystalline electric field). Because of the arrangement of atoms in crystalline materials, magnetization along certain orientations is energetically preferred. The magnetocrystalline anisotropy is closely related to the structure and symmetry of the material. For a cubic crystal, the anisotropy energy is often expressed as

$E_{ca} = K_0$

$+ K_1(\cos^2\theta_1 \cos^2\theta_2 + \cos^2\theta_2 \cos^2\theta_3 + \cos^2\theta_3 \cos^2\theta_1)$

$$+ K_2 cos^2\theta_1 cos^2\theta_2 cos^2\theta_3 + \ldots , \qquad (1.6)$$

where K_0, K_1, K_2, … are constants and θ_1, θ_1, and θ_1 are the angles between the magnetization direction and the three crystal axes, respectively. K_0 is independent of angle and can be ignored since it is the difference in energy between different crystal orientations that is of interest. In many cases, terms involving K_2 are small and can also be neglected.

The magnetocrystalline anisotropy energy associated with a hexagonal close-packed crystal is often expressed as

$$E_{ca} = K_0 + K_1 \sin^2\theta + K_2 \sin^4\theta, \qquad (1.7)$$

where K_0, K_1, and K_2 are constants and θ is the angle between the magnetization direction and the *c*-axis. If $K_1 > 0$, the energy is smallest when $\theta = 0$, i.e., along the *c*-axis, so that this axis is the easy axis. If $K_1 < 0$, the basal plane is the easy axis. As a result of the symmetry of the hexagonal close-packed lattice, the magnetocrystalline anisotropy is a uniaxial anisotropy. Examples of K_1 for various materials are given in Table 1.

Table 1. Values of the magnetocrystalline anisotropy energy constant K_1.

Material	K_1 *(J/m3)*
hcp Co	4.5e5
fcc Co	6.8e4
fcc Ni	-4.5 e3

1.4. Thesis Outline

After introductory sections on the state of the art (Chapter 1) and experimental techniques used in the work (Chapter 2), the study collects experimental aspects of electrochemical preparation and general structural and magnetic characterization in Chapter 3. Particular attention is paid to the influence of various parameters as solution pH during electroplating, geometry dimension (i.e., length and diameter of nanowires) or the addition of other elements (i.e., Ni or Pd) to determine the *hcp* or *fcc* crystalline structure and texture, and subsequently on the resulting magnetocrystalline anisotropy. Such anisotropy will define the magnetization reversal process, as it is discussed in Chapter 4, through consideration of analytical calculations where different reversal modes, particularly propagation of transverse or vortex-like domain walls are considered as an alternative to homogeneous coherent magnetization rotational mode. This is particularly developed to analyze and compare with the experimental angular dependence of coercivity of Co and Co-base nanowrie arrays. Additional experimental studies on the temperature dependence of coercivity are discussed in Chapter 5 together with the temperature dependence of anisotropic magnetoresistence in particular nanowire arrays. The experimental section includes the study of indivual Co nanowires removed from the template where last but promising first studies are introduced on their magnetic and magnetotransport properties. Chapter 6 is finally dealing with the more rigorous micromagnetic analysis of magnetization reversal of various Co nanowires with different aspect ratio (from 120 to 1000 nm in length, and 35 to 75 nm diameter). Different complex reversal modes are concluded depending on those geometry dimensions and the crystallographic structure. The simulations show that the hysteresis process in almost all nanowires involves the formation of the vortex. For long *hcp* nanowires with perpendicular c-axis, it is report the formation of central vortex which extends along its whole length at the remanence. The demagnetization proceeds with the reversible rotation of its shell and the consequent irreversible switching of the core.

The study has been carried out at the Laboratories of the Group of Nanomagnetism and Magnetization Processes and the Group of Magnetic Simulations at the Institute of Materials Science of Madrid, CSIC. Nevertheless, we should emphasize the number and intensity of collaborations with other groups. In this regard, we want to express our gratitude to the team at Porto University (Prof. J.P. Araujo and Dr. D. C. Leitao) for their support in the preparation and magnetotransport properties measurements; to the team in University of Oviedo (headed by Dr. V. M. Prida) for their help in the preparation of Co-base nanowire arrays and the temperature dependent magnetic properties; to the team at the University of Santiago de Chile (Prof. J. Escrig and Dr. Altbir) for their support in the analytical calculations and modeling; to the team at the Institute of Nanotechnology of Aragón (Prof. J.M. de Teresa) for their support in the final study on individual Co nanowires.

1.5. References

[1]B. Bhushan (ed.), Handbook of Nanotechnology (Springer-Verlag, Berlin/Heidelberg/New York, 2004).

[2] D. Atkinson, A. Allwood, G. Xiong, M. D. Cooke, C. C. Faulkner, and R. P. Cowburn, Nature Mater. **2**, 85 (2003).

[3] S-W. Jung, W. Kim, T-D Lee, K-J. Le, and H-W. Lee, Appl. Phys. Lett. **92**, 202508 (2008).

[4]A. P. Robinson, G. Burnell, M. Hu, and J. L. MacManus-Driscoll, Appl. Phys. Lett. **91**, 143123 (2007).

[5] M. Vazquez, and L. G.Vivas, Phys. Status Solidi B **248**, 2368 (2011).

[6] P. M. Paulus, F. Luis, M. Kro¨ ll, G. Schmid, and L. J. de Jongh, J. Magn. Magn. Mater. **224**, 180 (2001).

[7] H. Zeng, R. Skomski, L. Menon, Y. Liu, S. Bandyopadhyay, and D. J. Sellmyer, Phys. Rev. B **65**, 134426 (2002).

[8] M. Vazquez, M. Hernandez-Velez, A. Asenjo, D. Navas, K. Pirota, V. Prida, O. Sanchez, and J. L. Baldonedo, Physica B **384**, 36 (2006).

[9] Y. Ren, Q. F. Liu, S. L. Li, J. B. Wang, and X. H. Han, J. Magn. Magn. Mater. **321**, 226 (2009).

[10] J. Escrig, D. Altbir, M. Jaafar, D. Navas, A. Asenjo, and M. Vazquez, Phys. Rev. B **75**, 184429 (2007).

[11] K. Nielsch, R. B. Wehrspohn, J. Barthel, J. Kirschner, S. F. Fischer, H. Kronmu¨ ller, T. Schweinböck, D. Weiss, and U. Gösele, J. Magn. Magn. Mater. 249, 234 (2002).

[12] J. M. García, A. Asenjo, M. Vázquez, P. Aranda, and E. Ruiz-Hiztky, J. Appl. Phys. **85**, 5480 (1999).

[13] S. Thongmee, H. L. Pang, J. B. Yi, J. Ding, J. Y. Lin, and L. H. Van, Acta Mater. **57**, 2482 (2009).

[14] S. Shamaila, R. Sharif, S. Riaz, M. Ala, M. Khaleed-ur- Rahman, and X. F. Han, J. Magn. Magn. Mater. **320**, 1803 (2008).

[15] N. H. Hu, H. Y. Chen, S. Y. Yu, L. J. Chen, J. L. Chen, and G. H. Wu, J. Magn. Magn. Mater. **299**, 170 (2006).

[16] X. Y. Zhang, L. H. Xu, J. Y. Dai, and H. L. W. Chan, Physica B **353**, 187 (2004).

[17] K. Nielsch, R. B. Wehrspohn, J. Barthel, J. Kirschner, U. Gosele, S. F. Fischer, and H. Kronmüller, Appl. Phys. Lett. **79**, 1360 (2001).

[18] L. Sun, Y. Hao, C.-L. Chien, and P. C. Pearson, IBM J. Res. Dev. **49**, 79 (2005).

[19] X.-T. Tang, G.-C. Wang, and M. Shima, J. Magn. Magn. Mater. **309**, 188 (2007).

[20] S. Goolaup, N. Singh, A. O. Adeyeye, V. Ng, and M. B. A. Jalil, Eur. Phys. J. B **44**, 259 (2005).

[21] W. F. Brown, Jr. Micromagnetics (Krieger Pub. Co, New York, 1978).

[22] A. Aharoni, Introduction to the Theory of Ferromagnetism (Oxford University Press, Oxford, 1996) Chap. 9.

[23] E. H. Frei, S. Shtrikman, and D. Treves, Phys. Rev. **106**, 446 (1957).

Chapter 2: Experimental Part

In this Chapter we present a summary of the experimental techniques that have been used throughout this PhD work.

2.1. Nanoporous alumina templates and electrodeposition

2.1.1. Self-ordered honeycomb nanoporous anodic alumina oxides.

The synthesis procedure of nanoporous anodic alumina templates, AAO, involves a two-step anodization process of high purity (99.999 %) aluminium films in different acidic electrolytes.[1] This original two-step anodization method allows one to fabricate alumina membranes with large area densities of honeycomb nanometric porous structures by means of a low cost procedure under the appropriated conditions. In this way, hexagonally self-ordered patterns of pores within micrometric-size geometrical domains can be obtained. Closed-packet cells and centred pores self-assemble in a local hexagonal arrangement, where the diameter and depth of each pore, as well as the inter-spacing distance between adjacent pores can be also controlled by changing the anodization conditions.[2]

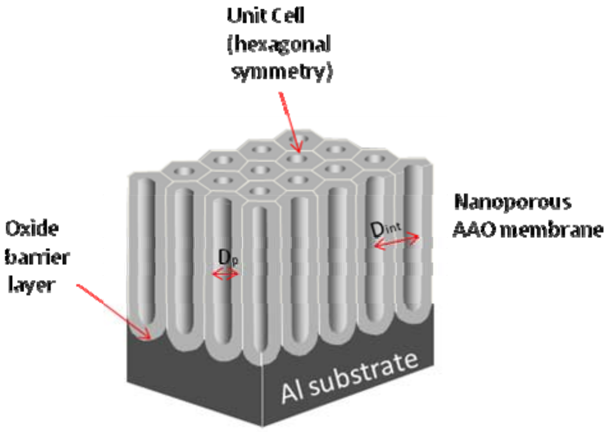

Fig. 2.1. Sketch of a nanoporous anodic alumina template (AAO) on aluminium substrate, showing the main parameters of the array: pore diameter, Dp, interpore distance, Dint, and the unit cell of the nanoporous alumina membrane. It can be seen also the oxide barrier layer.

In order to fabricate the nanoporous AAO with hexagonal ordering, previous to the anodization process, highly-pure (99.999 %) Al foils are first degreased, preannealed to remove mechanical stresses and enhance the grain size, and subsequently they are electropolished by applying a constant voltage for reducing the surface roughness and to create more homogeneous surfaces previously to the anodization beginning.[3] The anodization processes are always carried out at low temperatures to prevent attacks of the acidic electrolyte of the pores structure (typically between +10-0 ºC), inside an anodization cell by applying a constant voltage [see Fig. 2.2(a)]. In a first step of the long-period anodization process, the application of an electric field leads to the development of a so-called compact barrier layer of alumina, which consists of a closed thin oxide layer on the aluminium surface. In this initial stage of the anodization process, the pores grow randomly distributed on the alumina surface. The appearance of homogeneous pores during anodization depends on the oxidation rate of aluminium and the field-enhanced oxide dissolution rate at the oxide/electrolyte interface.[4] Owing to the decreasing current with the increase of the thickness of the barrier layer, the formation of pores is initiated at defect sites continuously growing during the ongoing anodization, as can be experimentally seen in the current transients shown in figures 2.2.(a) and (b).

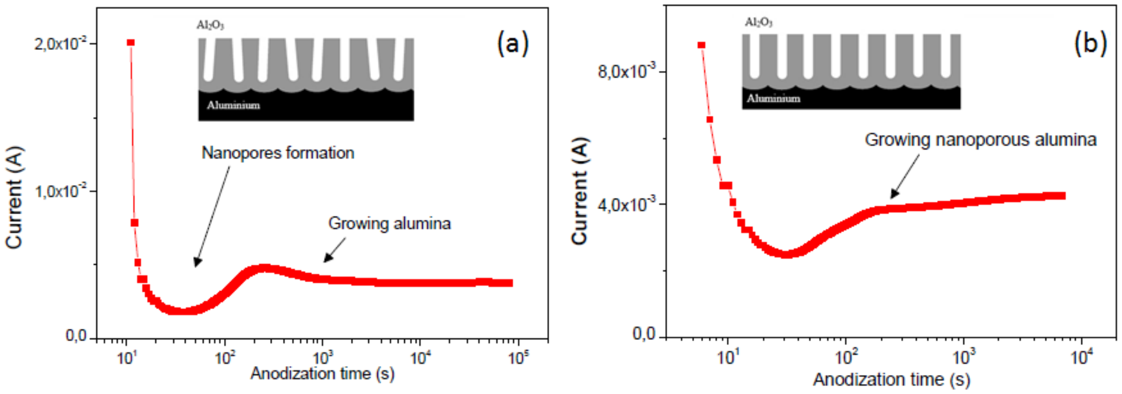

Fig. 2.2. Typical current transient during the nanoporous alumina membranes formation. (a) First and (b) second current-time curves during the anodization processes of alumina membranes potentiostatically anodized. The respective insets show the nanoporous structure grown after each anodic step.

The lattice parameter of the hexagonally ordered nanopores array depends on the first anodization conditions, such as anodization voltage and electrolyte. The size of crystalline hexagonal units is typically limited to domains of the order of a few μm^2, which is also controlled by the duration of the first anodization time and low temperature.[5] The optimal voltage depends on the electrolyte used for anodization. For example, the optimal voltage for long range ordering is 25 V in sulphuric acid, 40 V in oxalic acid and 195 V in phosphoric acid electrolyte, giving rise to 65, 105 and 500 nm lattice parameter and nanopore diameters of 25, 35 and 180 nm, respectively.[5,6]

The second step of anodization process at the same anodization conditions is carried out using the pre-structured aluminium surface as template, where the ordered concave sites formed during the first anodization process serve as the initial points to form a highly ordered alumina nanopores array with desired pore diameter and spacing. Both, the pore diameter and the interpore spacing are proportional to the anodizing voltage with constants of 1.3 nm/V and 2.5 nm/V, respectively.[7] As a rule of thumb, the pore diameter can be estimated to be about 30% of the interpore spacing.[8] A subsequent pore widening by an isotropic chemical etching procedure and thinning barrier layer process can be performed by a exponentially decreased of the potential, originating a reproducible tree-like branched structure known as dendrites.[9] The length of the nanopores is also controlled by the second anodization time. Thus, the whole array can be approached to a regular lattice of well-aligned and parallel grown nanopores with hexagonal symmetry, as it can be seen illustrated in the sketch of Fig. 2.1.

An explanation about the mechanism of the self-organized growing of the nanopores during the aluminium oxide expansion can be considered to obey the resulting mechanical stresses originated at the metal/oxide interface during the moderated ratio of the alumina volume expansion (of the order of 1.2-1.4), occurred under optimal conditions of the anodic oxidation process, which are proposed to cause repulsive forces between the neighboring nanopores, leading to self-organized formation of hexagonal pore arrays. During the anodic oxidation of the aluminium starting substrate, the oxygen containing ions (O^{2-}/OH^-) migrate from the electrolyte through the oxide layer at the pore bottom, while the Al^{3+} ions which simultaneously drift through the oxide layer are lost into the solution at the oxide/electrolyte interface. The last fact has been founded to be a prerequisite for porous oxide growth, whereas Al^{3+} ions reaching the oxide/electrolyte interface contribute to the oxide formation in form of the barrier oxide growth. Since the oxidation takes place at the entire pore bottom simultaneously; the alumina can only be expanded in the vertical direction, so that the pore walls are pushed upwards. Due to this mechanism, the nanopores are grown perpendicular aligned to the aluminium substrate with equilibrium of field-enhanced oxide dissolution at the oxide/electrolyte interface and the aluminium oxide growth at the metal/oxide interface.

2.1.2. Experimental set-up for anodization

The implemented experimental setup used for anodization has been developed in the Laboratories of the Group of *Nanomagnetism and Magnetization Processes*, ICMM. The facility implemented consists of chemical work benches and anodization/electrodeposition infrastructures. These facilities allow the growth of nanoporous templates through electrochemical oxidation (anodization) of Al foils for the preparation of nanostructures such as nanowires and nanotubes by chemical-based template-assisted-methods.

The anodization system implemented is a very simple and low cost but very effective experimental set-up (Fig. 2.3). The homemade anodization cell essentially consists of a teflon cylindrical container. The cell is non-reactive to the used acidic solutions, providing at the same time good thermal insulation for the refrigerated electrolyte (Fig. 2.4). The Al foils are pressed with an O-ring against the bottom of the cell, ensuring a leak-free proof system. While the top side of the Al foil is in direct contact with the electrolyte, the other side is in direct contact with a Cu-plate. The latter acts simultaneously as anode (positive electrical contact) and cooling plate, being constantly cooled by a refrigeration circuit. The cathode, an inert Pt mesh (99.9 % pure), is placed ~ 10 mm away from the sample acting as cathode. In order to improve the homogeneity of the solution (temperature, pH, and concentration gradients) one has a mechanical electrically driven stirrer typically adjusted to provide between 200 - 250 rpm. The stirrer consists of a Faulhaber Minimotor (Ref. 1624E024S 15/3) coupled to a plastic fan. The external DC voltage for the electrochemical process is provided by a Keithley 2004 Sourcemeter. This instrument provides two independent channels enabling current measurements while a constant voltage is applied, both being only limited by the characteristics of the equipment itself (220 V/1 A). A LabView application was developed to control automatically the experiment, monitoring the current density evolution during the anodization procedure within the user-defined conditions (anodization time and voltage).

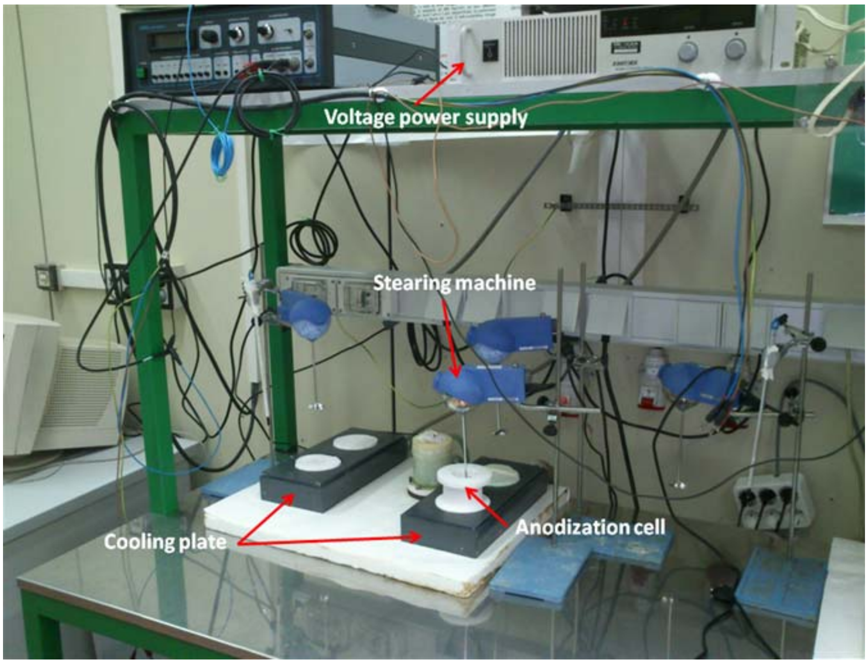

Fig. 2.3. Anodization setup implemented at the ICMM facilities.

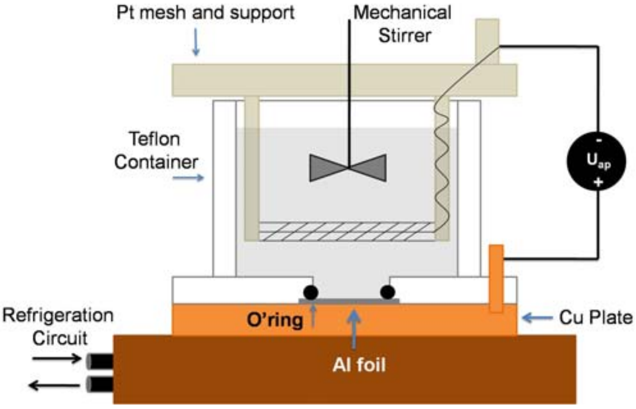

Fig. 2.4. Schem of an anodization cell implemented at the ICMM facilities.

2.1.3. Electrodeposition

Electrochemical deposition of nanowires into the AAO templates is a low-cost and efficient technique for growing high-density magnetic nanowire arrays with an ultrahigh nanowire aspect ratio, controllable nanowire diameters, and up to centimeter-long sample sizes.[10] Electroplated nanowires can have structures quite different from that of their bulk counterpart due to the size confinement by the AAO pores and the details of the electrochemical deposition processes. For example, although bulk Co has a hexagonal close-packed (*hcp*) structure at room temperature and a face centered cubic (*fcc*) structure above 422 ^{o}C, both *hcp* and *fcc* have been found in electroplated Co nanowires at room temperature.[11, 12]

Electrodeposition of magnetic metals can be performed by different modes as: constant current pulses,[13] constant voltage pulses,[3] current-voltage mixture pulses,[14] and by alternating pulses.[15] In this work, the nanowires were grown inside alumina nanoporous membranes by both constant current and voltage pulses.

The electrolytes of Watts bath used for the electrodeposition were:

Co: 300 g l^{-1} $CoSO_4.7H_2O$ + 45 g l^{-1} H_3BO_3

CoPd: 0.51 gl^{-1} $PdCl_2$ + 25 gl^{-1} $CoSO_4{\cdot}6H_2O$ + 21 gl^{-1} H_3BO_3 + 1.5 ml of HCl 37%
For less concentrations of Pd, the pH of the solution was adjusted to 7.0 with diluted ammonia. The actual role of ammonia in the solution is not only to adjust the pH but also to bring the deposition potentials of Pd^{2+} and Co^{2+} together due to the complexation of Pd^{2+}:[16]
Alternatively, the pH of the same solution was adjusted to 4 with diluted NaOH. Since Pd^{2+} ions are not complexed in the later solution, higher Palladium concentrations were expected in the nanowires electrodeposited with this second electrolyte. The CoPd nanowires were prepared in collaboration with the team from University of Oviedo (headed by Dr. V. M. Prida).

$Co_{80}Ni_{20}$: 150 gl^{-1} $CoSO_4{\cdot}7H_2O$ + 150 gl^{-1} $NiSO_4{\cdot}7H_2O$ + 30 gl^{-1} H_3BO_3
$Co_{50}Ni_{50}$: 30 gl^{-1} $CoSO_4{\cdot}7H_2O$ + 270 gl^{-1} $NiSO_4{\cdot}7H_2O$ + 30 gl^{-1} H_3BO_3
Ni: 300 gl^{-1} $NiSO_4{\cdot}7H_2O$ + 30 gl^{-1} H_3BO_3

Au: commercial gold-plating solution (Orosene 999)[17]
Cu: 130 gl^{-1} $CuSO_4 \cdot 7H_2O$ + 30 gl^{-1} H_3BO_3

Except for the case of CoPd alloy, the pH value of the electrolytes was adjusted adding few drops of 0.5 M H SO solution or 1 M NaOH solution.

a) Pulsed electrodeposition

In general, AAO membranes with pore lengths smaller than 2 μm can be very difficult to handle when detached from the underlying aluminum substrate. Using the pulsed electrodeposition method, it is possible to grow nanowires inside the pores of AAO membranes while avoiding the removal of them from the underlying aluminum substrate. However, the presence of an insulating alumina barrier-layer at the bottom of each nanopore prevents a direct deposition of material. Therefore, a suitable chemical process is required in order to reduce the thickness of this barrier-layer, resulting in the formation of dendrites at the bottom of pores that enable their subsequent filling with metals. In order to avoid the effect of the dendrites on the magnetic properties of nanowires, they can be filled with a non-magnetic metallic element as Au or Cu. Subsequently, the cylindrical main pores can be filled with metallic magnetic nanowires.

For the electrodepositions, the pulse sequence consisted in an 8 ms long galvanostatic pulse followed by a positive potentiostatic pulse of 4.5 V during 2 ms. This positive voltage is applied in order to discharge the thin and electrically isolating Al_2O_3 barrier layer present at the AAO/Al interface. A long rest time of 700 s during which no current was applied to the sample is used between consecutive electrodeposition steps in order to restore the amount of metals ions in the metal/electrolyte interface. In order to obtain different composition alloys, the current density or the components concentrations were varied. Table 1 resumes the current density applied during the deposition process.

Table 1: Synthesis conditions for electrodeposition of the nanowires.[16]

Electrolyte composition	*Current density $(mA.cm^{-2})$*
Co, Ni, Cu, CoNi-alloys	30
Au	70
$Co_{88}Pd_{12}$, pH 7	26
$Co_{74}Pd_{26}$, pH 7	13
$Co_{56}Pd_{44}$, pH 4	26

Fig. 2.4 shows the voltage evolution whereas the negative current pulse was applied. In this figure three zones can be observed in which the fully filling of the nanopores is reached at the third zone. The experimental set-up used, which is the same as the anodization apparatus, consists of the electrodeposition (a teflon container where at the bottom we place our substrate, copper working electrode), facing directly an inert Pt mesh (counter electrode). As an external current source we use a Keithley 2004 Sourcemeter controlled by a LabView application. This equipment enables a sequential application of current and voltage pulses.

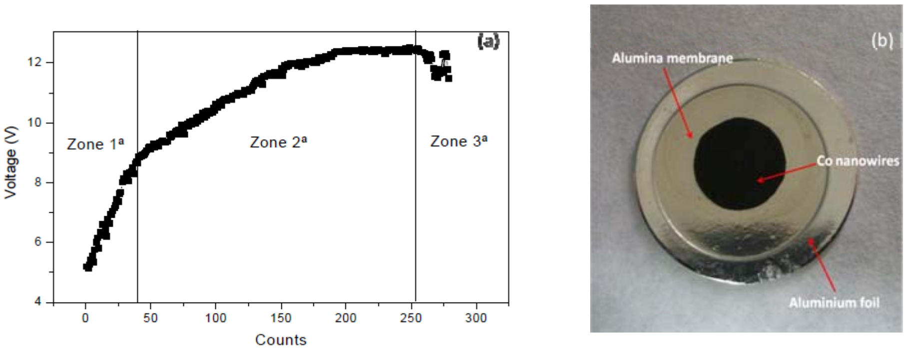

Fig. 2.5. (a) Voltage value measured during the negative current pulse of the electrodeposition. (b) Top view of a Co nanowires sample inside the AAO template.

b) Potentiostatic mode

In order to obtain arrays of nanowires with lengths above 5 microns or multilayered nanowires, a suitable method of electrodeposition is the potentiostatic mode. Through this method, it is possible to grow several micron nanowires after few minutes of electroplating. Also, multilayered structures can be electrodeposited by switching between the deposition potentials of the constituents.[16]

For the electrodeposition, the nanopores were opened at the bottom by chemical etching of Al in an aqueous solution of 0.2 M $CuCl_2$ and 4.1 M HCl at room temperature, and chemical dissolution of the alumina bottom barrier layer in 0.5 M phosphoric acid. (Pore widening using phosphoric acid was also performed in selected samples to obtain different pore diameters). A thin Au layer (~ 100 nm) was then sputtered on the backside of the membrane to serve as the working electrode in a three-electrode cell. A Pt mesh and Ag/AgCl (in 4 M KCl) were used as the counter and reference electrodes, respectively. The electrodeposition of Co nanowires was performed at -1 V using a Solartron 1480 MultiStat.

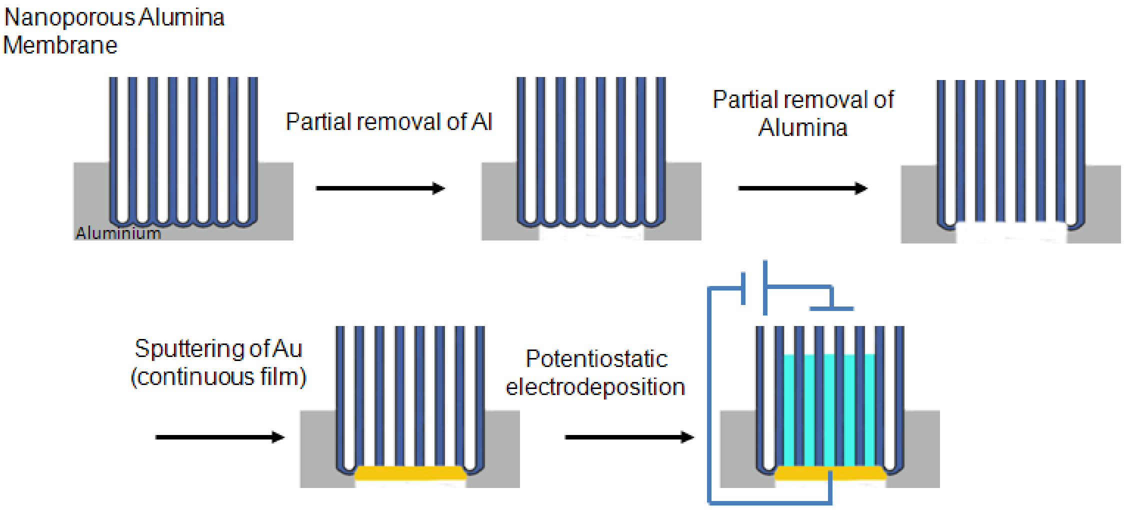

Fig. 2.6. Scheme of the process for electrodeposition by potentiostatic mode.

2.2. Morphology and topography

2.2.1. Scanning Electron Microscopy (SEM)

The electron microscopy is based on the use of an accelerated electron beam in order to examine and obtain samples images of different materials. The wave function associated to the each electron has a wavelength $\lambda = h/(m\,v)$ (where m is the mass of the electron; v the velocity of the electron; and h is the Planck's constant) given by the de Broglie relation. One notices that λ decreases with the increase of the kinetic energy, being less than 0.1 nm under the ordinary conditions of operation in electron microscopy. Thus, it is possible, without appreciable effects of diffraction, to achieve an extremely small electron beam diameter and angular aperture, allowing to obtain a much higher resolving power and field depth than those obtained with light microscopy. The electronic microscopic system is based on the production of an electron beam with controlled kinetic energy and the use of a electrostatic and magnetic lenses (electric and magnetic fields with proper conformation and intensity) to electron beam setting and focusing. The conditions for the electron beam generation and propagation require the use of high-vacuum chambers, which impose some restrictions on the characteristics of the samples for observation. Depending on the characteristics of the lighting system (the incident electron beam generation and guidance control), the mode to detect radiation emerging from the sample (under the electron beam impact) and the image construction, one can consider several methods of electron microscopy.

The morphology of the nanowires was studied by scanning electron microscopy (SEM). SEM yields images with a resolution from a few millimeters down to 5 nm. In a SEM microscope, the surface of the sample is irradiated with high energy electrons. A set of magnetic lenses moves the focused beam back and forth across the specimen. As the electron beam hits each spot on the sample, both electrons and photons are emitted by the specimen surface, and their intensity is used to form the SEM image when all the spots are convoluted. The signals most commonly used are the secondary electrons, the backscattered electrons and X-rays. Secondary electrons are specimen electrons that obtain energy from inelastic collisions caused by the incident beam electrons. They are defined as electrons emitted from the specimen with energy less than 50 eV. On the other hand, backscattered electrons are the primary incoming beam electrons that experience an elastic backscattering with sample electrons. The number of backscattered electrons will produce a contrast depending on the mean atomic number of the illuminated spot. That way, 2D phase analysis can be performed comparing the different contrasts. SEM was employed to characterize samples with surface and cross-section views using a FEI Nova Nano 230 high resolution scanning electron microscope (SEM), located at the laboratories of the Group *New Architectures in Materials Chemestry,* ICMM.

2.2.2. Electron Diffraction Spectroscopy (EDS)

Features observed by SEM may then be immediately analyzed to obtain the corresponding elemental composition, using the Energy Dispersive Spectroscopy (EDS) analysis of X-rays. The electron beam interacts with the sample atoms through the ionization of an inner shell electron. The resultant vacancy is filled by an outer electron, which releases its energy with the emission of Auger electrons or X-rays. Since these emissions are specific for each element, the composition of the material can be deduced. This can be used to provide qualitative and/or quantitative information about the elements present at different points of the samples, and it is also possible to map the concentration of an element as a function of the position.

2.3. X-Ray Diffraction (XRD)

The X-ray diffraction (XRD) allows one the identification and structural characterization of crystalline nanostructures. The X-rays interact with the electrons in the atoms, when passes through the sample, resulting in scattering of the radiation. The wavelength of the X-ray radiation has values of 1 Å in the order of the lattice parameters in crystalline solids. Thus, if the distance between the atoms is close to the wavelength of the X-rays, interference of the scattered waves in these solids will occur and form a diffraction pattern with constructive and destructive interferences. The X-rays are scattered at characteristic angles based on the spaces between the atomic planes defining their crystalline structure. Since most crystals have several sets of planes passing through their atoms, each of them has a specific interplanar distance and will originate a characteristic angle of diffracted X-rays. The intensity maximum of the diffraction pattern will appear for scattering directions which are univocally related with specific reciprocal lattice vectors of the solid. These directions determine the so called Bragg reflections (giving Bragg peaks in the spectra) and a set of Miller indexes (*hkl*) can be assigned to them. The relationship between wavelength (λ) atomic spacing (d_{hkl}) and diffraction angle θ, is given by the Bragg's law:

$$n \lambda = 2d_{hkl} \sin \theta, \tag{2.1}$$

where λ is the wavelength of the incident wave, d_{hkl} is the distance between the planes with the miller indexes (*hkl*), and θ the angle formed by the propagating vectors of the incident and scattered waves. From the broadening it is possible to determine an average crystallite size, in Å, by Debye-Scherrer formula:

$$D_{hkl} = k \frac{\lambda}{\beta \cos\theta}, \tag{2.2}$$

where k = 0.8 - 1.39 (usually close to the unity e.g. 0.9, considering spherical grains), λ the wavelength of the radiation λ_{Cu} = 1.54056 Å, β is the full width at half maximum, or half-width in radians and θ is the position of the maximum of diffraction. The XRD spectra were performed with a X'Pert PRO X-ray diffractometer using filtered Cu Ka radiation, located at the laboratories of the *Servicio Interdepartamental de Investigación,* SIDI, UAM.

2.4. Magnetization. Vibrating Sample Magnetometer (VSM)

The vibrating sample magnetometer (VSM) technique to measure the magnetic properties of materials was first developed by S. Foner in 1956,[18] and has been accepted as a standard approach worldwide. It has been proved to be a successful tool for low temperature and high magnetic field studies of correlated electron system due to its simplicity, ruggedness, ease of measurement, and relatively high sensitivity. The working principle of VSM is based on Faraday's law of electromagnetic induction. In a VSM, a sample is attached to a vibrating rod and allowed to vibrate in a magnetic field produced by electromagnets. As the magnetization of the samples increases due to the increasing magnitude of the field, the change in flux induces a net voltage signal measured by induction coils located near the samples. The signal is usually small, and is measured by a lock-in amplifier at a frequency specified by the signal from the sample vibrator. The signal measured by the induction coils is directly proportional to the magnetization of the sample, and independent of the external field intensity. Plotting the induction vs.magnetic field intensity (H) results in a hysteresis curve representative of the samples magnetization. Nevertheless, it can lack adequate sensitivity on ultrathin films or samples with diluted magnetic moment.

In the present work, the measurements were done using KLA-Tencor EV7 VSM, located at the Laboratories of the Group of *Nanomagnetism and Magnetization Processes,* ICMM, and the Group of *Nanostructured Magnetic Materials,* University of Oviedo. The schematics are shown in Fig. 2.7.

The magnetization curves were studied mostly at room temperature but also for temperatures ranging from 50 to 300 K. The first order reversal curves were measured at room temperature.

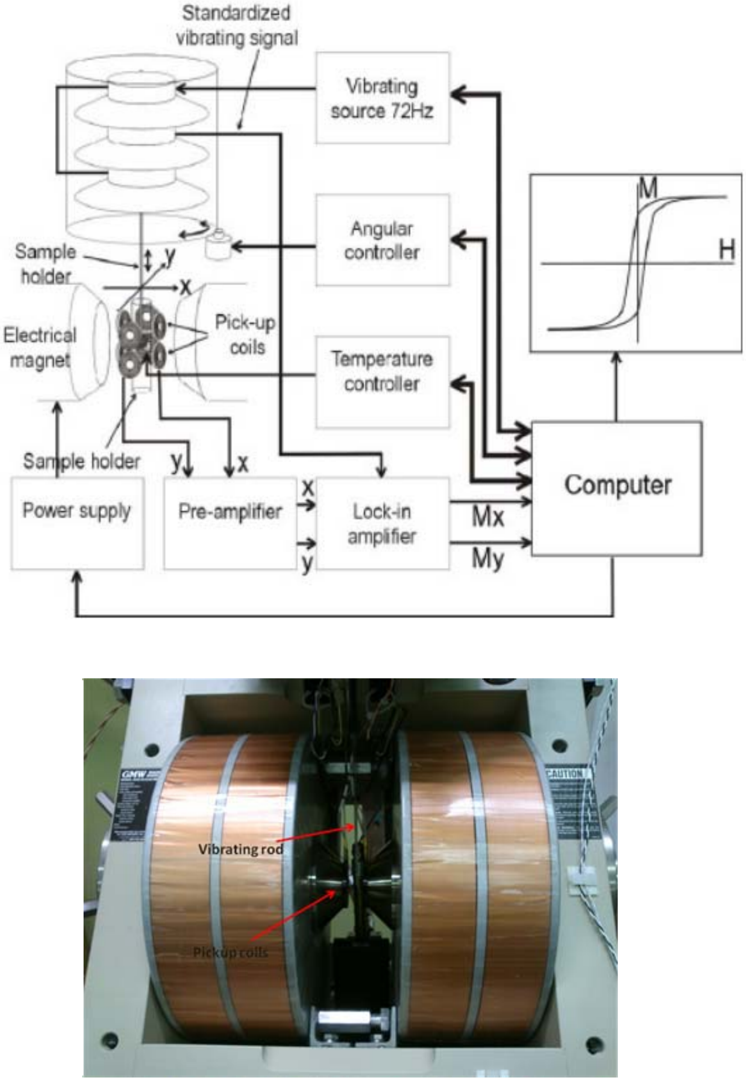

Fig. 2.7. Schematic diagram of vibrating sample magnetometers. (Bottom: image of the VSM part where the pickup coils and the sample are located).

2.5. Electrical resistance and magnetoresistance measurements

Usually, when working with smooth thin-films, silver-paint electrical contacts are directly placed over the sample's surface. However, due to the accentuated roughness of the AAO surface, it became of important to deposit first gold micro-contacts onto the samples, before the standard silver-paint contacts were connected, thus avoiding detachment from the AAO templates, especially at low temperatures. The micro-contacts were deposited with a low-vacuum BOC Edwards SCANCOAT SIX sputtering unit. For the measurements of arrays of nanowires (prepared by pulsed electrodeposition), one-contact was necessary to deposited on top of the array, and the current flows parallel to the nanowire longitudinal direction, passing through the barrier layer at the bottom.

The temperature dependent electrical transport measurement systems existent at IFIMUP (Instituto de Física dos Materiais da Universidade de Porto) based on closed cycle He cryostats of the Gifford-McMahon type. These systems undergo He expansion/compression cycles enabling to reach temperatures of ~10 K.[19]

For the transport measurements, the samples were glued to a copper sample-holder with a special varnish (GE-varnish), thus ensuring electrical insulation, down to cryogenic temperatures, between the conductive bottom Al foil and the sample holder, but also keeping a good thermal contact between the two. Silver-paint spots were placed on top of previously sputtered, Au micro-contacts and directly connected to 70 μm diameter copper wires. The sample-holder was then mounted in the cold Cu basis of the closed cycle cryostat with the copper wires well (thermally) anchored along the cryostat to minimize difference of temperatures between measuring wires in such spots, and so significantly reducing thermoelectrical effects in the measured voltages. The temperature was monitored with a NiCr(10 %) / AuFe(0.07 %) thermocouple, where the cold junction was thermally coupled with pressed In (in a small hole) to the sample holder and placed as close as possible to the sample. When a magnetic field was required, an electromagnet from GMW-Magnet System (Fe core nucleus) was used, powered by a magnet power supply with electrical currents up to 60 A. The magnetic field was measured using a Hall probe (Applied Magnetics Labs) locally calibrated (10^{-4} T sensitivity), taking readings in a HP 3457A voltmeter.

The electrical resistance (*R*) and magnetoresistance (*MR*) were studied for temperatures ranging from 20 to 300 K and applied magnetic field up to 1 T. The magnetic nanowires, were investigated in magnetic fields both along and perpendicular to the nanowires.

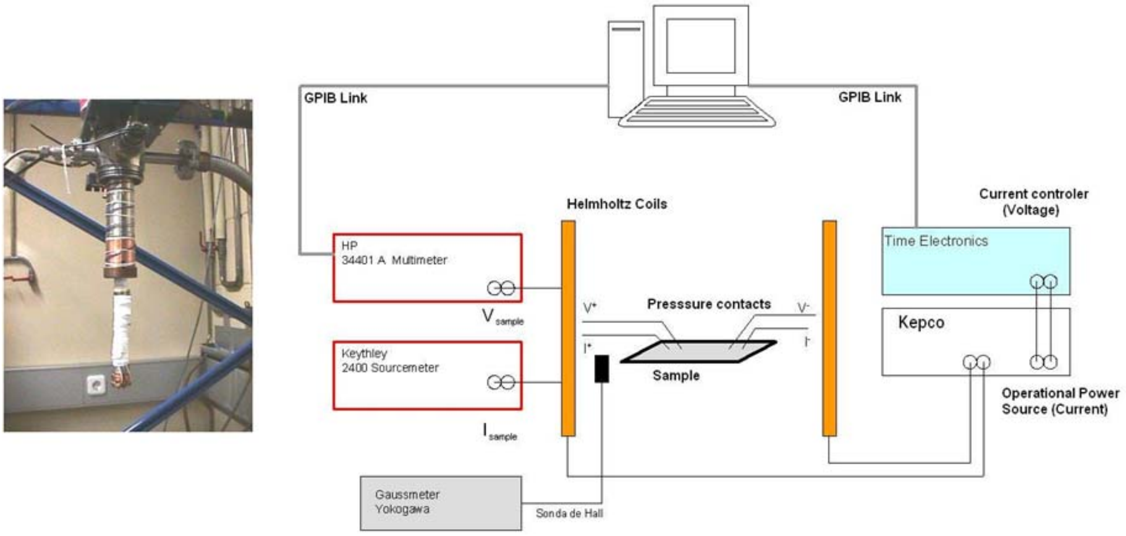

Figure 2.8. Transport measurement set-up: (left) cryostat system for *R(T)* and *MR(T)* measurements; (right) station for room temperature *R* and *MR* measurements.[19]

2.6. References

[1] H. Masuda and K. Fukuda, Science **268**, 1466 (1995).

[2] L. Ba and W.S. Li, J. Phys. D: Appl. Phys. **33**, 2527 (2000).

[3] K.R. Pirota, D. Navas, M. Hernández-Vélez, K. Nielsch and M. Vázquez, J. Alloys Compounds **369**, 18 (2004).

[4] O. Jessensky, F. Muller and U. Gösele, Appl. Phys. Lett. **72**, 1173 (1998).

[5] M. Vázquez, K. Pirota, J. Torrejón, D. Navas and M. Hernández-Vélez, J. Magn. Magn. Mater. **294**, 174 (2005).

[6] H. Masuda, F. Hasegawa and S. Ono, J. Electrochem. Soc. **144**, L127 (1997).

[7] V.M. Prida, K.R. Pirota, D. Navas, A. Asenjo, M. Hernández-Vélez and M. Vázquez, J. Nanosci. Nanotechnol. **7**, 272 (2007).

[8] K. Nielsch, J. Choi, K. Schwirn, R.B. Wehrspohn and U. Gösele, Nano Lett. **2**, (7), 687 (2002).

[9] A.P. Li, F. Müller, A. Birner, K. Nielsch and U. Gösele, Adv. Mater. 11, 483 (1999).

[10] C. R. Martin*,* Science **266,** 1961 (1994).

[11] H. Zeng, M. Zheng, R. Skomski, D. J. Sellmyer, Y. Liu, L. Menon and S. Bandyopadhyay, J. Appl. Phys. **87,** 4718(2000).

[12] K. Ounadjela, R. Ferré, L. Louail , J. M. George, J. L. Maurice, L. Piraux and S. Dubois, J. Appl. Phys. **81,** 5455 (1997).

[13] C. T. Sousa, D.C. Leitao, M. P. Proenca, A. Apolinário, J. G. Correia, J. Ventura and J. P. Araujo, Nanotechnology **22,** 315602 (2011).

[14] K. Nielsch, F. Müller, A.P. Li, U. Gösele, Adv. Mater. **12**, 582 (2000).

[15] R. M. Metzger, V. V. Konovalov, M. Sum, T. Xu, G. Zangari, B. Xu, M. Benakli, W.D. Doyle, IEEE Trans. Magn. **36**, 1 (2000).

[16] V. Vega, W. O. Rosa, J. García, T. Sánchez, J. D. Santos, F. Béron, K. R. Pirota, V. M. Prida, and B. Hernando, J. Nanosci. Nanotechnol., (in press).

[17] V.M. Prida, V. Vega, J. García, L. González, W.O. Rosa, A. Fernández and B. Hernando, J. Magn. Magn. Mater. (in press).

[18] S. Foner, Rev. Sci. Instrum. **30,** 548 (1959).

[19] Diana Cristina Pinto Leitão, *Micro and Nano Patterned Magnetic Structures*, PhD thesis, Universidade do Porto, 2010.

Chapter 3: On the Fabrication, the Structural Properties and Magnetic Behavior

3.1. Introduction

The magnetic behaviour of ordered arrays of magnetic nanowires is controlled by the combined action of anisotropy energy terms determined by geometrical shape, crystalline structure and magnetostriction, as well as by the magnetostatic interactions among them. For Co and Co-base nanowires the magnetocrystalline anisotropy plays a very important role. Their *hcp* or *fcc* crystal structure is confirmed to depend on the synthesis parameters, such as, the electrolytic bath acidity, on the presence of selected elements in the composition and on the template´s geometry.

For regular Co at ambient pressure, *hcp* is the phase stable at temperatures below 422 °C, and *fcc* is the stable phase at temperatures above 422 °C.[1] In electroplated Co, the *fcc* phase can be obtained from electroplating at ambient temperature and pressure using a low pH (< 2.5) electrolyte. The low pH electrolyte enhances the H_2 evolution and the Co ion mobility during the electroplating process. The enhanced atomic mobility may be equivalent to high temperature condition so that the *fcc* phase is obtained.[2] On the other hand, a coexistence of both Co phases has been reported in different works.[3,4] Also, one can expects a transition to a *fcc* phase for nanowires diameters of ~ 30 nm.[4] Other investigations of Co nanoparticles[5] show that the presence of a *hcp* phase or a *fcc* phase can be related to the particle diameter. In that case, the transition from *hcp* to *fcc* was ascribed to a size effect due to the lower surface energy of the *fcc* phase.

In this chapter the samples prepared are described and their magnetic behavior are presented as a function of (i) the pH of the electrolytic bath, (ii) the composition (e.g. adding Ni or Pd) and (iii) the geometry (e.g. diameter of particularly short lengths).

3.2. Samples preparation

3.2.1. AAO membranes

Highly pure aluminum foils of 0.5 mm thickness and 25 mm diameter were electropolished in a 1:4 volume mixture of perchloric acid and ethanol. The foils were then anodized in 0.3M oxalic (or 0.3 M sulphuric acid solution) at 2ºC (0ºC) under an applied potential of 40V (25V). First anodization stage lasted for 24 h. Subsequently,the anodized foils were immersed in a solution composed of 0.2M chromic and 0.5M phosphoric acid at 35ºC for 12 h to remove the anodized layer. The foils were then anodized with identical parameters as those of the first step for different times ranging from 3 min to 24 h, depending on the desired nanopores lenghts.

Figure 3.1 shows the top view SEM micrographs of a AAO membranes after the second anodization step in oxalic [Fig.3.1 (a)] and sulphuric acid [Fig.3.1 (b)]. As seen in this figures hexagonal self-assembled nanopores were formed. In the oxalic membrane, the nominal diameter, *D*, of 35 nm was increased up to 63 nm with 105 nm of interpore distance, D_{int}. The values for the sulphuric membrane were the nominal ones, *D* of 25 nm and D_{int} of 65 nm. In the cases in which the pore diameter was increased, it was necessary a chemical etching using a solution of H_3PO_4 (5 wt%) with different exposure times.

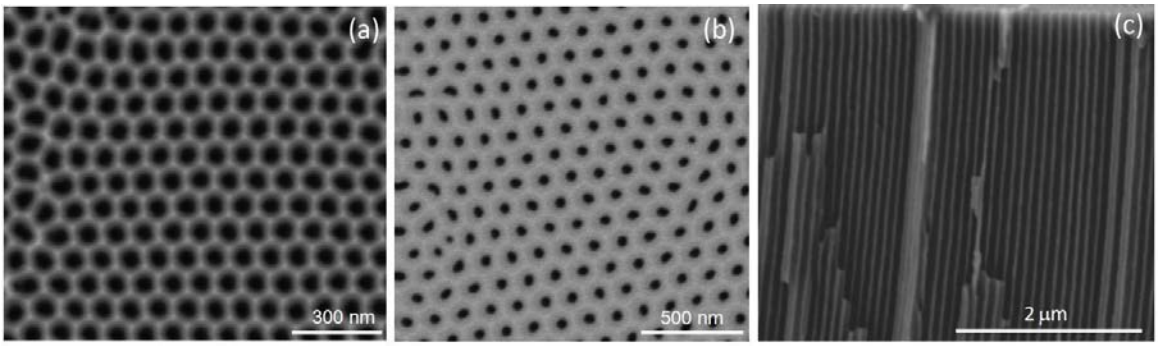

Fig. 3.1 (a) Top view SEM of AAO membranes obtained with different acidic solutions: (a) oxalic acid and (b) sulphuric acid. (c) Cross-section of an oxalic membrane.

Subsequent filling of nanoporous is performed after surface preparation of the oxide barrier layer at pore bottom by pulsed electrodeposition technique. When it was necessary or desired to avoid the drawback of the dendrites the samples were grown by potentiostatic mode. Independent of the electrodeposition method, the different lengths, *L*, of the samples were controlled by changing the electroplating time. Full additional details regarding the electroplating process and their conditions can be found in Chapter 2 or will be specified when it is required.

3.2.2. Electroplating Process of Co

Electrodeposited Co has a *hcp* structure, although the cubic phase can be obtained using particular deposition parameters, such as low pH and/or high temperature or deposition rate.[6] The electrocrystallization of cobalt is a complex phenomenon that has been widely studied.[7] Although many reactions are involved in this electroplating process, four main reactions are pointed out. The basic reaction is the reduction of the Co^{2+} ions into Co,

$$Co^{2+} + 2e^{-} \longrightarrow Co, \tag{3.1}$$

Hydrogen evolution, reduction of hydrogen into gaseous H_2, more active as the solution is more acid (higher concentration of H^- ions)

$$2H^{+} + 2e^{-} \rightleftarrows H_2, \tag{3.2}$$

Also, OH^- ions are produced at the cathode, inducing an alkalinization of the growth surface,

$$2H_2O + 2e^{-} \longrightarrow H_2 + 2OH^{-}, \tag{3.3}$$

In parallel, the Co^{2+} ions interact with the OH^- ions from reaction (3.3), leading to the production of cobalt hydroxides

$$Co^{2+} + OH^{-} \rightleftarrows CoOH^{+}, \tag{3.4}$$

The influence of the pH on the electroplating process of cobalt films has been demonstrated, and it can induce structural modifications in the final Co nanowires.[8] A short, basic description is given here. At pH in the range 3–6, the structure is *hcp* Co with the easy magnetization axis (*c*-axis) perpendicular to the growth direction. At low pH (less than 2.5), reaction (3.2) produces high concentration of hydrogen that is adsorbed in the deposit. The growth process is thus heavily disturbed and Co crystallizes in a *fcc* Co structure. Moreover, this structure is heavily faulted due to the desorption of hydrogen from the deposit. Above pH 6.0, the onset of hydroxide precipitation is reached. A Co-hydroxide layer is formed at the surface of the growing crystallite. The reduction of cobalt then occurs through this intermediate layer following a two steps reaction (fully described in Ref. 9)

$$CoOH^{+} + e^{-} \rightleftarrows CoOH_{ads}, \qquad (3.5)$$

$$CoOH_{ads} + e^{-} \rightleftarrows Co + OH^{-}, \qquad (3.6)$$

It has been suggested that the growth of *hcp* Co with the *c*-axis parallel to the growth direction is promoted by the presence of such Co-hydroxide layer.[9]

3.3. Electroplating Co changing the electrolytic bath acidity, pH

The as-prepared Co solution (see Chapter 2) with typical pH value of 3.5 has been gradually increased to 4.5 and to 6.7 by the addition of diluted NaOH (0.5 M). The nanowires were grown by potentiostatic mode at -1 V of applied voltage (at room tempetarature).For each of the three pH values, it was prepared three wire lengths: 3, 8 and 30 μm. The pore diameter was fixed at ~ 50 nm for all the samples in this section.

Figure 3.2(a) shows the cross-section of an AAO membrane filled with Co nanowires (L ~ 3 μm). The inset is the AAO membrane surface where the hexagonal order degree and the homogeneity of the pores can be observed. XRD patterns of the nanowires embedded into the templates and electroplated at the different pH values are presented in Fig. 3.2(b) for L ~ 3 μm. The *hcp*-phase was identified in all the cases, showing strong textures along [100], [101] and [002] directions depending on the respective pH value. These textured structures at 2θ = 41.5°, 47.5° and 44.5° are ascribed to hexagonal crystalline anisotropy with *c*-axis nearly perpendicular, at ~ 45° and parallel to the wires axis, respectively.[10] (See figure 3.3). These results are in agreement with what was reported by Darques, *et al.*[11] They found that for pH values of 3.8 - 4.0, the *c* axis of the *hcp* phase is oriented perpendicular to the wires or parallel for pH values ≥ 6. Also, as it was discussed above, in previous works involving electrodeposited Co films, these kind of structural changes are attributed to the influence of absorbed hydrolysis products at the cathode as well as to the evolution of hydrogen, which are known to depend on the pH.[12, 13]

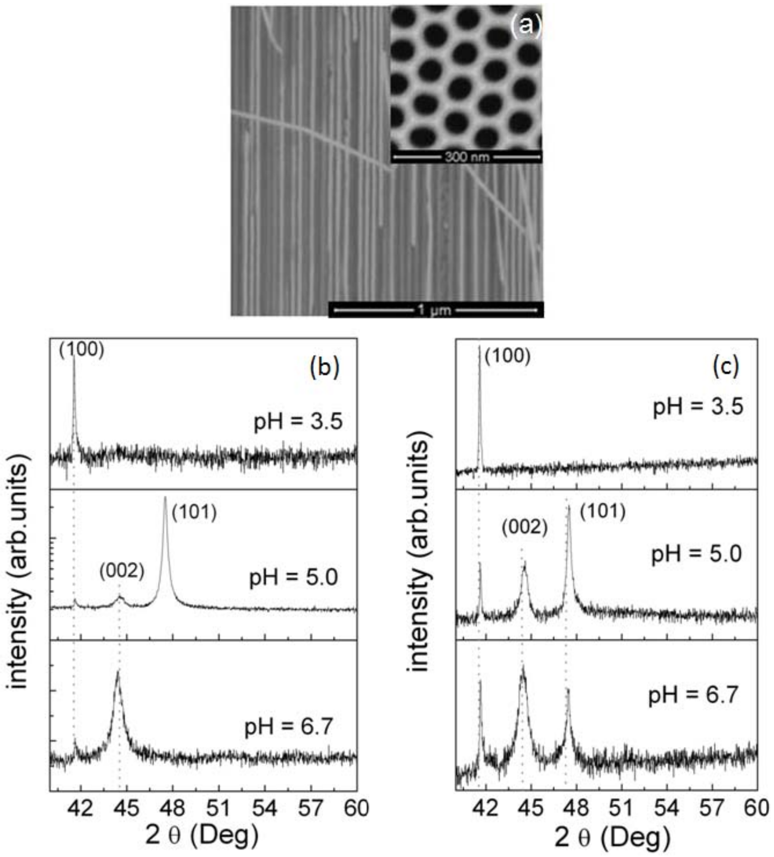

Fig. 3.2 (a) SEM of cross-sectional view of AAO membranes filled with Co nanowires (the inset shows a SEM of an AAO upper view). (b) XRD patterns of the *hcp* phase for L ~ 3 µm and (c) L ~ 30 µm.

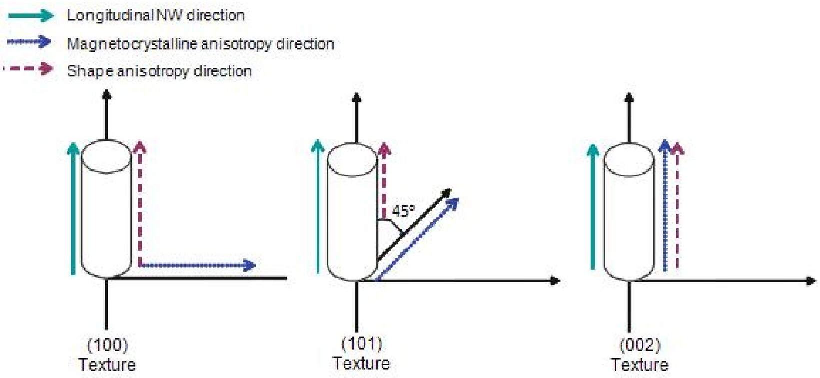

Fig. 3.3. Schematic diagram showing directions of shape and magnetocrystalline anisotropies and NW long axis for (100), (101), and (002) *hcp* Co textures.

On the other hand, increasing the length of the wires leads to a reduction of the crystal texture, particularly for the (002) and (101) peaks as can be observed in the diffractions peaks of Fig. 3.2(c) and in the increase of the perpendicular coercivity in Figs. 3.4 (e)-(f), which is discussed below.

Magnetic hysteresis loops, shown in Fig. 3.4 for arrays of Co NWs 3 and 30 µm long, have been measured in a Vibrating Sample Magnetometer (VSM) under longitudinal (//) (parallel to nanowires axes) and perpendicular (⊥) (in-plane) configuration of the applied field. A clear uniaxial magnetic anisotropy can be inferred from the high longitudinal remanence and coercivity and their vanishing perpendicular values for the nanowires textured in the [002] crystallographic direction, (pH 6.7). A more balanced anisotropy is deduced for the sample textured in the [101] direction (pH 5.0), while a more complex anisotropy distribution is suggested for the [100] texture (pH 3.5), where there is deduced a strong competition of the parallel and perpendicular magnetic anisotropies. Besides, for longer nanowires [Fig.3.4 (d)], it can be observed two smooth jumps in the magnetization reversal when the field in applied perpendicular to the wires, suggesting the coexistence of two different magnetic species. From the XRD results for nanowires of 30 μm long, there was detected a textured in the [100] direction when using pH of 3.5 in the sample preparation, and no other crystallographic peak was detected. Although, these two magnetic entities should have the same crystal properties, thus, the magnetization reversal in this case should be governed by complex dipolar interactions, which are expected to be more relevant in large systems.

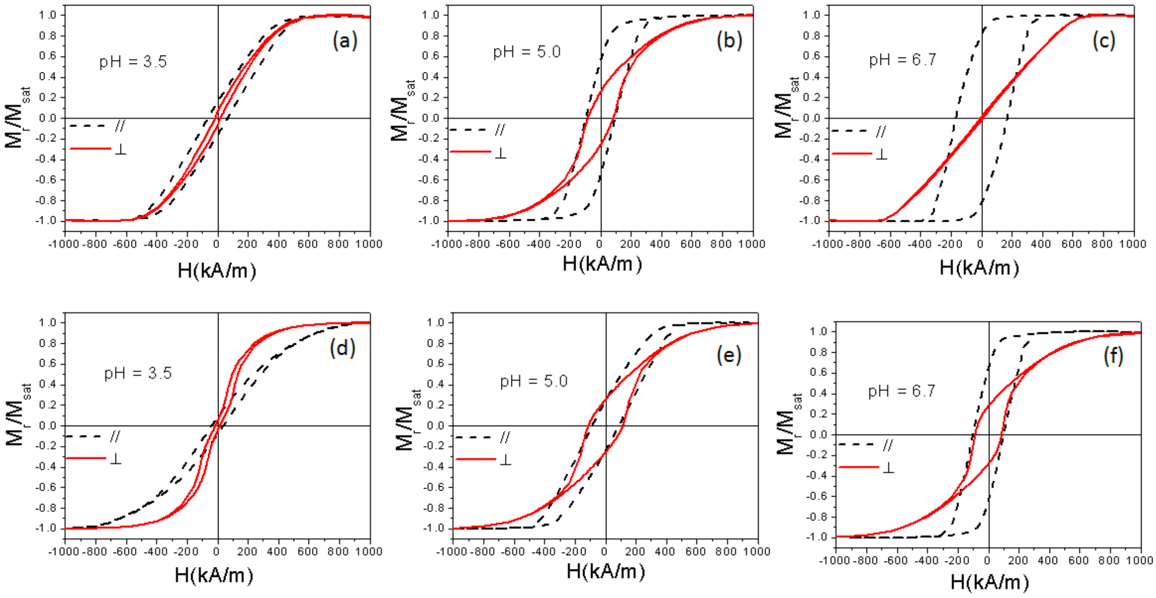

Fig. 3.4 Normalized longitudinal (//) and perpendicular (⊥) hysteresis loops for nanowires with $L \sim 3$ μm [(a), (b) and (c)] and with $L \sim 30$ μm [(d), (e) and (f)] for different electrolytic bath acidity.

3.4. Co-base nanowire arrays

The magnetic behavior of nanowire arrays can also be tuned by modifying the composition. For example, the addition of Ni or Pd allows one to partly retain the large saturation magnetization and high coercivity of Co, while enhancing the uniaxial anisotropy. Therefore, an appropriate Co-base alloy can be a simple and controllable route to tune the magnetic properties of this system. These samples were prepared using oxalic membranes (center to center nanowire distance, D_{int}, of 105 nm) and the wires were grown by pulsed electrodeposition method. In order to obtain the different CoPd and CoNi alloys the current density was varied to have the desired compositional Co/alloy ratios, which were determined by EDX in SEM. The length of the wires and the pore diameter were fixed at 35 nm and 2.5 μm, respectively.

3.4.1. The case of Co_xNi_{1-x} nanowires ($0 \leq x \leq 1$)

Figure 3.5 displays the XRD θ-2θ scans corresponding to the Co, $Co_{80}Ni_{20}$ and $Co_{50}Ni_{50}$ nanowire arrays, from top to bottom. For the Co sample, only the (100) *hcp*-phase peak is detected indicating a textured structure. Although the presence of mixed *fcc-hcp* phases on electrodeposited Co nanowires can be present for diameters around 30 nm, we did not observe any peak corresponding to this phase. However, reducing the length, the panorama turns more complex, as it will be discussed later. With the addition of Ni the presence of the *hcp* (100) Co peak decreases significantly. Instead, two peaks are observed around 44.5º being more intense for $Co_{50}Ni_{50}$ (indicating a textured structure) than for $Co_{80}Ni_{20}$. At $2\theta = 44.2º$ and 44.5º one expects the (111) Co *fcc* peak and the (111) Ni *fcc* peaks, respectively. This behaviour indicates that the crystal structure of the nanowires has evolved from a *hcp* to a *fcc* phase.

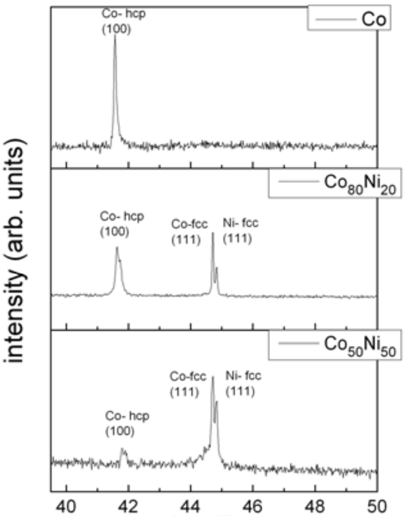

Fig. 3.5. XRD θ-2θ diffraction patterns of Co, $Co_{80}Ni_{20}$, and $Co_{50}Ni_{50}$ nanowires.

Figure 3.6 shows the room temperature hysteresis loops of the samples for // and ⊥ applied field configuration. From a comparative analysis, a weak effective longitudinal magnetic anisotropy can be assumed for Co nanowires, since both parallel coercivity (H_c) and parallel reduced remanence ($m_r = M_r/M_{sat}$) take slightly larger values than the corresponding perpendicular ones. That reflects a balance between magnetic anisotropies. While the textured (100) *hcp* phase of Co leads to a magnetocrystalline anisotropy with a perpendicular magnetic easy axis, the strong effect of the shape anisotropy results in a preferential orientation of the magnetization parallel to the nanowires. These observations are in agreement with previously reported data on polycrystalline Co nanowires.[14, 15] With the addition of Ni, a reinforcement of the parallel magnetic easy-axis is observed, reflected in the increase of $H_c^{//}$ and $m_r^{//}$, and consequent decrease in $m_r^{\perp}$. However, an overall increase in $H_c^{\perp}$ is also visible. In this case, the samples polycristallinity and the presence of both *hcp* and *fcc* phases, may lead to local crystal inhomogeneities originating the observed increased irreversibility in the perpendicular *M(H)* loop.

For sulphuric membranes (D_{int} = 65 nm) of the same pore diameter (35 nm), similar crystallographic results were obtained for CoNi nanowires. However, it was observed a reduction of both magnetic parameters H_c and M_r when comparing with the oxalic membranes samples. The ratio D/D_{int} is higher in the sulphuric samples, hence, it is expected a reduction in the effective anisotropy of the system due to the reinforcement in the magnetostatic interactions among nanowires, which is in agreement with previous reports.[16] The magnetic results for the sulphuric samples will be discussed in the frame of the temperature behavior in Chapter 5.

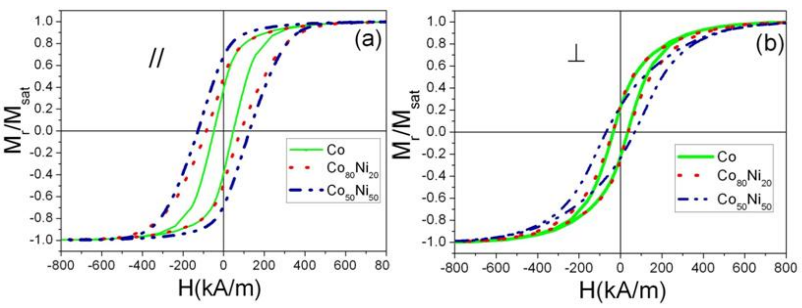

Fig. 3.6. Normalized hysteresis loops of Co, $Co_{80}Ni_{20}$ and $Co_{50}Ni_{50}$ nanowires for (a) parallel and (b) perpendicular applied magnetic field.

3.4.2. The case of Co_xPd_{1-x} nanowires ($0 \le x \le 0.6$)

Figure 3.7(a) shows the cross-sectional view of AAO membranes filled with CoPd nanowires. The crystal spectra of selected CoPd nanowire arrays namely, $Co_{88}Pd_{12}$ and $Co_{56}Pd_{44}$ are presented in Fig. 3.7(b).The presence of the two Co phases is confirmed: *hcp* (denoted by (100) and (101) peaks) and *fcc* ((111) peak). In addition, (111), (200) and (220) Pd peaks are also detected. Note however that for the Co-rich sample the (101) Co peak and the (200) Pd peak are not fully resolved, while when the amount of Pd is increased, the peaks (100) and (111) of Co and Pd, respectively, are not detected. It appears that a moderate Pd content results in a complex spectrum with a significant *fcc* Co contribution, while higher Pd content results in a significant reduction of Co peaks.

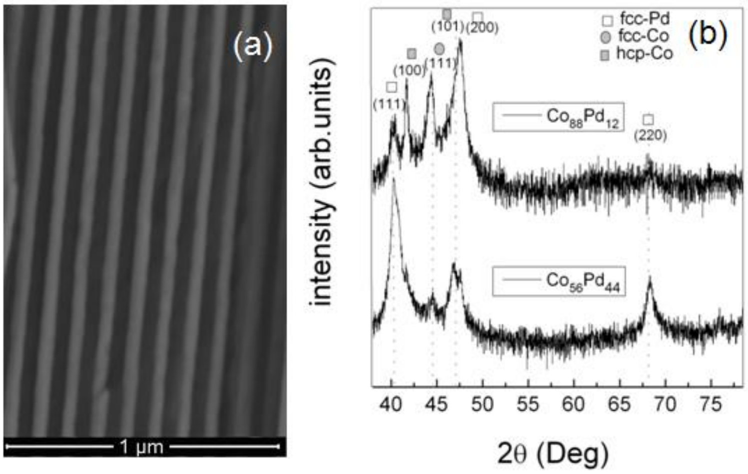

Fig. 3.7. (a) SEM of cross-sectional view of a AAO membrane filled with CoPd NWs (b)XRD θ-2θ diffraction patterns of $Co_{88}Ni_{12}$, and $Co_{56}Ni_{44}$ nanowires.

An even more outstanding evolution of the magnetic anisotropy easy axis with composition is observed for the CoPd nanowire arrays as it can be observed in Table 1. While Co-rich nanowire system denotes the presence of a clear transverse anisotropy in the case of CoNi nanowires, at lower Pd content, CoPd nanowires exhibit the optimum behavior as much as longitudinal anisotropy and coercivity is concerned. As it was mention above, higher Pd content reduces the Co peaks in the XRD spectrum, in particular, which seem to affect the magnetic properties. However, the polycrystallinity and non-textured character of these samples makes difficult to establish a clear correlation between the crystal structure and the behavior of both H_c and m_r parameters. Hu et *al.*,[17] report that the crystallization of Co_xPd_{1-x} was not perfect, resulting in nanowires composed of CoPd alloy with some Co and Pd clusters. They report also, optimized longitudinal magnetic properties for Co-rich samples.

Table 1: Experimental magnetic parameters of CoNi, and CoPd nanowire arrays extracted from hysteresis curves.

Sample	$H_c^{\parallel}$(kA/m)	$m_r^{\parallel}$	$H_c^{\perp}$(kA/m)	$m_r^{\perp}$
Co	49	0.38	33	0.23
$Co_{80}Ni_{20}$	85	0.51	37	0.24
$Co_{50}Ni_{50}$	127	0.73	69	0.22
$Co_{88}Pd_{12}$	129	0.91	60	0.10
$Co_{74}Pd_{26}$	124	0.80	34	0.12
$Co_{56}Pd_{44}$	105	0.74	48	0.20
$Co_{48}Pd_{52}$	93	0.70	16	0.20

3.5.On the geometric characteristics

In this section it is studied the influence of the geometry characteristics of the Co nanowire arrays: their length and diameter. That makes an influence not only in the shape anisotropy and magnetostatic interactions, but also in the crystallographic structure.

3.5.1. As a function of length

These samples were grown by pulsed electrodeposition in oxalic membranes, D_{int} of 105 nm). In order to study the effect of changing the length, the results discussed below are for nanowires with diameter of nm and the length was varied from 120 to 1000 nm. Figure 3.8 shows the cross-sectional view of SEM image of AAO membranes filled with Co nanowires, L ~ 120 nm (a), and L ~ 1000 nm (b). One can see the existence of empty pores (due to the breaking of the samples needed to obtain this image), and the dendrites at the bottom filled with Cu.

XRD patterns of Co nanowire arrays with given diameter and different length are presented in Fig. 3.9. The intense peak at $2\theta = 44.7^{\circ}$ arises from the (200) *fcc* phase of the underlying aluminium foil (for experimental simplicity, the samples were grown by pulsed electrodeposition method within the membranes, which were attached to the Al). For the shorter (120 nm long) nanowires, only a broadening on the left side of the aluminium peak is visible. This could reflects the presence of the diffraction peak from the *fcc* (111) crystallographic phase at $2\theta = 44.2^\circ$. Nevertheless, this phase could overlap with the *hcp*-(002), at $2\theta = 44.5^\circ$. As the length of Co nanowires increases, *hcp*-phase peaks are observed and become almost the only detected for the longest (1000 nm) nanowires. For longer wires ($L > 500$ nm), a strong preferential texture in the (100) direction for the *hcp* phase is observed, which increases with the nanowire length. The intensity of the *hcp* (100) peak at $2\theta = 41.7^\circ$ denotes a textured structure, which has been ascribed to a perpendicular crystalline anisotropy. Less intense *hcp* (002) and *hcp* (101) peaks appear at $2\theta = 44.5^\circ$ and 47.4°, respectively. A detailed synchrotron XRD study has been recently performed on the modification of *fcc* and *hcp* Co crystallographic phases with increasing length of nanowires.[18] There, as in the present results, a critical nanowire length of around 270 nm is estimated below which Co crystallizes into *fcc* phase, while the upper part of longer nanowires crystallizes mostly into *hcp*-phase. As it was shown before, for $1\ \mu\text{m} \leq L \sim 30\ \mu\text{m}$, the crystallographic structure is already dominated by the *hcp* phase, whereas less intense Co-*fcc* phase reflections cannot be discarded for $D \leq 35$ nm when the pH of the electroplating process is above 2.5 at room temperature. The crystal and magnetic behaviors for this kind of nanowires with $L \sim 30\ \mu\text{m}$ is quite similar for those of $L \sim 40\ \mu\text{m}$.[19]

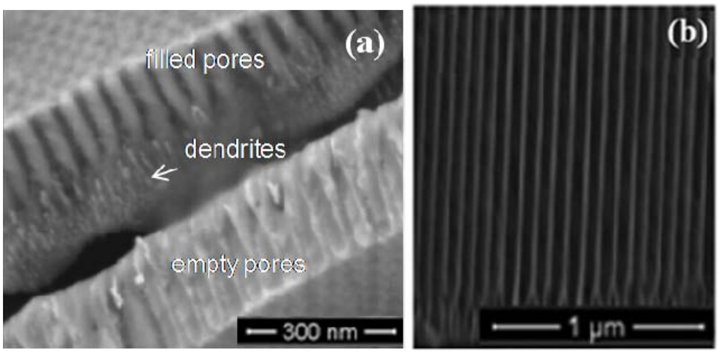

FIG. 3.8. SEM of cross-sectional view of AAO membranes filled with Co nanowires for (a) $L \sim 120$ nm and (b) $L \sim 1000$ nm.

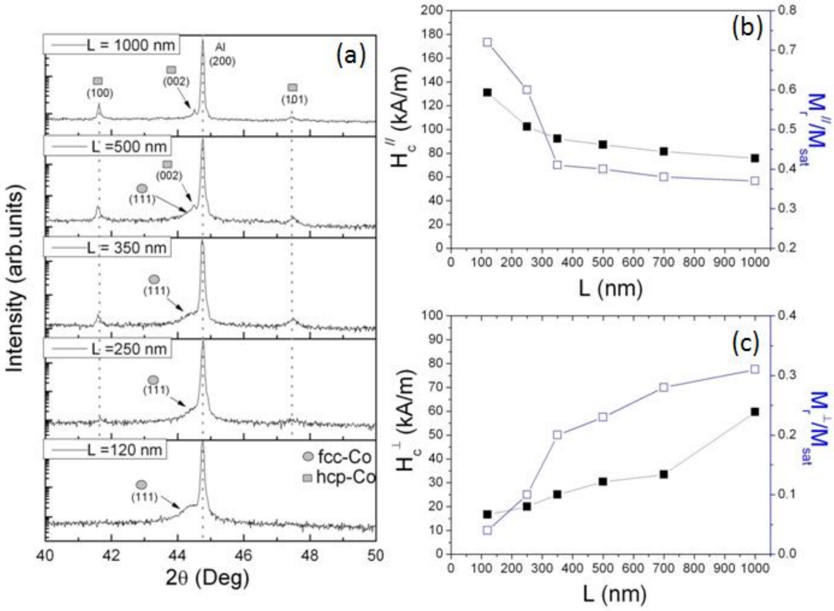

Fig. 3.9. (a) XRD patterns of Co NWs (*D* ~ 35 nm) with length going from 120 nm to 1000 nm. (b) Parallel and (c) perpendicular coercivity and reduced remanence as a function of NWs length.

A comparative analysis of parallel and perpendicular hysteresis loops for *L* ~ 120 nm reveals the presence of an effective longitudinal uniaxial magnetic anisotropy because m_r and H_c take larger values for the parallel field configuration, which confirms the relevance of the shape anisotropy. Nevertheless, increasing the nanowire length leads to the lowering of the effective longitudinal magnetic anisotropy, as deduced from the remanence decrease with the nanowire length [see figures 3.9(b)]. This is an unexpected result and may be ascribed to modification of the crystalline anisotropy, that is, the increase of the (100) Co *hcp* phase with a perpendicular to the wire crystalline anisotropy, in spite of the parallel increase of uniaxial longitudinal wire shape anisotropy. An additional effect comes from the demagnetisation factor of the thin film geometry of the nanowire array. One can see also in figure 3.9 (c) that $H_c^\perp$ and $m_r^\perp$ increase when *L* increases, which can be understood to a loss of effective anisotropy in the system as it has been discussing.

3.5.2. As a function of diameter

In this subsection the results for low aspect ratio (*L/D* < 10) nanowire arrays grown by potentiostatic mode in oxalic membranes are discussed. As already mentioned the nanowires diameter is predetermined by the diameter of the nanopores of the AAO membrane. The effect in the crystal properties of *D,* increased from 35 nm to 75 nm, was investigated for a fixed value of *L* ~ 120 nm, so that, the samples here will be called nanopillars instead of nanowires. Fig. 3.10(a) shows the cross-sectional SEM image of Co nanopillars (D ~ 44 nm) embedded in the AAO template, where the brighter segments are Au electrodeposited in order to improve the electrochemical contacts (bottom) and to protect of oxidation the sample (top). Fig. 3.10(b) shows the XRD results for this set of samples. For the case of D ~ 35 nm (discussed above), it cannot be properly resolved whether there is a contribution of the (002) *hcp* peak, however, the *fcc* phase is expected to be the dominant one. Increasing the diameter, the *hcp* phase is the only detected in the diffraction patterns and the orientation of the hexagonal *c*-axis has been found to change from parallel (D ~ 44 nm) to perpendicular to the wire axis (44 nm < D ~ 75 nm). In spite of the reduction in the aspect ratio of the samples presented here, a similar result has been obtained for nanowires (L/D ~10 μm), where this reorientation of the *c* axis appears above a critical diameter of about 50 nm.[20] This observation suggests that the hysteresis of the nanowire array may be significantly increased by a further reduction of the nanowire diameter.

Figures 3.11 (a)-(d) show the typical hysteresis loops of Co nanopillars arrays in AAO templates for different pillar diameters at magnetic field applied both parallel and perpendicular to the pillar axis. For D ~ 35 nm and 44 nm, the magnetization easy axis is clearly defined in the pillar axis. At D ~ 63nm, although $H_c^{//}$ is higher than $H_c^{\perp}$, m_r takes almost the same values for the parallel and the perpendicular applied field configurations. Finally, for D ~ 75 nm it could not be established a preferred orientation of the magnetization for the applied magnetic field angle range at 0^o (out of plane) or 90^o (in plane).

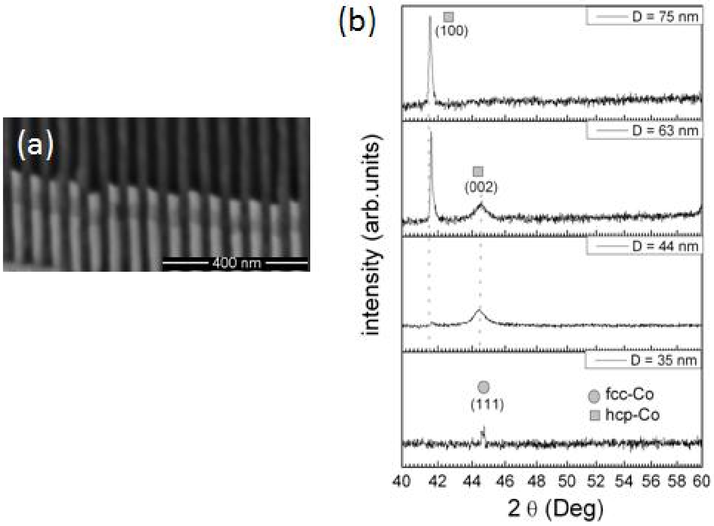

Fig.3.10.(a) Cross-sectional SEM image of Co nanopillars embedded in the AAO template, where the brighter segments are Au electrodeposited in order to improve the electrochemical contacts (bottom) and to protect of oxidation the sample (upper part). (b) XRD θ–2θ diffraction patterns of 120 nm long Co nanopillars with increasing diameter from 35 nm to 75 nm.

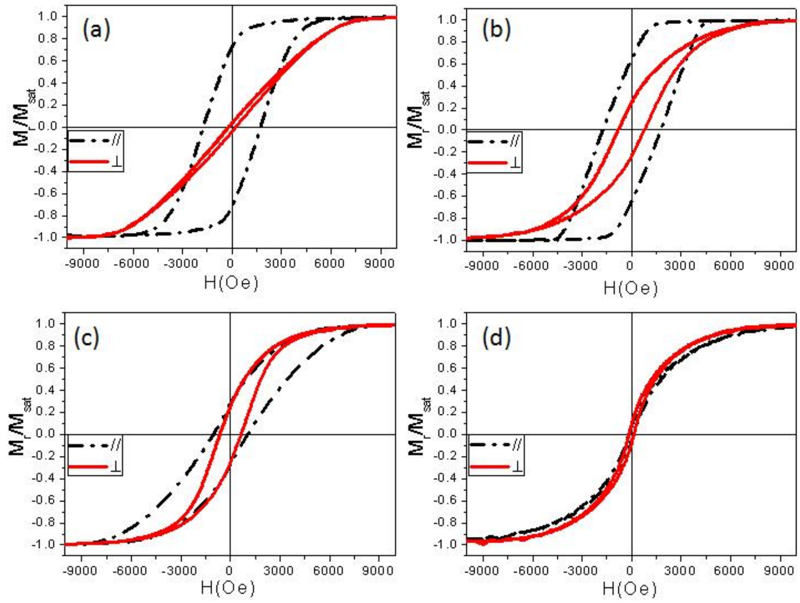

Fig. 3.11. Normalized hysteresis loops for Co nanopillar arrays under parallel and perpendicular applied magnetic field. (a) *D* ~ 35 nm, (b) *D* ~ 44 nm, (c) *D* ~ 63 nm and (d) *D* ~ 75 nm.

The magnetic behavior of the nanopillar arrays is expected to be determined mainly by two factors, firstly by the soft/hard magnetic nature of individual nanopillars, including their crystalline character, texture, orientation of crystalline axes with regards to nanopillar axis, and secondly, by the magnetic interactions among them, which is in turn determined by all the parameters mentioned above. For these samples, it can be observed that both coercivity and remanence decreases as the pillar diameter increases

(Table 2). This is expected since a larger diameter facilitates the formation of magnetic multidomain structures, hence degrading H_c and m_r. However, this is not true for the case of $D \sim 44$ nm. This result can be understood in the light of results from XRD. Electrodeposited Co is proved to adopt a rather good quality hexagonal compact structure with a preferential texture which depends on the diameter of the pillars. For the case of $D \sim 44$ nm, the *c*-axis is preferentially oriented parallel to the revolution axis of the pillars, whereas for larger diameters, it is aligned within the normal plane to the pillar axis. Cobalt pillars should thus possess a strong crystal anisotropy (K_1 = 4.5e5 J/m^3 in bulk *hcp* Co),[19] and always favoring an alignment of the magnetization along the *c*-axis. Therefore, crystal anisotropy should be reinforce the longitudinal shape anisotropy. That explains the similar values of coercivity and remanence when compared with the respective values for $D \sim 35$ nm, where the crystal anisotropy has been discussed to be almost due to the (111) *fcc* Co phase oriented along the pillar axis, thus, the magnetic behavior is expected to be similar to those nanowires without magnetocrystalline anisotropy.[3]

Table 2: Experimental magnetic parameters of Co nanopillar arrays extracted from hysteresis curves.

D (nm)	$H_c^{\parallel}$(kA/m)	$m_r^{\parallel}$	$H_c^{\perp}$(kA/m)	$m_r^{\perp}$
35	138	0.73	17	0.02
44	139	0.64	62	0.24
63	83	0.28	51	0.25
75	11	0.06	12	0.08

3.6. Summary

The objective of this chapter has been to emphasize the role played by the crystalline structure in the magnetic properties of Co and Co-base nanowire arrays. It can be concluded that:

(i) The crystalline structure can be tailored by the synthesis process. In particular, it has been shown that by modifying the electrolytic bath acidity, the pH, in the electrodeposition of Co nanowires, it is possible to induce different *hcp* Co phase textures, which will result in different magnetic behaviors.

(ii) An alternative way to tune the magnetic anisotropy without extreme changes in saturation magnetic moment is through the addition of other metallic elements. Here, it was paid attention to elements such as Ni and Pd. In the case of CoNi nanowires, the presence of the Co *hcp*-phase leads to an important competition between shape and magnetocrystalline anisotropies, which translates into a weakly defined magnetization easy axis along the nanowire longitudinal direction. With increasing Ni content the net crystalline anisotropy drastically decreases and the shape anisotropy becomes dominant. This latter effect is even more pronounced in the case of CoPd nanowires (highest m_r achieved), but for a lower Pd content.

(iii) The dimensions (i.e. length and diameter) of Co nanowires modify their crystalline structure. Particularly, for short electroplating time (i.e. reduced length of nanowires) *fcc*-crystal phase is dominant which together with shape anisotropy usually results in longitudinal magnetization easy axis. For longer electroplating time (i.e. longer nanowires), *hcp*-crystal phase is formed which determines the appearance of a magnetocrystalline anisotropy nearly at transverse orientation. In this case, a competition between shape and crystalline anisotropy is observed. For the case of Co nanopillars, it was found that for 35 nm of pore diameter the dominant crystal fase is the *fcc* one. Above this diameter the crystal structure is dominated by the *hcp* phase and a reorientation of the *c* axis is observed from out of plane to in plane for a pore diameter higher than 44 nm.

These findings indicate that the crystalline structure depend on the geometrical parameters and the particular deposition parameters. Further detailed investigations are required, in particular to understand the role of grain sizes, which are expected to affect magnetic properties.

3.7. References

[1] C. S. Yoo, H. Cynn, P. Söderlind, and V. Iota, Phys. Rev. Lett. **84**, 4132 (2000).

[2] T. Cohen-Hyams, W. D. Kaplan, and J. Yahalom, Electrochem. Solid-State Lett. **5**, C75 (2002).

[3] Z.Ye, H. Liu, Z. Luo, H-G. Lee, W. Wu, D. G. Naugle, and I. Lyuksyutov, J. Appl. Phys. **105**, 07E126 (2009).

[4] J. Sánchez-Barriga, M. Lucas, F. Radu, E. Martin, M. Multigner, P. Marin, A. Hernando, and G. Rivero, Phys. Rev. B **80**, 184424 (2009).

[5] O. Kitakami, H. Sato, Y. Shimada, F. Sato, and M. Tanaka, Phys. Rev. B **56**, 13849 (1997).

[6] S. Nakahara and S. Mahajan, J. Electrochem. Soc., **127**, 283 (1980).

[7] A. Vicenzo and P. L. Cavallotti, Electrochim. Act., **49**, 4079 (2004).

[8] I. M. Croll, IEEE Trans. Magn., **23**, 59 (1987).

[9] P. L. Cavallotti, E. Galbiati, and T. Chen, D. D. Snyder, U. Landau, and R. Sard, Eds. Pennington, NJ: ECS, 1983, p. 130.

[10] K. Maaz, S. Karim, M. Usman, A. Mumtaz, J. Liu, J. L. Duan, and M.Maqbool, Nanoscale Res. Lett. **5**, 1111 (2010).

[11] M. Darques, A. Encinas, L. Vila, and L. Piraux, J. Phys.: Condens. Matter. **16**, S2279 (2004).

[12] X. W. Wang, G. T. Fei, P. Tong, X. J. Xu, L. De Zhang, J. Cryst. Growth, **300**, 421 (2007).

[13] J.A. Switzer, H.M. Kothari, E.W. Bohannan, J. Phys. Chem. B, **106** 4027 (2002).

[14] H. Schlorb, V. Haehnel, M. S. Khatri, A. Srivastav, A. Kumar, L. Schultz, and S. Fahler, Phys. Stat. Sol. B. **247**, 2364 (2010).

[15] A. Ghahremaninezhad and A. Dolati, J. Alloy Comp. **480**, 275 (2009).

[16] M. Vázquez, K. Pirota, J. Torrejón, D. Navas, M. Hernández-Vélez, J. Magn. Magn. Mater. **294**, 174 (2005).

[17] H.N. Hu, H.Y. Chen, S.Y. Yu, L.J. Chen, J.L. Chen, G.H. Wu, J. Magn. Magn. Mater. **299**, 170 (2006).

[18] K. R. Pirota, F. Béron, D. Zanchet, T. C. R. Rocha, D. Navas, J. Torrejón, M. Vazquez, and M. Knobel, J. Appl. Phys. **109**, 083919 (2011).

[19] L. G. Vivas, R. Yanes, O. Chubykalo-Fesenko, and M. Vazquez, Appl. Phys. Lett. **98**, 232507 (2011).

[20] Y. Henry, K. Ounadjela, L. Piraux, S. Dubois, J. M. George and J. L. Duvail, Eur. Phys. J. B **20,** 35 (2001).

Chapter 4: Magnetic Reversal Processes, Analytical Calculations

4.1. On the magnetization reversal in nanowires: a micromagnetic overview

Magnetization reversal in macroscopic systems can take place by magnetization rotation and by domain walls displacement when the size of the particle is large enough to bear a multi-domain structure. The single domain structure is determined by a critical size at which the stored energy required to form a domain wall is balanced by the reduction in magnetostatic energy of the single domain state. In the case of a cylindrical wire with uniaxial longitudinal anisotropy, a long domain wall can be formed when the diameter of the wire is larger than the wall width. A first estimation of that critical diameter, D_{sd}, was derived in pioneering works.[1] It can be expressed as

$$D_{sd} = 2\sqrt{\frac{6A}{N_{//}M_s^2}\ln\left[\frac{2D_{sd}}{a}-1\right]}, \qquad (4.1)$$

where A is the exchange constant, M_s the spontaneous magnetization and a is the interatomic distance. The demagnetizing factors along the wire axis, $N_{//}$, and its perpendicular direction, $N_\perp$, can be approximated by those of a prolate spheroid as[2]

$$N_{//} = \frac{4\pi}{A_r^2-1}\left[\frac{A_r}{2\sqrt{\left(A_r^2-1\right)}}\ln\left(A_r+\sqrt{A_r^2-1}\right)-1\right], \qquad (4.2.a)$$

$$N_\perp = \frac{4\pi - N_{//}}{2}, \qquad (4.2.b)$$

where the aspect ratio (length, L, to diameter, D) of the wire is given by $A_r=L/D$, wire. An effective longitudinal uniaxial anisotropy energy density, $K_{//}$, can be labelled as:

$$K_{//} = K_D + K_{ca} = \frac{1}{2}\left(N_\perp - N_{//}\right)M_s^2 \pm K_{ca} \qquad (4.3)$$

Where K_D is the shape anisotropy term and the crystalline term, K_{ca}, takes positive or negative sign when the corresponging magnetization easy axis is parallel (//) or perpendicular (⊥) to the wire axis.

In the case of a single domain structure, the matter about which is the particular magnetization rotational reversal mode in elongated nanowires is a classical micromagnetism issue that is nicely described in classical references.[1,3-5] In a first approximation, the Stoner-Wohlfahrt model has been essentially considered to interpret the reversal mechanism in nanowire arrays.[6] This classical model assumes the nanowires to be elongated non-interacting particles, where the parallel coercivity, $H_c^{//}$ (applied field parallel to the wire axis) is simply evaluated considering the demagnetizing factor of a prolate spheroid. Nevertheless, for Co and Co-base nanowire arrays, it should be considered that both the magnetocrystalline anisotropy and the magnetostatic interactions among nanowires cannot be neglected.

In the case of long cylinders, when the applied field is parallel to the nanowire axis, two main magnetization rotation modes have been considered: i) Homogeneous or in-unison coherent rotation, and ii) Magnetization curling. Self-demagnetizing, magnetocrystalline and exchange energy terms compete to determine the most energetically favourable mode. In addition, in the present case of arrays of nanowires, magnetostatic interactions among them play an important role.[7-9]

For the coherent rotation mode, a general expression for the nucleation field, $H^C{}_n$, of a reversed domain can be established as[10]

$$H^C{}_n = \frac{2K_{ca}}{M_s}\left(N_\perp - N_{//}\right)M_s\left(1-\frac{3}{2}f\right) \tag{4.4}$$

where the second term on the right-hand side denotes the shape anisotropy field corrected by the magnetostatic interactions, which depend on the filling factor, f, or density of nanowires. Here, a simple expression to account for the average interaction field in the nanowire array[11] is considered. Where the filling factor is given by[12]

$$f = \frac{2\pi}{\sqrt{3}}\left(\frac{D}{2D_{\text{int}}}\right)^2 \tag{4.5}$$

where D is the pore diameter and D_{int} is the center-to-center nanowire distance.

On the other hand, the nucleation field in the magnetization vortex mode (curling), can be express as [10]

$$H^V{}_n = \frac{2K_{ca}}{M_s} - N_{//}M_s\left(1-\frac{3}{2}f\right) + \frac{8Aq^2}{D^2M_s}, \tag{4.6}$$

where the third term on the right-hand side represents the field necessary to overcome exchange forces. For a cylindrical geometry, Shtrikman *et al.*[13] have obtained that the parameter q is given by $q^2 = 1.08\pi$. Notice that in opposition to coherent rotation, for the vortex mode, $H^V{}_n$ depends on the square inverse diameter of the wire. A critical diameter, D_{cr}, has been considered for the transition between coherent and curling modes[5]

$$D_{cr} = \frac{2q}{M_s}\sqrt{A/N_\perp}, \tag{4.7}$$

For $D < D_{cr}$ the preferred mode is coherent rotation, while for $D > D_{cr}$ curling rotation is expected.

Values of the critical diameter of single domain structures according to eq. (4.1) are collected in Table 1 for selected nanowires taking $M_s(Co)$ = 1400 emu/cm^3, $A(Co)$=3.1x10^{-7} Jm^{-3}, a_{Co} = 0.25 nm, and $M_s(Co_{50}Ni_{50})$ = 950 emu/cm^3, $A(Co_{50}Ni_{50})$ = 1.1x10^{-7} Jm^{-3}, $a_{\mathrm{Co_{50}Ni_{50}}}$ = 0.27 nm.[14] It should be noted that single domain structure can be assumed, and consequently a rotational magnetization process, for most of the cases except for NWs with reduced aspect ratio (i.e., the nanopillar with D ~ 75 nm and L ~120 nm).

For small nanowire diameters ($D < D_{cr}$), the preferred mode is coherent rotation, while for larger sizes ($D > D_{cr}$) curling rotation is expected. According to the D_{cr} values in Table 1, all the nanowires should reverse magnetization by curling since, $D > D_{cr}$, except for the small aspect ratio nanowires, where even some contribution from domain wall motion could be also be present. A finer fitting could be achieved considering the contribution of non-ideal mechanisms. That includes the nucleation of reversed magnetization at very local regions around local inhomogeneities of composition, or at structure or surface defects.[15, 16] In these samples, the magnetocrystalline anisotropy field has a relevant role. As it has been mentioned in Chapter 3, when there is a (l00)-*hcp* Co crystal texture phase, a preferential direction of the *hcp* *c*-axis perpendicular to the nanowires axis is induced. Therefore, the competition between shape anisotropy K_D (// to the nanowires) and K_{ca} (Co-*hcp*) (⊥ to the nanowires) is relevant. Assuming K_{ca}(Co-*hcp*) ≈ 4.5×10^5 Jm^{-3}as for bulk Co,[17] the effective parallel anisotropy is calculated by eq. (4.3). The nucleation field, $H^C{}_n$, from eq. (4.4) takes a moderate value although higher than the experimental value of the experimental H_c.

For short *fcc*-Co sample, with K_{ca}(Co-*fcc*) ≈ 6.3×10^4 Jm^{-3},[17] a higher $K_{//}$ is comparatively obtained in spite of the reduction in shape anisotropy. Similarly, a net parallel effective anisotropy is calculated for $Co_{50}Ni_{50}$ with ($K_{ca}(Co_{50}Ni_{50})$ ≈ -1.1×10^3 Jm^{-3}.[17]

As observed in Table 1, calculated nucleation field values according to the coherent rotation model are higher than those of coercivity, H_c, experimentally found. Nevertheless, calculated nucleation field according vortex mode does not fit perfectly with experiments. For the longer Co nanowire arrays, it is obtained a nucleation field which in this case is even smaller than experimental coercivity. That indicates that it is considered an overestimated strong perpendicular crystalline anisotropy, seemingly as a consequence of the actual polycrystalline character of such long nanowires. In the case of shorter Co and longer $Co_{50}Ni_{50}$ nanowire arrays, it is obtained high calculated values although closer to experimental coercivity than through the coherent rotation model.

Table 1. Critical diameters, and estimated and experimental coercivity, H_c, for selected nanowire arrays.

Nanowires (L, D)	D_{sd} (nm) (kA/m)	D_{cr} (nm)	$K_{//}$ (e-1J/m^3)	H_n^C (kA/m)	H_n^V (kA/m)	H_c
hcp Co (2.5 μm, 35 nm)	1350	18	1.5	213	5	50
fcc Co (120 nm, 35 nm)	110	19	4.8	487	245	138
hcp Co (120 nm, 75 nm)	50	21	-2.5	---	---	11
fcc $Co_{50}Ni_{50}$ (2 μm, 35 nm)	2100	27	2.2	376	205	131

4.2. Angular dependence of coercivity

An alternative way to obtain information about the actual rotational magnetization reversal mechanism is the study of the angular dependence of magnetic properties, particularly of coercivity and remanence, M_r. It should be firstly emphasized that the critical diameter in eq. (4.7) is defined for the case when the field is applied parallel to the nanowires axis. For fields making a given angle, θ, with the nanowire axis, D_{cr} shifts towards higher values.

Recent analytical calculations [18] have lead to determine the angular dependence of three main idealized modes of magnetization reversal process: coherent rotation mode (*C*) with all the spins rotating simultaneously, the vortex wall mode (*V*), in which spins reverse progressively via propagation of a vortex (curling) domain wall (these two modes have been discussed above), and the transverse wall mode (*T*) in which spins reverse progressively via propagation of a transverse domain wall.

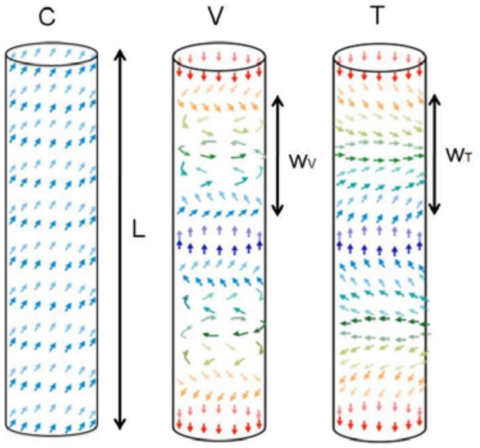

Fig.4.1. Magnetization reversal modes in nanowires. The arrows represent the orientation of magnetic moments within the wire. Left: coherent rotation mode, *C* Center: vortex rotation mode, *V*, with a domain wall of thickness w_V. Right: transverse rotation mode, *T*, with a domain wall of thickness w_T.

The classical angular dependence of the nucleation field for a coherent magnetization reversal was calculated by Stoner-Wohlfarth [6, 14] and gives

$$H_n^C(\theta) = -\frac{2(K_D(L\,) + K_{ca})\sqrt{1-t^2+t^4}}{\mu_o M_s^2(1+t^2)} M_s \quad , \tag{4.8}$$

where $t = \tan(\theta)^{1/3}$ with θ being the angle between the long axis of the wire and the applied field, M_s is the saturation magnetization and L is the length of the wire. Besides, $K_D(L) = \frac{1}{4}\mu_o M_s^2\left[1-3N_z(L)\right]$ is the shape anisotropy constant and K_{ca} denotes the magnetocrystalline anisotropy constant and the demagnetizing factor of a wire along the *z* axis, $N_z(L)$, has been previously obtained.[19]

Landeros *et al.*[20] calculated the total energy for the transverse reversal mode considering the sum of exchange and dipolar contributions. Then, they minimized the energy with regard to the domain wall width (ω_T). The calculation of nucleation or coercive field was derived by Escrig *et al.*[18] assuming that the magnetization reversal by means of the nucleation and propagation of a transverse wall is equal to the nucleation field of an equivalent system with an effective volume that reverses its magnetization by coherent rotation. Then, the Stoner-Wohlfarth model can be adapted to describe the angular dependence of a transverse reversal mode by replacing the length of the whole structure by the reduced length of the involved domain wall with width ω_T

$$H_n^T(\theta) = -\frac{2(K_D(\omega_T)+K_{ca})\sqrt{1-t^2+t^4}}{\mu_o M_s^2(1+t^2)} M_s \ , \tag{4.9}$$

where $K_D(\omega_T) = \frac{1}{4}\mu_o M_s^2\left[1-3N_z(\omega_T)\right]$ is the shape anisotropy constant. It is important to mention that the expressions for $H_n^T(\theta)$ and $H_n^C(\theta)$ differ only by the length. In the coherent reversal, *L* represents the total length of the wire, and then the coercivity varies with the length of nanowires. However, in the transverse mode, and because ω_T is nearly independent of the length of the wire, as shown by Landeros *et al*, [20] the coercivity is also independent on the length. Then, for long enough wires, ($L > \omega_T$), the transverse mode will always exhibit a lower coercivity, irrespective of *θ.* As shown in the Stoner-Wohlfarth model, the coercivity for coherent and transverse reversal modes expression can be written as a function of the nucleation field as

$$H_c^{C(T)}(\theta) = \begin{cases} \left|H_n^{C(T)}(\theta)\right| & 0 \le \theta \le \pi/4 \\ 2\left|H_n^{C(T)}(\pi/4)\right| - \left|H_n^{C(T)}(\theta)\right| & \pi/4 \le \theta \le \pi/2 \end{cases} \tag{4.10}$$

Thus, in very short wires $(L \approx \omega_T)$ the high energy cost involved in the creation of a domain wall is responsible of the coherent rotational magnetization reversal.

The angular dependence of the curling nucleation field in a prolate spheroid has been calculated first by Aharoni.[21] The effect of adding a magnetic anisotropy is essentially the same as that of changing the shape anisotropy by changing the aspect ratio. The effect is far from being negligible, and the anisotropy must be taken into account. Thus we obtain the following expressions for the nucleation field

$$H_n^V(\theta)\cos(\theta-\gamma) = (N_x(L)\sin^2\gamma + N_z(L)\cos^2\gamma - c - d(3\cos^2\gamma - 1))M_s , \tag{4.11}$$

$$H_n^V(\theta)\sin(\theta-\gamma) = \left((N_x(L) - N_z(L) + d)\frac{\sin 2\gamma}{2}\right)M_s \ , \tag{4.12}$$

where $c = \dfrac{q^2 L_{ex}^2}{R^2}$, $d = \dfrac{K_{ca}}{\mu_o M_s^2}$, $L_{ex} = \sqrt{\dfrac{2A}{\mu_o M_s^2}}$ is the exchange length, R the radius of the wire and γ is the angle at which the nucleation starts, measured from the wire axis. To obtain the nucleation field, $H_n^V(\theta)$, it can be simultaneously solved numerically equations (4.11) and (4.22) for each applied field angle, θ. As pointed out by Aharoni, a jump of the magnetization for an isolated system occurs at or near the vortex nucleation field. Therefore, the coercivity is quite close to the absolute value of the nucleation field and it is assumed here, as in other studies[22] that in the V mode $-H_n^V$ is a good approximation to the coercivity H_c^V.

In order to analyze the actual magnetization reversal processes in the framework of the models discussed above, the full angular dependence of hysteresis loops was measured in a number of nanowire arrays. The experimental coercivity can be compared with the expected evolution assuming different possible reversal modes: coherent, transverse and vortex wall. In the following two sections, it will be analyzed the angular dependence of H_c for the samples presented in Sections 3.3 and 3.4.1.

4.2.1. Fitting Co textured nanowires

Figures 4.2 illustrates the experimental curves and the calculated fittings for nanowire arrays (D_{int} ~ 105 nm, D ~ 50 nm) with textures in the (002) [Fig. 4.2 (a), (c)] and (100) [Fig. 4.2 (b), (d)] crystal planes. The results for nanowires with L ~ 3 and 30 μm are presented in Fig.4.2 (a-b) and Fig.4.2 (c-d), respectively. Note that for both crystal textures, as well as for (101) crystal texture, the transverse domain wall propagation possesses much lower coercivity than that of the coherent and curling process for the identical anisotropy value. The best fittings are obtained for magnetocrystalline anisotropy constants, K_{ca}= 18.5x10^4 J/m^3, 7.4 x10^4 J/m^3 and -1.23 x10^4 J/m^3 respectively for (002), (101) and (001) textured peaks. Note that negative K_{ca} values are interpreted as magnetocrystalline anisotropy exhibiting in-plane easy axis, perpendicular to the nanowire axis. As expected, the strength of the anisotropy evolves from strongly longitudinal for (002) texture to weak perpendicular anisotropy for (001) texture. On the other hand, the shape anisotropy constant takes similar values: 6.03, 6.11 and 6.14 x 10^5 J/m^3 respectively for nanowires 3, 8 and 30 μm long, this suggests that the changes in the magnetic behaviour of these samples are expected to be dependent mainly to the magnetocrystalline properties.

Analytical calculations for arrays of nanowires with increasing length (up to 30 μm) show also that magnetization reversal is better fitted to experimental data through transverse domain wall-like mode [see Fig. 4.3]. It is also observed that the magnetocrystalline anisotropy constant becomes weaker as the length of the wires increases. That is a consequence of the less textured crystalline structure of very long wires as discussed in Section 3.3 [Fig. 3.2(c)].

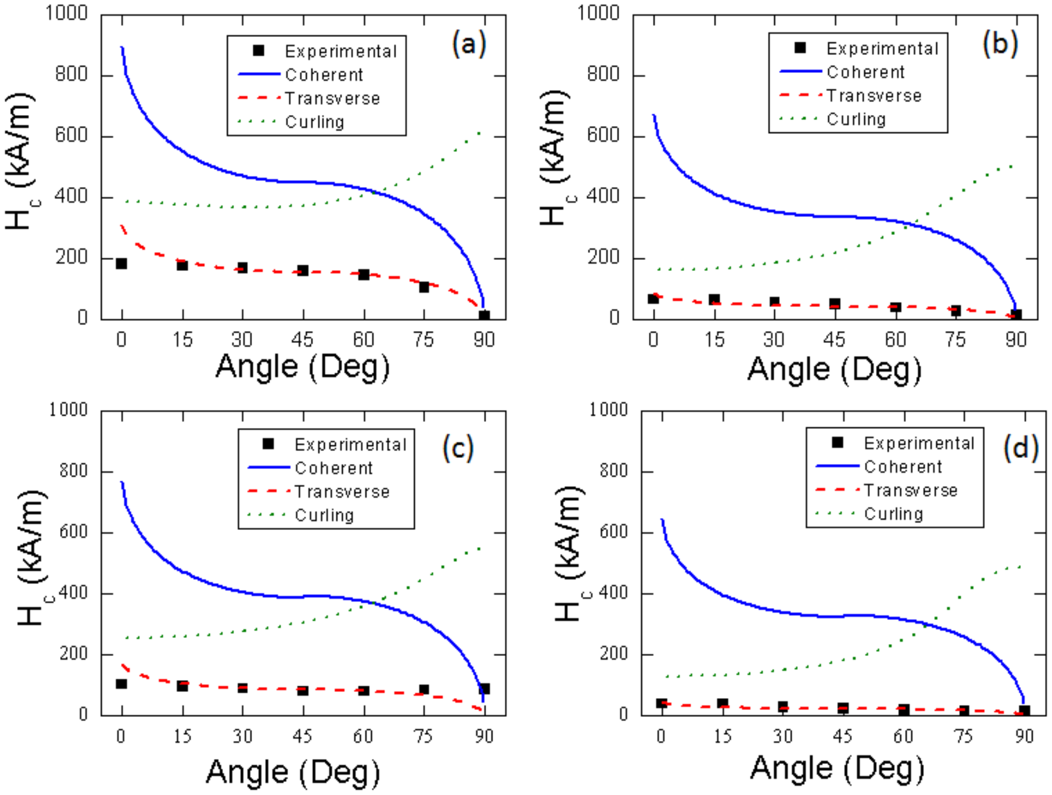

Fig. 4.2. Experimental (black squares) and calculated angular dependence of coercivity for arrays of 3 and 30 μm long Co nanowires [(a), (b) and (c), (d), respectively] with (002) *hcp*- phase texture [(a) and (c)] and (100) perpendicular *hcp*-phase texture [((b) and (d)].

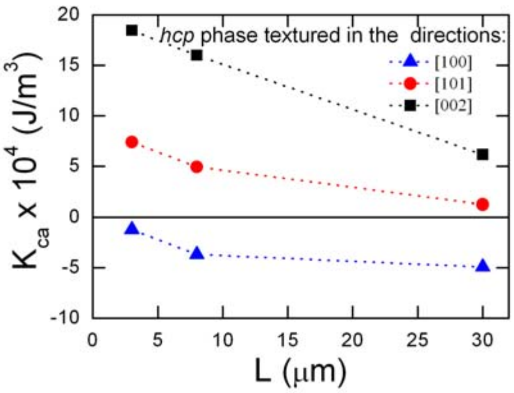

Fig. 4.3. Fitted magnetocrystalline anisotropy constant for NWs of indicated texture as a function of their length.

It should be mentioned that the effect of magnetostatic interactions between wires depends on their length.[23] The present model does not consider these interactions which may be reflected as a perturbation of the crystalline anisotropy of the material. On the other hand, the grain size varies with the length, which could affect the value of the anisotropy constant. Other factors that have not been considered in this analytical calculations model include thermal instabilities, which have a large effect on thin particles, potential irregularities in the shape of the wires, and uniformity in the length of the same.

Micromagnetic simulations in Co wires of the diameter relevant to the present study have reached to the conclusion that magnetization should switch through more complex mechanisms involving magnetization curling (vortex-like) modes depending on strength and orientation of crystalline anisotropy.[24] However, as it was pointed by Hertel and Kirschner,[25] the magnetization reversal process is quite complex and the difficulty arises from the central axis, where the magnetization switches in a discontinuous fashion. Thus, the switching process involves the injection of a magnetic point singularity (Bloch point) into the cylinder and the formation of micromagnetic drops, i.e., isolated, non-reversed regions. In particular, this agrees with the results present in Chapter 6, where it is observed that for *hcp*-phase Co nanowires the remanence is characterized by a longitudinally magnetized core and a circularly magnetized shell. Although, the angular dependence of the curling nucleation field has been analytically modeled by Aharoni,[21] he only obtained an expression for the nucleation field in a prolate spheroid regardless of the complexity of the vortex reversal mode observed in numerical simulations.

4.2.2. Fitting CoNi nanowires

In the previous Section the studied samples were prepared modifying the pH during the electrodeposition in order to obtain *hcp* Co with different crystal textures, i.e., different magnetocrystalline behaviors. Now, it is considered the case of Co_xNi_{1-x} nanowires ($0 \leq x \leq 1$, $D_{int} \sim 105$ nm, $D \sim 35$ nm, $L \sim 2.5$ μm) and the objective was to tune the Co-alloy composition by changing the Ni content, thus resulting in a balance between the *hcp/fcc* phases for the control of the magnetocrystalline contribution, looking forward the reinforcement of the longitudinal effective anisotropy.

Figure 4.4(a) illustrates the results for Co nanowires. Although all three modes are in principle possible, the corresponding system will reverse its magnetization by whichever mode opens an energetically accessible route first, that is, by the mode that offers the lowest coercivity. To obtain a good agreement with experiments it was considered for the calculations a magnetocrystalline anisotropy with an out-of-plane anisotropy constant of -8.62×10^4 J/m^3, which corresponds to a perpendicular easy plane. In this case it is concluded that, independent of the angle, the magnetization reversal is driven by the nucleation and propagation of a transverse wall. Fig. 4.4(b) shows the results for $Co_{50}Ni_{50}$ sample where similar calculations were performed. In this case, a better agreement with experiments is obtained by using a longitudinal anisotropy constant of 4.89×10^3 J/m^3, reflecting an axial easy axis. Again, the magnetization reverses by means of a transverse wall, although for angles around 60º the curling and the transverse reversal modes showed a very similar coercivity. As it has been mentioned before, thermal instability or shape irregularities, which are not considered in this model, can bring the system to adopt a vortex reversal mode. Similar results were obtained for $Co_{80}Ni_{20}$ and Ni nanowires [Fig. 4.4(c) and (d), respectively].

Regarding the lack of perfect fitting for angles close to 0º and 90º, it is important to note that this model does not consider inter-element interactions with surrounding wires. These interactions are responsible for an additional antiferromagnetic or ferromagnetic contribution to the field for 0º and 90º, respectively.

Fig. 4.5 collects the values of the crystalline anisotropy used in the calculations to obtain the best agreement in the fitting with experimental results. From this figure it is observed that the easy axis evolves from perpendicular (in-plane of the membrane) in the case of Co nanowires to longitudinal (parallel to the wires axis) in the case of Ni rich alloy samples.

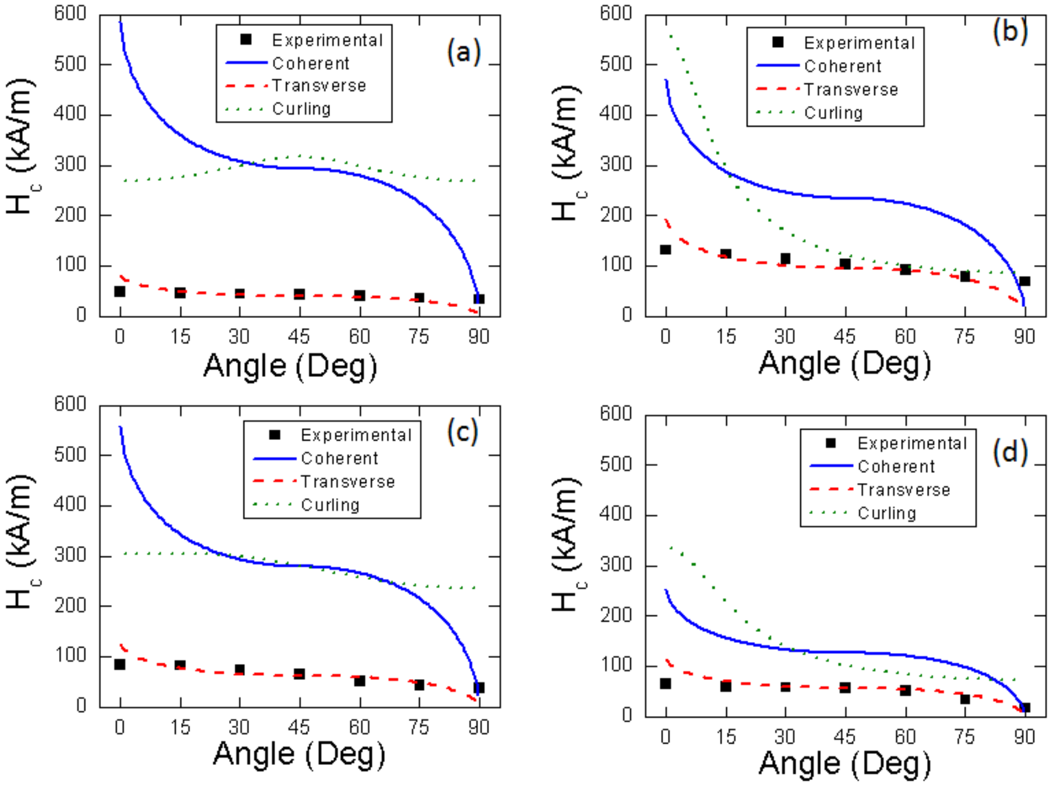

Fig.4.4. Experimental and calculated (according to the different modes) angular dependence of coercivity for (a) Co, (b) $Co_{50}Ni_{50}$, (c) $Co_{80}Ni_{20}$ and (d) Ni nanowire arrays.

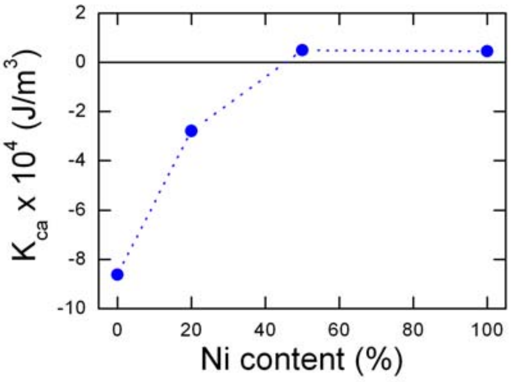

Fig. 4.5. Fitted magnetocrystalline anisotropy constant as a function of Ni concentration.

The effect of crystalline anisotropy on a particular magnetic element is to modify its fundamental magnetic properties, like its coercivity and remanence. When the curling and the transversal reversal modes have similar coercivities, the crystalline anisotropy could be responsible for a transition between both modes. However in the cases under consideration the effect has not been observed and it can be conclude that, independent of the angle, the reversal is driven by the nucleation and propagation of a transverse wall. It is important to note that obtained magnetization reversal mode is not intrinsic of Co or CoNi nanowires but of a given shape (geometry) and crystalline anisotropy.

4.3. First Order Reversal Curves, FORC

In order to reach further insight into the magnetic properties of the systems, it has been obtained First Order Reversal Curves, FORC, from a set of minor hysteresis loops.

While major hysteresis loops (*MHL*) provide information regarding the global (average) behavior of the magnetic system, FORC measurements are more appropriate to investigate the processes taking place during the magnetization reversal. In particular, FORC measurements proved to be valuable to address the role of the distinct crystallographic contributions present in nanowires,[26] being therefore complementary to the magnetic and structural characterizations presented.

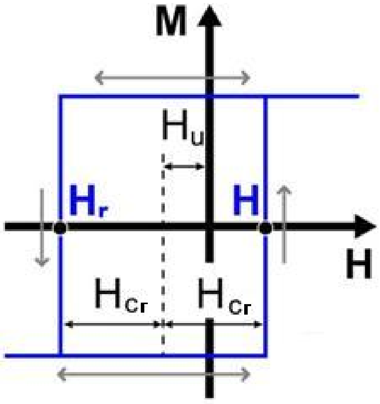

Fig. 4.6. Mathematical hysteron from the classical Preisach model. The magnetization switches down, abruptly, at $H_r = -(H_{cr} + H_u)$, and switches back up for a certain $H = (H_{cr} - H_u)$ value. The H_{cr} and H_u parameters, respectively represent the coercivity and the bias field of the mathematical hysteron.

The FORC method is based, at its origin, on the classical Preisach model,[27] a mathematical model where hysteresis can be modelled as a set of elementary processes, or operators, called hysterons and characterized by two parameters, H_{cr} and H_u (Fig. 4.6). It is important to note that these hysterons do not necessarily have a physical significance. Indeed, when applying the FORC method to a physical system, one does not need to use the classical Preisach model to interpret the result. Several different approaches are possible, either based on physical hypothesis. Spinu et *al.*[28] proposed that, in the specific case of nanowire arrays in an out of plane magnetic field, the narrow distribution along the H_{cr} axis may be interpreted as a small distribution of coercive forces of wires of the same composition and geometrical parameters, and that the very broad distribution parallel to the H_{u} axis represents the large interaction fields acting on the wires. Thus, the hysterons might have a physical meaning in this case. That is, they might be interpreted as individual the wires. Besides, Berón et *al.*, [29] showed that the peak in the H_{cr} direction is close to the average value of the nanowire coercivity and that the half width of the distribution in the H_{u} direction provides information on the magnetostatic interactions.

The goal of any FORC measurements is to retrieve the H_{cr} and H_u parameters of each hysteron of the system. To achieve this, the system is first magnetically saturated along a positive direction, in order to put all the magnetization of the hysterons in the "up" position. Then, the external applied field, H, is lowered until a point called reversal field (H_r), which switches "down" the magnetization of some hysterons, depending upon their H_{cr} and H_u parameters. Then, the field H is increased again and the magnetization M is measured. The difference of magnetization between the applied field and the reversal field is directly proportional to the amount of hysterons that switched back "up". This kind of minor hysteresis curve is called first-order reversal curve. The information about all hysterons in the system, the FORC distribution, ρ, can be obtained by generalizing the process, i.e. applying a second-order mixed derivative of M on a set of FORCs beginning at different H_r, [30]

$$\rho(H,H_r) = -\frac{1}{2}\frac{\partial^2 M(H,H_r)}{\partial H \partial H_r} \text{ , for } H > H_r \tag{4.13}$$

For clarity, H_u and H_{cr} are defined as follows

$$H_u = \frac{H+H_r}{2}, \qquad H_{cr} = \frac{H-H_r}{2}, \tag{4.14}$$

In addition, the characterization of the reversible processes can be done through the calculation of a reversibility indicator (grey scale strip in the diagrams), ranging from white to black, corresponding to fully reversible or irreversible behaviour, respectively.[30] This indicator is obtained from the slope (χ_F) of the minor loops at each H_r, and reflects the reversibility of the process, normalized to the susceptibility (χ_{Hyst}) of the *MHL* upper branch at the same H_r:

$$\eta(H = H_r) = \frac{\chi_F(H = H_r)}{\chi_{Hyst}(H = H_r)}, \tag{4.15}$$

4.3.1.FORC diagrams in Co and CoNi nanowires

In this Section, it is presented a set of 100 FORC cycles, covering the region between the closure points of the hysteresis diagrams (field ranging from -398 kA/m to 398 kA/m). The magnetic field was applied parallel and perpendicular to the NWs longitudinal axis, and a reversal field step (ΔH_r) of 100 Oe was used.

Figure 4.7 shows the parallel and perpendicular FORC diagrams for Co and $Co_{50}Ni_{50}$ NW arrays. Each diagram consists of a contour plot of ρ with a colour scale from blue (minimum) to red (maximum).[31] In this representation, the H_u axis corresponds to the interaction field and H_{cr} denotes the coercive field, which may not correspond directly to the H_c obtained from *MHL*.[32] Besides, from the FORC diagram, one can obtain the coercivity $<H_c^F>$ as the H_c position of the FORC distribution maximum.

Figures 4.7(a) and 4.7(b) show respectively the parallel and perpendicular FORC diagrams for Co NWs. The parallel FORC diagram in Fig. 4.7(a) exhibits two distinct distributions. The main one, along H_u axis, can be ascribed to the magnetostatic interactions among nanowires. Each nanowire in the array interacts with the stray fields produced by the neighbouring wires, and experiences an antiferromagnetic-like coupling,[29] which acts as a macroscopic demagnetizing field.[33] In this regard, the effect of the magnetostatic interactions is equivalent to that of a perpendicular (in-plane) magnetic anisotropy. Thus, both perpendicular magnetocrystalline anisotropy [(100) *hcp*-Co phase] and magnetostatic interactions reinforce themselves against the geometrical shape anisotropy. Enhanced dipolar interactions are also expected in pure Co nanowires as a consequence of a high saturation magnetization. The second distribution (on parallel Co FORC), observed along the H_{cr} axis, should be associated with a harder magnetization reversal process. As discussed by Pirota *et al.*[34], the broadening of this distribution can be ascribed to the existence of a *fcc*-phase, which requires a higher field to reverse magnetization leading to the visible extended branch over H_{cr}. Notice that a clear maximum at $<H_c^F(fcc)> \approx 302$ kA/m for a 20% (volume) *fcc* contribution in 1.7 μm long Co nanowires has been also reported.[26]

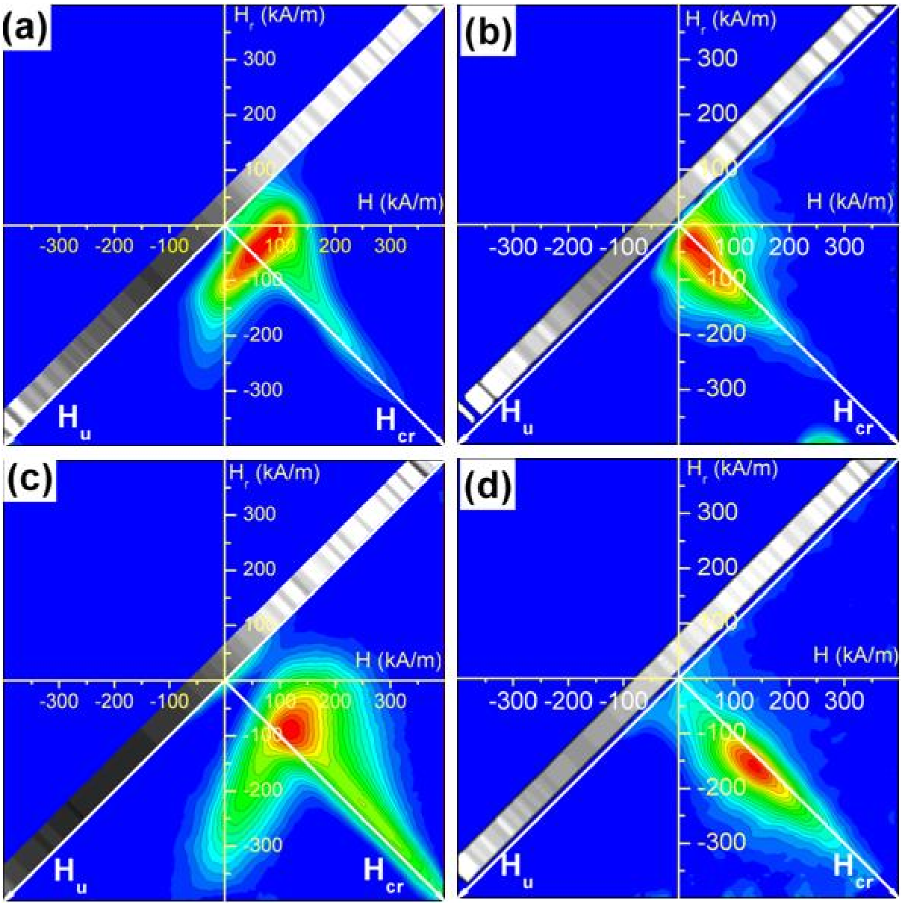

Fig. 4.7. FORC diagrams for (a), (b) Co and (c), (d) $Co_{50}Ni_{50}$ NWs, obtained with the applied magnetic field parallel (a),(c) and perpendicular (b),(d) to the NW axis. The color scale goes from blue (representing the minimum) toward red (maximum values). The gray-scale strip in the diagrams denotes the reversibility indicator which ranges from white to black, corresponding to fully reversibleand irreversible behavior, respectively.

In the case discussed here, the absence of a maximum in this second distribution confirms a rather small contribution from *fcc* crystallites (lower than 10 %). In turn, the perpendicular FORC diagram in Fig. 4.7(b) shows less complex structure. A single main coercitivity distribution is observed along the H_{cr} axis which is attributed to the reversal of the crystallographic *hcp*-phase being the visible broadening of ρ originated by the nanowire polycrystalline nature, as concluded from the XRD data (Section 3.4.1.).

For $Co_{50}Ni_{50}$, the parallel and perpendicular FORC diagrams are shown in Figures 6(c) and 6(d), respectively. For the parallel FORC diagram, two distributions are again observed exhibiting a wider spread over both H_u and H_{cr} axes in comparison with those of Co nanowires. In this case, the presence of Co still favors the magnetostatic interactions among NWs, which is reflected in the elongation along H_u.

However, with increasing Ni content the *fcc* phase increases, translated by the presence of a broader distribution along the H_{cr} axis. Accordingly, the defined maximum of the coercivity distribution is shifted to higher fields in comparison with Co nanowires. In addition, the maximum of ρ over H_{cr} is also detected at higher field (around 231 kA/m) which can be attributed to the irreversible magnetization reversal of the *fcc* grains (lying parallel to the applied magnetic field).[31] Such large irreversible contribution strongly favors magnetization reversal by nucleation and propagation of a transverse domain wall, as inferred from the analytical calculations. In contrast, the perpendicular FORC diagram [Fig. 4.7(d)] shows mainly a broad distribution along H_{cr} which supports the transition from *hcp* to *fcc* phase, suggesting that the nanowires may present a mixture of both *fcc* and *hcp* structures.

Finally, the reversibility indicator for parallel FORC diagrams denotes clearly a wider distribution of irreversible (dark grey) processes for $Co_{50}Ni_{50}$ NWs, attributed to the reduced contribution of *hcp* crystallites and correspondingly reduced perpendicular anisotropy, as discussed above. Regarding the perpendicular FORC diagrams, stronger irreversibilities are observed at low field for Co NWs. However, for $Co_{50}Ni_{50}$ NWs the irreversibility distribution extends over a wider spectrum at higher fields probably associated with the observed higher coercivity in *MHL* measurements.

4.4. Summary

In this chapter, it was introduced a summarized introduction on the magnetization reversal modes depending on the wires diameter. Then analytical calculations considering the coherent, transverse and vortex modes were discussed.

I should be emphasized the point that magnetocrystalline anisotropy determined by different parameters, as discussed in previous chapters, plays an important role in the magnetization reversal problem. The presence of a Co *hcp*-phase leads to an important competition between shape and magnetocrystalline anisotropies, which translates into a weakly defined magnetization easy axis along the NW longitudinal direction. Modifying the electrochemical parameters in the electrodeposition of Co, could leads to a modification of the crystal structure, which results in a strong influence of the effective anisotropy of the system. On the other hand, with increasing Ni content in a Co-alloy system the net crystalline anisotropy drastically decreases and shape anisotropy becomes dominant.

The angular dependence of coercivity has been modelled considering the different possible reversal modes. The propagation of a transversal wall gives the best fitting with experimental observations for all the NWs Co and the alloy compositions.

i) Co textured nanowires: From the fitting, the strength and easy direction of the magnetocrystalline anisotropy constant is derived to depend on the *hcp*-phase texture. The magnetocrystallin easy axis evolves from longitudinal (parallel to the wires axis) in the case of nanowires with the *hcp* (002) texture to perpendicular (in-plane of the membrane) in the case of nanowires with *hcp* (100) texture.

ii) CoNi-alloy nanowires: Fitted values of magnetocrystalline anisotropy confirm the evolution from perpendicular to longitudinal orientation of the magnetization easy axis.

iii) Finally, FORC analysis has given additional information on the role of each crystallographic phase present in the NWs, evidencing the presence of a *hcp/fcc* mixture in all samples. Moreover, the appearance of an irreversible magnetization reversal promoted by the presence of higher *fcc*-phase as Ni content increases strongly correlates with the analytical calculations of H_c angular dependence.

4.5. References

[1] E. H. Frei, S. Shtrikman, and D. Treves, Phys. Rev. **106**, 446 (1957).

[2] J. A. Osborn, Phys. Rev. **67**, 351 (1945).

[3] W. F. Brown, Jr., Micromagnetics (Krieger Publ. Co, New York, 1978).

[4] A. Aharoni, Introduction to the Theory of Ferromagnetism (Oxford University Press, Oxford, 1996), Chap. 9.

[5] H. Kronmüller and M. Fähnle, Micromagnetism and the Microstructure of Ferromagnetic Solids (Cambridge University Press, Cambridge, 2003).

[6] E. C. Stoner and E. P. Wohlfarth, Philos. Trans. R. Soc. Lond., Ser. A 240, 599 (1948) [reprinted in IEEE Trans. Magn. 27, 3475 (1991)].

[7] K. Nielsch, R. B. Wehrspohn, J. Barthel, J. Kirschner, U.Gösele, S. F. Fischer, and H. Kronmüller, Appl. Phys. Lett.**79**, 1360 (2001).

[8] M. Vazquez, K. Nielsch, P. Vargas, J. Velazquez, D. Navas, K. Pirota, M. Hernandez-Velez, E. Vogel, J. Cartes, and R. B. Wehrspohn, Physica B **343**, 395 (2004).

[9] J. De La Torre, M. Darques, T. Blon, and L. Piraux, Phys. Rev. B **77**, 014417 (2008).

[10] M. Vázquez and L. G. Vivas, Phys. Status Solidi B **248**, 2368 (2011).

[11] J. De La Torre Medina, L. Piraux, J. M. Olais Govea, and A. Encinas, Phys. Rev. B **81**, 144411 (2010).

[12] K. Nielsch, J. Choi, K. Schwirn, R. B. Wehrspohn, and U.Gösele, Nano Lett. **2**, 677 (2002).

[13] S. Shtrikman, and D. Treves, In Magnetism G. T. Rado G T and H. Suhl H Eds. New York Academic **3**, (1963).

[14] C. Tannous and J. Gieraltowski, Eur. J. Phys. **29**, 475 (2008).

[15] W. Wernsdorfer, B. Doudin, D. Mailly, K. Hasselbach, A. Benoit, J. Meier, J. P. Ansermet, and B. Barbara, Phys. Rev.Lett. **77**, 1873 (1996).

[16] D. C. Leitao, C. T. Sousa, J. Ventura, K. R. Pirota, M. Vazquez, J. B. Sousa, and J. P. Araujo, J. Magn. Magn. Mater. 322, 1319 (2010).

[17] S. Chikazumi, BT Physics of Magnetism (R.E. Krieger Publ.Co., New York, 1978).

[18] J. Escrig, J. Bachmann, J. Jing, M. Daub, D. Altbir,, and K. Nielsch, Phys. Rev. B **77**, 214421 (2008).

[19] I. Beleggia, S. Tandon, Y. Zhu, and M. De Graef, J. Magn. Magn. Mater. **272**, e1197 (2004).

[20] P. Landeros, S. Allende, J. Escrig, R. Salcedo, D. Altbir, and E. Vogel, Appl. Phys. Lett. **90**, 102501 (2007).

[21] A. Aharoni, J. Appl. Phys. **82**, 1281 (1997).

[22] Y. Ishii, J. Appl. Phys. **70**, 3765 (1991).

[23] J. Escrig, R. Lavín, J. L. Palma, J. C. Denardin, D. Altbir, A. Cortés, H. Gómez, Nanotechnology **19**, 075713 (2008).

[24] L. G. Vivas, R. Yanes, O. Chubykalo-Fesenko, and M. Vazquez, Appl. Phys. Lett. **98**, 232507 (2011).

[25] R. Hertel, J. Kirschner, Physica B **343**, 206 (2004).

[26] M. Ciureanu, F. Béron, P. Ciureanu, R.W. Cochrane, D. Ménard, A. Sklyuyev, A. Yelon, J. Nanosci. Nanotechnol.,**8**, 5725 (2008).

[27] I. D. Mayergoyz Mathematical Models of Hysteresis and Their Applications, Elsevier, Amsterdam (2003).

[28] L.Spinu, A.Stancu, C.Radu, F.Li, and J.B.W iley, *IEEE Trans. Magn.* 40, 2116 (2004).

[29] F. Béron, D. Ménard, and A. Yelon, J. Appl. Phys. **103**, 07D908 (2008).

[30] I. D Mayergoyz, J. Appl. Phys. **57**, 3803 (1985).

[31] F. Beron, L.-P. Carignan, D. Menard, and A. Yelon, in *Electrodeposited Nanowires and Their Applications*, edited by N. Lupu (InTech, 2010), p. 167.

[32] F. Beron, L. Clime, M. Ciureanu, D. Menard, R. W. Cochrane, and A. Yelon, J. Appl. Phys. **101**, 09J107 (2007).

[33] C. R. Pike, Phys. Rev. B **68**, 1044249 (2003).

[34] K. R. Pirota, F. Beron, D. Zanchet, T. C. R. Rocha, D. Navas, J. Torrejon, M. Vazquez, and M.Knobel, J. Appl. Phys. **109**, 083919 (2011).

Chapter 5: Temperature Dependent Magnetic and Transport Properties

5.1. Introduction

A number of works have been reported on the temperature dependence of the magnetic behavior in arrays of magnetic nanowires for samples with different compositions and geometries.[1-3] A noticeable modification in anisotropy strength was sometimes observed when reducing the measuring temperature. Even a change of sign (i.e. from longitudinal to perpendicular) was obtained which denotes the competition between energy terms with opposite temperature dependence. On the other hand, the reduction in size can lead to both qualitative and quantitative changes in the electrical transport in nanowires when compared to the bulk properties. While a lot of work has been reported on the magnetism in the ferromagnetic nanowires, the magneto-transport properties (in particular, the temperature dependent part) require further studies to complete a full view of involved magnetic mechanisms. [4,5]

In this Chapter the temperature dependence of magnetic behavior in Co-base nanowire arrays is considered, with particular emphasis on the magnetotransport properties as a function of temperature [$MR(T)$] of CoNi nanowires.

5.2. Temperature magnetic behavior in Co and Co-base nanowires

In Chapter 3 the characterization of hysteresis loops and their parameters, i.e., coercivity, H_c and reduced remanence ($m_r = M/M_{sat}$), at room temperature indicates the rising of an anisotropy with longitudinal magnetization easy axis when: i) the length of Co nanowires decreases or a (002) *hcp* Co crystal phase is achieved, ii) the Ni content is continuously increased and iii) the Pd content is moderately increased. This section is focused on the temperature dependence of such anisotropy and the overall magnetic behavior.

The evolution of m_r and H_c with temperature is plotted in Fig. 5.1 in the parallel, //, and perpendicular, ⊥, field configurations for Co nanowires with different lengths ($D \sim 50$ nm and $D_{int} \sim 105$ nm). For the shortest wires presented here ($L \sim 300$ nm), a longitudinal magnetization easy axis is clearly deduced from the larger values of longitudinal remanence and coercivity in the whole temperature range. This is ascribed to the dominant growth of the (111) *fcc* Co phase during the initial out of equilibrium state of the electroplating process, with a weak anisotropy, (see Section 3.5.1) whose easy axis is mainly oriented along the axis of the nanowires, leading to the predominance of the shape anisotropy. As the length of the nanowires increases, the balance between *fcc* and *hcp* Co phases gives rise to a more complex behavior with the compensation of // and ⊥ anisotropies at given temperature. Note that the small values of remanence, particularly at and just below room temperature, indicate that the effective magnetization easy axis lies neither longitudinal not perpendicular to the wires.

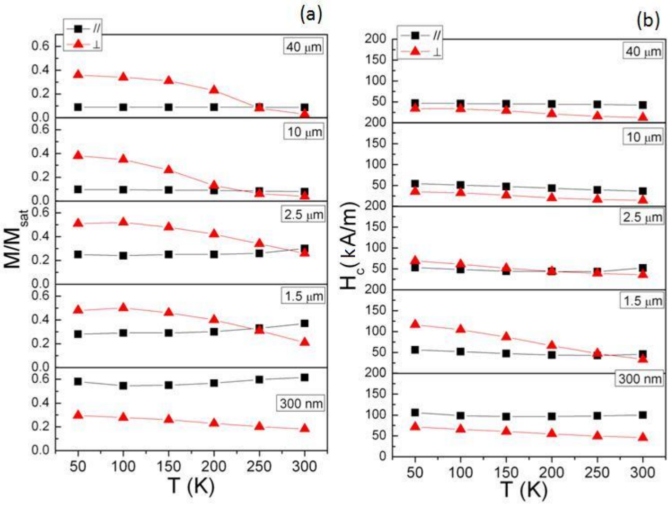

Fig. 5.1. Temperature dependence of // and ⊥ (a) reduced remanence and (b) coercivirty of arrays of Co nanowires with selected indicated length.

Figure 5.2 shows the temperature dependence of m_r for several arrays of CoNi nanowires with selected compositions (L ~ 2μm, D ~ 35 nm and D_{int} ~ 65 nm). The evolution of these magnetic parameters is depicted for both // and ⊥ configuration of the applied field. In the case of $Co_{25}Ni_{75}$ nanowires, Ni-rich sample, [Fig. 5.2(a)], we deduce that there is an effective longitudinal easy axis in the whole range of investigated temperatures where both, reduced remanence and coercivity, take higher values in the parallel applied field configuration than the perpendicular configuration. For increasing Co content, in the case of $Co_{50}Ni_{50}$ [Fig. 5.2(b)], the parallel coercivity and the parallel remanence still have the highest values through the changes of temperature, except at room temperature where m_r has about the same value for the // and ⊥ cases. For $Co_{75}Ni_{25}$ nanowires, Co-rich sample, [Fig. 5.2(c)] a crossover effect is observed from parallel to perpendicular reduced remanence. Also the perpendicular coercivity values increase in comparison with the perpendicular values for the $Co_{50}Ni_{50}$ nanowires. However, the parallel coercivity values dominate over the perpendicular ones, but modestly. While the same behavior than before is observed for m_r in the case of Co nanowires [Fig. 5.2(d)], it can be noted a crossover effect in H_c. Below 100 K the effective anisotropy of the system clearly lies perpendicular to the nanowires long axis.

As a summary of the comparison between longitudinal and perpendicular remanence and coercivity for each composition, we deduce that: (i) for high Co content, there is an evolution towards perpendicular anisotropy as temperature decreases and (ii) for high enough Ni content, the longitudinal anisotropy is well defined through the whole temperature range. Nevertheless, a crossing temperature is observed when there is the same ratio between Ni and Co contents.

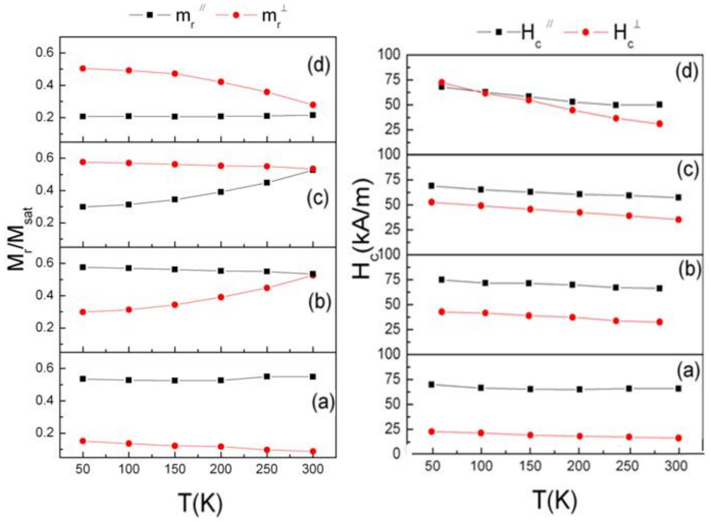

Fig. 5.2. Temperature dependence of // and ⊥ reduced remanence (left panel) and coercivirty (right panel) of arrays of (a) $Co_{25}Ni_{75}$, (b) $Co_{50}Ni_{50}$, (c) $Co_{75}Ni_{25}$ and (d) Co nanowires.

Finally, Fig. 5.3 shows the temperature dependence of of m_r for several arrays of CoPd nanowires with selected compositions ($L \sim 2\mu m$, $D \sim 35$ nm and $D_{int} \sim 105$ nm). While in Fig. 5.1, it was shown that Co nanowires (of the same geometric parameters) exhibit low coercivity values for every temperature and a dominant perpendicular anisotropy below the room temperature, it is observed that, when a small quantity of Pd is added to the system, both H_c and m_r drastically increase in the whole temperature range for the parallel applied field configuration [Fig. 5.3(a)]. Nevertheless, these magnetic parameters decrease continuously as Pd content is further increased. Also it can be noted that m_r// and $H_c^{//}$ slightly decrease with temperature when increasing Pd content and a broad minimum can be observed. In short, these results should be understood by considering the existence of a magnetic anisotropy which is strengthened for relatively modest amount of Pd.

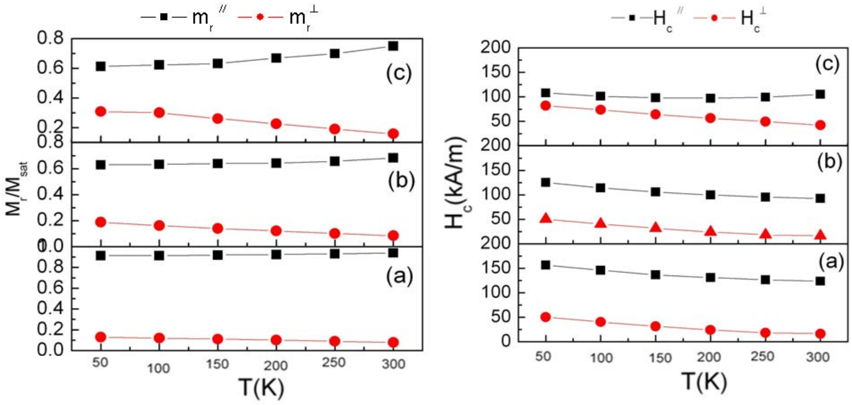

Fig. 5.3. Temperature dependence of // and ⊥ reduced remanence (left panel) and coercivirty (right panel) of arrays of (a) $Co_{88}Pd_{12}$, (b) $Co_{74}Pd_{26}$, and (c) $Co_{56}Pd_{44}$.

Through this study, the relevance of the magnetocrystalline anisotropy is emphasized by: i) the rising of perpendicular anisotropy (due to *hcp*-Co phase) with the length of Co nanowires even against an enhanced longitudinal shape anisotropy; ii) the addition of suitable elements that results in the reduction of *hcp*-Co phase: Pd in less content results in the optimum longitudinal anisotropy, while continuous increase of Ni content gives rise to moderate enhancement of longitudinal anisotropy. [6, 7]

The magnetic behavior is determined by the effective magnetic anisotropy, its strength and easy axis orientation. Such effective anisotropy is determined by the balance between crystalline (K_{an}), magnetoelastic ($K_e=\frac{3}{2}\lambda\sigma$, λ and σ are the magnetostriction and the stress, respectively) and shape ($K_s \sim \mu_o N M_s^2$, N the longitudinal demagnetizing factor) anisotropy contributions together with the magnetostatic interaction [$K_{int} \sim \mu_o(1\text{-}3f/2)M_s^2$, where f is the membrane filling factor] among nanowires. That anisotropy determines a general expression for the temperature dependence of H_c as:[6]

$$H_c(T) \approx \frac{2}{\mu_0 M_s(T)}\left[K_{an}(T) + \frac{3}{2}\lambda(\mathrm{T})\sigma(\mathrm{T})\right] + \left[N\left(1-\frac{3}{2}f\right)\right]M_s(T), \qquad (5.1)$$

where, as observed, all contributions are temperature dependent, and composition modifications give rise to changes in magnetocrystalline (i.e., *hcp* or *fcc* phases contributions) and magnetoelastic (i.e., alloy composition dependent magnetostriction) terms. At temperature well below the Curie point and neglecting the magnetoelastic contribution that expression reduces to

$$H_c(T) \approx h_{c,an} M_s^2(T) + h_{c,geom} M_s(T), \tag{5.2}$$

where each contribution to coercivity exhibits diverse temperature dependence, and $h_{c,cr}$ and $h_{c,geom}$ denote respectively the magnetocrystalline and geometry anisotropy constant contributions to coercivity. I can be noted that $h_{c,an}$ is determined by composition (e.g., *hcp* or *fcc* phases) and length of wires, while $h_{c,geom}$ is only dependent on their length.

In Fig. 5.1, the higher values of $H_c^{//}$ for short wires is mostly determined by the cylinder shape anisotropy (K_{sh} ~ 6e5 J/m^3),[8] and the presence of (111) *fcc* crystals, which reinforces the longitudinal anisotropy ($K_{an,fcc\text{-}Co}$ ~ 6e4 J/m^3at room temperature).[9] For intermediate lengths (i.e., around 2.5 µm), the stronger *hcp* phase crystalline anisotropy determines a higher value of perpendicular coercivity although it decreases more drastically with temperature than the shape contribution and a crossing temperature is thus observed. Finally, for the longer wires with enhanced shape anisotropy, longitudinal coercivity takes slightly higher value than perpendicular ones. That, together with their overall reduced values and modest temperature dependence, suggests a balance between crystalline and shape anisotropies with seemingly predominance of shape anisotropy.

For CoNi nanowires [see Fig. 5.2], the monotonous increase of longitudinal coercivity with Ni content is ascribed to the decrease of the *hcp* crystal phase, as it was discussed in Section 3.4.1. It should be mentioned that for high Ni content a significant contribution of magnetoelastic anisotropy in Eq. 5.1 is expected due to the magnetoelastic coupling between a higher magnetostriction with the mechanical stress induced by the different thermal expansion coefficients of Ni and AAO (for these experiments the Al foil had been removed).[2, 3] It is well known that fundamental magnitudes, as saturation magnetization, crystalline anisotropy constants or magnetostriction are modified by temperature. In the present case, apart from those changes it has to be taken into account that nanowires are embedded in an alumina membrane. Since each system (nanowires and alumina) exhibits different thermal expansion coefficients, thermal strains will be induced in the nanowires that finally will result in magnetoelastic anisotropy. Such complex magnetoelastic anisotropy is particularly important in the case of nanowires with high magnetostriction as Ni. In the case of Co-rich nanowires, the change of crystalline anisotropy constant with temperature seems more relevant. The contribution from changes in the shape anisotropy coming from variation in saturation magnetization seems to be relatively modest since the effect is observed well below the Curie temperature.

On the other hand, from Fig. 5.3., it is observed that a moderate Pd content increases significantly the longitudinal coercivity, due to the reduction of *hcp* at the expense of *fcc* phase [see Fig. 3.7(b)]. That is similar to the effect observed with the moderate increase of length in Co nanowires. Further increase of Pd content contributes to reduce the effective longitudinal crystalline anisotropy.

5.3. Temperature dependent magnetoresistance behavior in CoNi nanowires

5.3.1. Sample preparation for transport characterization

For the growth of the magnetic nanowires in this section, AAO templates anodized in a 0.3 M oxalic acid at 40 V resulting in nanopores with an average diameter of ~ 35 nm, separation of ~105 nm were used (see Chapter 2 for details). At the bottom of each nanopore, a non-conductive alumina barrier of ~50 nm is present, which must be removed or thinned down to allow the growth of wires by electrodeposition.[9] The barrier layer was therefore reduced to a nominal thickness of ~3 nm, originating dendrites. The pulsed electrodeposition method was then used to grow the metallic nanowires inside the AAO as decribed in Chapter 2. The dendritic channels were first filled with Au, and the main cylindrical nanopore was subsequently filled with the $Co_{50}Ni_{50}$ alloy (Fig. 5.4). As in the study of Ref .5, the studied samples are composed by distinct segments: the magnetic nanowires, Au metallic dendritic channels, and a ~3 nm alumina barrier layer (Fig 5.5.). A top Au electrode was sputtered, while the Al foil works as bottom electrode for the transport measurements.

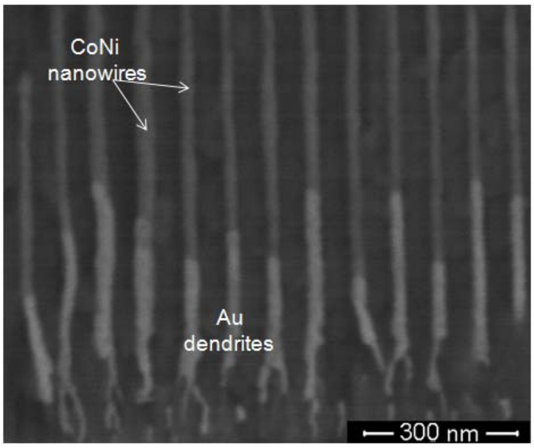

Fig. 5.4. AAO cross-section SEM image with nanowires (*D* ~ 35 nm and *L*~ 2.5 μm). Their distinct contrast enables one to distinguish between the Au present at the bottom (brighter) and the $Co_{50}Ni_{50}$ alloy on top (darker).

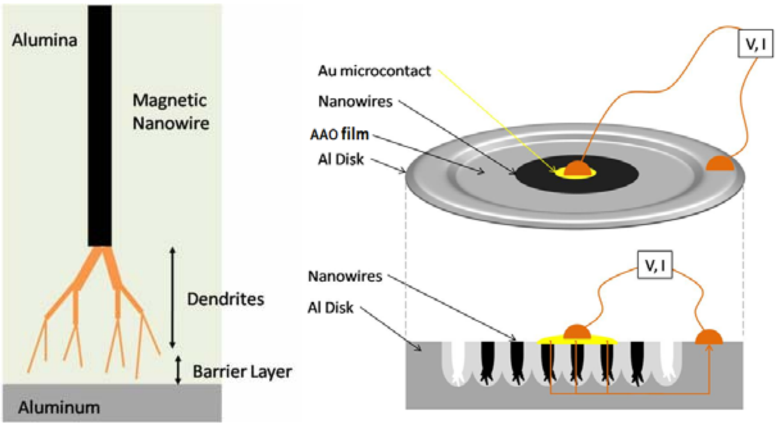

Fig. 5.5. (Left) Sketch of the distinct segments that compose a single nanowire. (Right) Drawing of the electrical contacts geometry for transport measurements, with a top Au electrode and a bottom Al foil electrode.[10]

5.3.2. Electric and magneto-transport properties

The investigation of spin dependent transport phenomena is fundamental for the development and application of spintronic.[11] One example is the giant magnetoresistance effect (GMR) which is caused by spin dependent scattering of electrons at the interfaces of exchange coupled multilayer systems.[12] Other spin dependent transport phenomena are, e.g., the anisotropic magnetoresistance (AMR) and the domain wall magnetoresistance (DWMR). The AMR is caused by an anisotropic scattering of electrons and depends strongly on the orientation of the magnetization related to the current direction. The physical origin of the AMR is the spin orbit interaction.[13] Actually, magnetoresistance measurements have been found to be well qualified to investigate the magnetization reversal processes in nanostructures,[14, 15] since the AMR is sensitive to the magnetization distribution during the reversal process. The AMR of bulk polycrystalline samples is proportional to $cos^2\omega$, where ω is the angle between the current (which is parallel to the wire axis) and the magnetization $M(H)$ (which in turn, is a function of the applied field H). However, in the case of magnetic nanostructures, deviations may be expected, due to diffusive scattering at the surface.[16] Neglecting such finite size effects, the magnetoresistive curve $R(H)$ is related to the magnetization $M(H)$ by,

$$R(H) - Ro + (\Delta R)_{max}\left(\frac{M(H)}{M_{sat}}\right)^2, \tag{5.3}$$

when the magnetization is uniform and measured along the wire axis (and hence $M(H)= Ms \cos[\omega (H)]$, where M_{sat} is the saturation magnetization).

Figure 5.6 shows the room temperature magnetoresistance curves for the $Co_{50}Ni_{50}$ nanowire arrays (D ~35 nm, L~ 2.5µm, D_{int}~ 105 nm), where the maximum parallel and perpendicular magnetoresistance, MR, ratio for the nanowires was measured, in parallel and perpendicular configurations. The parallel and perpendicular MR ratios are defined as,

$$(\Delta R/R)^{//} = \frac{R^{//}(H) - R^{//}(max)}{R^{//}H_0} x\ 100, \tag{5.5}$$

$$(\Delta R/R)^{\perp} = \frac{R^{\perp}(H) - R^{\perp}(H_{max})}{R^{\perp}H_0} x\ 100, \tag{5.6}$$

where $R^{//}(H)$ is the resistance for the parallel applied field geometry, $R^{\perp}(H)$ is the resistance of the perpendicular applied field geometry and H_{max} was 756 kA/m. The angular dependence of the applied field has a ~ $cos^2\ \omega$ relationship with the angle, shown in Fig. 5.7, which is typical for an AMR system. Moreover, the observed bell-shape curve for the perpendicular geometry confirms the magnetization reversal mainly by spins rotation.[17] For a magnetic field applied parallel to the nanowire a MR ratio of ~0.5% was obtained, while in the perpendicular geometry a MR ratio of ~1.5% was observed. On the other hand, for Ni and Co nanowires previously reported MR values were around 1.0% at room temperature.[17] In addition, a transverse MR ration of ~ 2% at room temperature in a single and isolated Ni-rich CoNi nanowire has been observed.[18]

Hence, the results reported here are in agreement with the enhanced *MR* of ~1.5% that was observed for $Co_{50}Ni_{50}$.

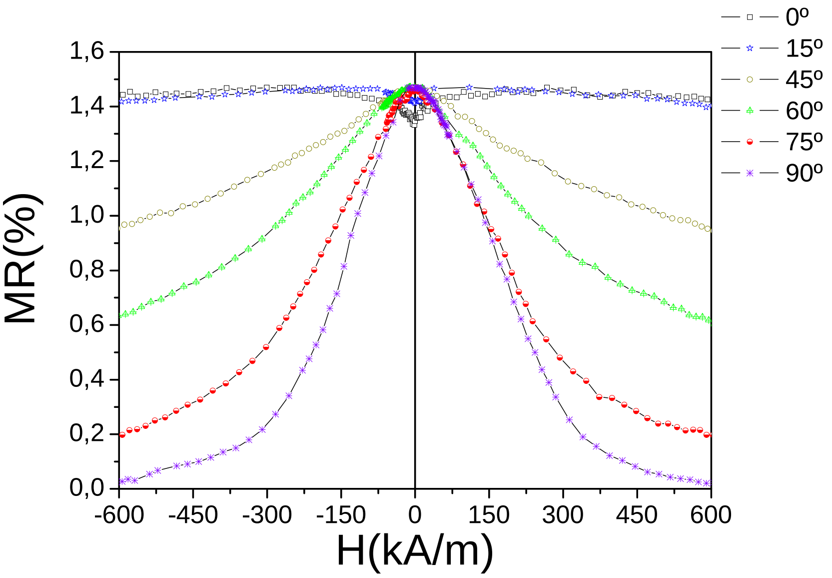

Fig. 5.6 Angular and field dependence of the resistance of $Co_{50}Ni_{50}$ nanowire array.

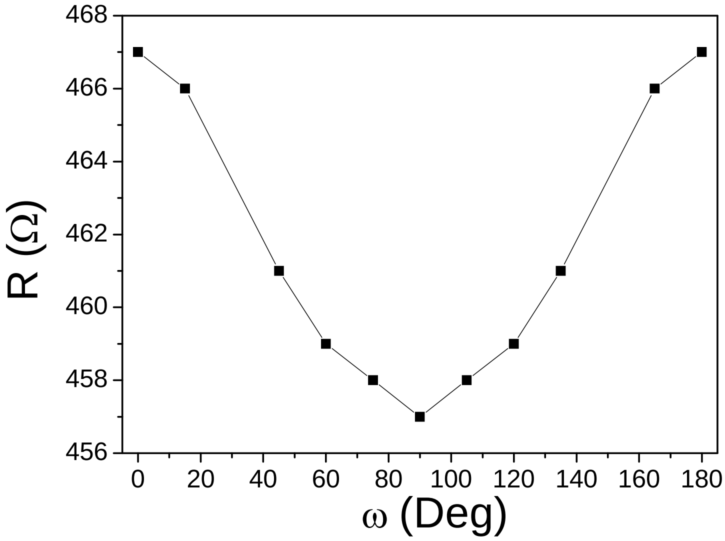

Fig. 5.7 Angular dependence of magnetoresistance of $Co_{50}Ni_{50}$ nanowire array at saturation.

Figure 5.8(a) shows the electrical resistance measurements as a function of temperature, *R (T)*. The total resistivity of a magnetic nanowire can be given by the Matthiessen's rule with distinct contributions,[19]

$$\rho\ (T) = \rho_0 + \rho_{ph}\ (T) + \rho_{mag}\ (T)\ , \tag{5.4}$$

where, ρ_0 is the temperature independent residual resistivity, $\rho_{ph}(T)$ the temperature dependent scattering of conduction electrons by lattice phonons and $\rho_{mag}(T)$ which represents the contribution from magnetic-disorder scattering. A metallic-like *R(T)* behavior ($dR=dT > 0$) was observed over the entire temperature range considered.[10] This indicates that the thin (~3nm) alumina-barrier layer between the dendritic-ends and the Al foil does not affect considerably the transport measurements. In fact, such barriers may even be absent and the dendrites end directly in the Al foil (bottom electrode), or the barrier may be too thin giving a low resistance contribution to the total *R(T)*. This assumption that the electrical conduction is not dominated by the alumina barrier but instead by the nanowire itself (a small contribution from the Au dendrites is also expected) is reinforce by the detection of a change in *R(T)* with applied magnetic field, as it can be seen in Fig.5.8(b), where the maximum parallel and perpendicular *MR* ratio for the nanowires was measured at different temperatures.

For both the parallel and perpendicular orientations, the maximum value of the *MR* ratio occurs at 20 K and decreases linearly with increasing temperature. From figures 5.8 (c) and (d), it can be seen that the *MR* profiles are composed of two magnetization processes. One is the reversible rotation of the magnetization, which is the continuous variation in resistance at high magnetic field. The other is the magnetization reversal, which shows up as discontinuous jumps in the resistance at specific magnetic fields. The jumps in the AMR curves indicate the pinning and de-pinning of the magnetization.[20]

As it was expected, the overall profile has the characteristic AMR, which show negative parallel and positive perpendicular *MR* curves, regardless of temperature [see Figures 5.8(c)-(d)]. The $MR^{\perp}$ ratio was of about 1.7% at 300 K. This slight difference with the value obtained previously in the angular $MR^{\perp}$ curve (see Fig.5.6), may be attributed to fluctuations in temperature during the measurement at room temperature.
The AMR ratio for bulk CoNi alloys was reported to be 6.5% and decreases linearly to 3% at 400K. Although the magnitudes of these ratios are different for the case of the nanowires discussed here, the result coincides with that the ratio decreases continuously with increasing temperature.[21]

Note that discontinuities in the *MR* [perpendicular and parallel in figures 5.6, 5.8(c)-(d) and] are expected to coincide with the switching field. In this work, it should be mentioned that several nanowires electrically connected in parallel have been characterized. Moreover, the actual number of nanowires being measured is unknown, and each single nanowire in the array will possess a slightly distinct resistance and *MR* ratio. Therefore, there is only an access to an average *MR* value, and no discontinuities in the respective curves are distinguishable.

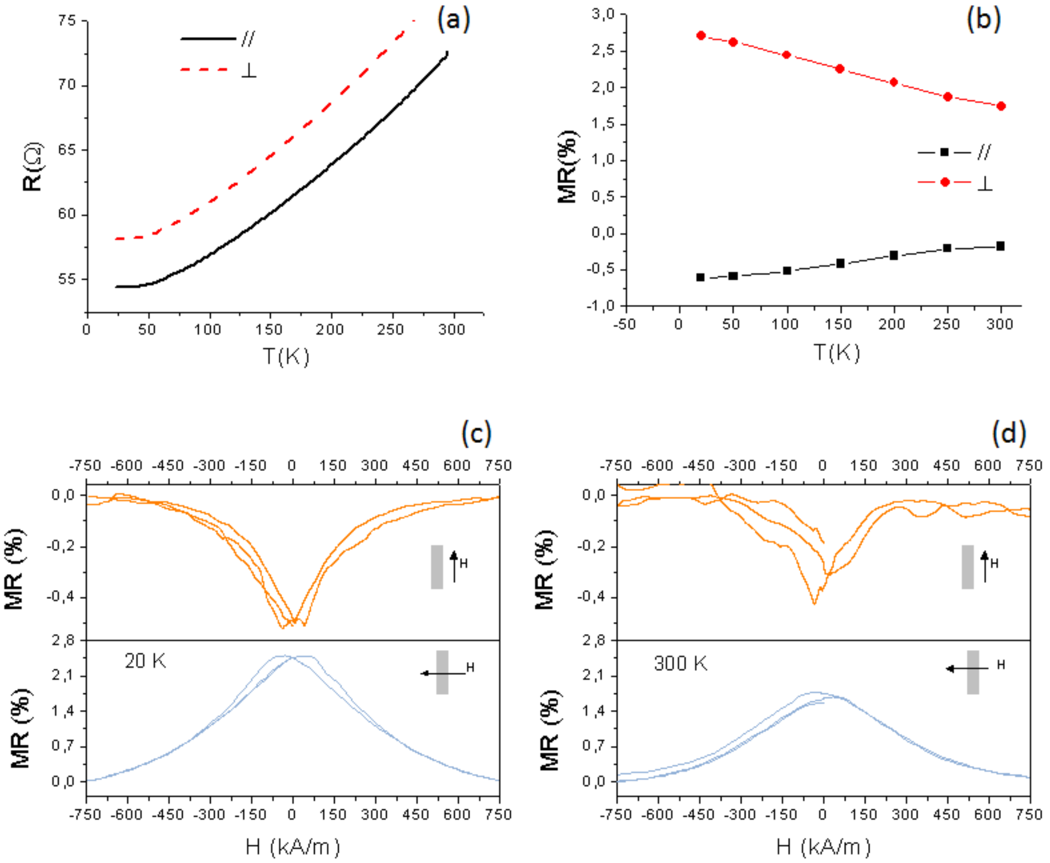

Fig. 5.8. (a) Resistivity as a function of temperature for CoNi nanowires. (b) Temperature dependence of maximum parallel and perpendicular *MR* ratio. (c) *MR* curves at 20 K and (d) 300 K.

5.3.3. Accessing a single nanowire

In this sub-section it is describe the experimental method for positioning four electrical contacts on top of an isolated nanowire by a direct writing/deposition method. These measurements, were performed in collaboration with Prof. J. M. de Teresa, from the Instituto de Ciencia de Materiales de Aragón in Zaragoza, Spain.

The preparation of the samples was performed using commercial Nova 200 NanoLab Dual Beam equipment (FEI), which incorporates different tools, such as SEM, in-situ growth of different materials, focused ion beam etching, and in-situ electrical measurements. The local deposition for the electrical contacts was done by using focus-electron-beam-induced deposition (FEBID), consisting of one-step maskless processes with resolution < 50 nm. Briefly, an automatic gas injection system (GIS) introduces a gas, containing the metal to be deposited, into the chamber. A focused ion beam (FIB) is then scanned over the place where one wants to define the film, and the gas is absorbed by the surface. The dissociation of the gas molecules is induced by the incident ions and the nonvolatile fragment of the molecule from the precursor gas remains on the substrate.[22] The equipment also includes in-situ electrical resistance characterization using four commercial Kleindiek microprobes, connected to a combines 6220 DC current source-2182A nanovoltmeter Keithley system.[23]

CoNi nanowires ($D \sim 50$ nm, $L \sim 10$ μm) were removed from the template by dissolving the latter in a $CrO_3 : H_3PO_4 : H_2O$ solution. The resulting solution was then cleaned several times in deionized water assisted by ultrasound, and in-between subjected to magnetic separation. Afterwards, one small drop of the suspension containing the nanowires was placed over a Si/SiO2 substrate with Ti pads ($t = 180$ nm) defined a priori by optical lithography. The sample was then placed in the system described in the above. An isolated nanowire was selected, and four in-line electrical contacts defined. First, and to guarantee the good quality of the contacted area, FIB etching was performed over the nanowire. Subsequently, Pt contacts were deposited by FEBID over the nanowire [Fig. 5.9], until reaching the main tracks [Fig. 5.9(a)]. The deposited contacts had a width of ~ 400 nm and thickness of ~500 nm.

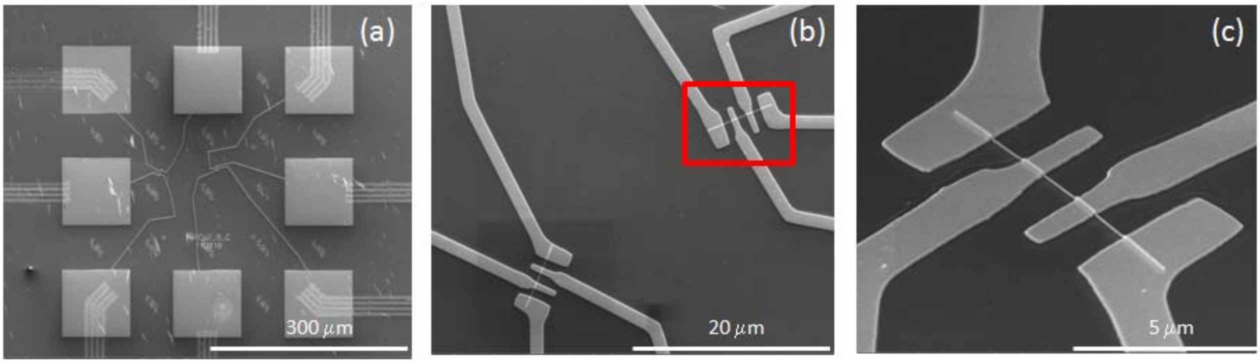

Fig. 5.9. SEM images of Pt contacts deposition by FEBID in a 4 in-line geometry. (a) Nanowires solution dispersed on top of a patterned Si/SiO2 substrate with the lithographed Ti pads; (b) the placing electrical contacts in two single and isolated CoNi nanowires. (c) Zoom of the inset in (b).

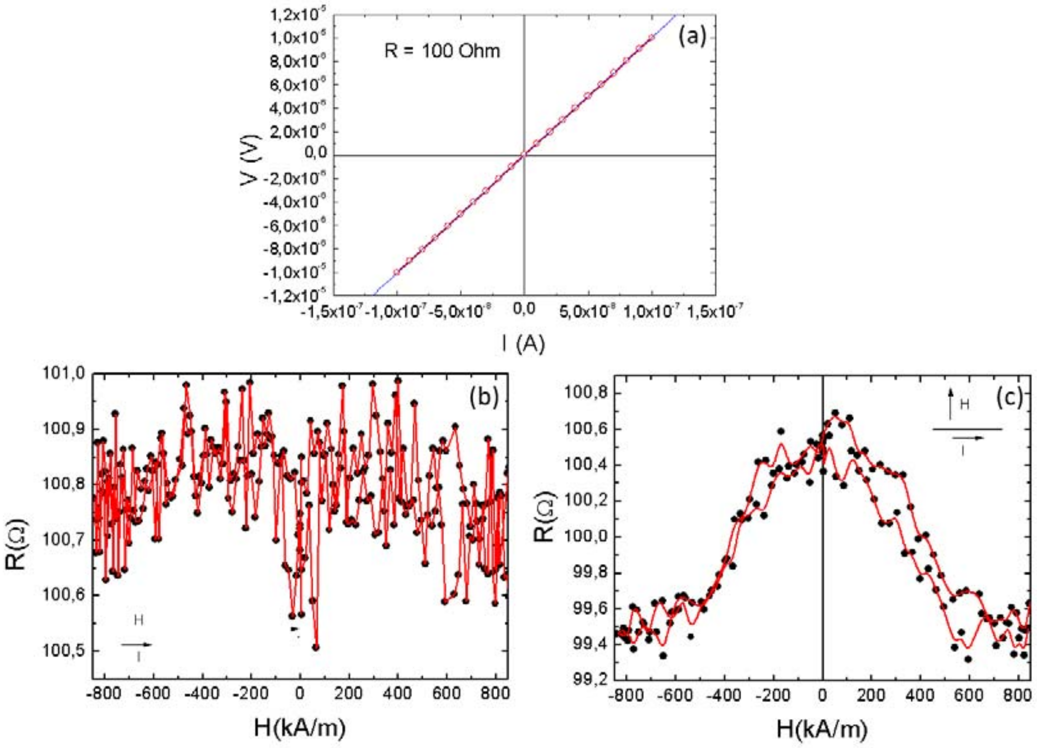

Fig. 5.10. Room temperature (a) *V(I)* curve, and the *R(H)* curves measured with at an applied field parallel (b) and perpendicular (c) to the current applied along the wire axis.

Figure 5.10 shows *V(I)* behavior of the single CoNi nanowire showing a classic Ohmic behavior where the voltage increases linearly with the current resulting in a resistance of 100 Ω. The magnetoresistance of the individual nanowires, shown in Figure 5.10a and 5.10b, is typical of an anisotropic magnetoresistive system, clearly indicating that the magnetic easy axis lays parallel to the wire axis. Interestingly, the transport behavior of a single nanowire, is remarkably similar to that of the array of parallel nanowires hexagonally ordered within the porous alumina matrix, shown in figures 5.6 and 5.8(c-d).

5.4. Summary

In summary, the temperature dependence of magnetic properties of Co, CoPd and CoNi nanowire arrays has been investigated. The effective magnetic anisotropy is determined by the balance between several energy terms, particularly magnetocrystalline (i.e., *hcp* and *fcc* phases) and shape (i.e., aspect ratio of wires) anisotropies. It is conclude that longitudinal anisotropy can be tuned by adequate choice of length in Co wires or by adding suitable elements to their composition. Short Co nanowires and low Pd-content CoPd nanowires exhibit maximum longitudinal anisotropy and coercivity. Ni content enhances modestly the development of a longitudinal anisotropy. Compensation temperature is observed in some cases as a consequence of the different temperature dependence of shape and *hcp* crystalline anisotropies. These findings allow one for the fine tuning (in terms of length and composition) of the magnetic behavior of Co-based magnetic nanowires with longitudinal anisotropy to fulfill the requirements of technological applications.

By filling the dendritic channels with a non-magnetic metallic element, it was possible to access the magnetotransport properties of CoNi nanowires, without resorting to more complicated AAO templates handling procedures. Both, arrays and isolated CoNi nanowires showed the expected anisotropic magnetoresistance behavior, and the dependency of magnetoresistance with temperature in the arrays was consistent with the observed in CoNi bulk samples.

5.5. References

[1] E. L. Silva, W. C. Nunes, M. Knobel, J. C. Denardin, D. Zanchet, K. Pirota, D. Navas, and M. Vázquez, Physica B **384**, 22 (2006).

[2] A. Kumar, S. Fähler, H. Schlörb, K. Leistner, and L. Schultz, Phys. Rev. B **73**, 066421 (2006).

[3] K. R. Pirota, E. L. Silva, D. Zanchet, D. Navas, M. Vázquez, M. Hernández-Vélez, and M. Knobel, Phys. Rev. B **76**, 233410 (2007).

[4] M. Venkata Kamalakar, A. K. Raychaudhuri, Xueyong Wei, Jason Teng, and Philip D. Prewett, Appl. Phys. Lett., **95**, 013112 (2009).

[5] D. C. Leitao, J. Ventura, C. T. Sousa, A. M. Pereira, J. B. Sousa, M. Vázquez, and J. P. Araujo, Phys. Rev. B **84**, 014410 (2011).

[6] M. Vazquez, and L. G.Vivas, Phys. Status Solidi B **248**, 2368 (2011).

[7] L. G. Vivas, M. Vázquez, V. Vega, J. García, W.O. Rosa, R. P. del Real and V. M. Prida, J. Appl. Phys.,**111**, 07A325 (2012).

[8] C Tannous and J Gieraltowski, Eur. J. Phys. **29**, 475 (2008).

[9] K. R. Pirota, F. Beron, D. Zanchet, T. C. R. Rocha, D. Navas, J. Torrejon, M. Vázquez, and M. Knobel, J. Appl. Phys. 109, 083919 (2011).

[10] Diana Cristina Pinto Leitão, *Micro and Nano Patterned Magnetic Structures*, PhD thesis, Universidade do Porto, 2010.

[11] D. Atkinson, A. Allwood, G. Xiong, M. D. Cooke, C. C. Faulkner, and R. P. Cowburn, Nature Mater. **2**, 85 (2003).

[12] S. S. P. Parkin, Phys. Rev. Lett. **71**, 1641 (1993).

[13] R. McGuire and R. I. Potter, IEEE Trans. Magn. **11**, 1018 (1975).

[14] S. J. Blundell, C. Shearwood, M. Gester, M. J. Baird, J. A. C. Bland, and H. Ahmed, J. Magn. Magn. Mater. **153**, L17 (1994).

[15] C. Shearwood, S. J. Blundell, M. J. Baird, J. A. C. Bland, M. Gester, and H. Ahmed, J. Appl. Phys. **75**, 5249 (1994).

[16] Th. G. S. M. Rijks, R. Coehoorn, M. J. M. de Jong, and W. J. M. de Jonge, Phys. Rev. B **51**, 283 (1995).

[17] L. Fashen and et al., J. Phys.: Cond. Matt. 16, 8053 (2004).

[18] Y. Rheem, B-Y. Yoo, W.P. Beyermann and N. V. Myung, Nanotechnology, **18**, 125204 (2007).

[19] M. Venkata Kamalakar and A. K. Raychaudhuri, Phys. Rev. B **79**, 205417 (2009).

[20] S. Pignard, G. Goglio, A. Radulescu, L. Piraux, S. Dubois , A. Declemy and J. L. Duvail, J. Appl. Phys., **87**, 824 (2000).

[21] R. M. Bozorth, *Ferromagnetism,* New Jersey: Wiley (1951).

[22] A. Fernandez-Pacheco, J. M. De Teresa, R. Cordoba, M. R. Ibarra, D. Petit, D. E. Read, L. O'Brien, E. R. Lewis, H. T. Zeng, and R. P. Cowburn, Appl. Phys. Lett., vol. 94, no. 19, pp. 192509–3, 2009.

[23] A. Fernandez-Pacheco, J. M. De Teresa, R. Cordoba, and M. R. Ibarra, Phys. Rev. B, **79**, 174204 (2009).

Chapter 6: Micromagnetic Modeling of Magnetization Reversal in Magnetic Nanowires

6.1. Introduction

Micromagnetic modeling of nanostructured ferromagnetic materials has been an active area of research in the past decade, and is receiving even more attention because of the general interest in nanoscale physics. It can supply information, complementary to experimental, about the magnetization reversal modes in nanostructures. In particular, as a result from progress in the fabrication of highly ordered arrays of magnetic nanowires and their prospective application in different technological areas, the micromagnetic properties of magnetic nanowires, and especially the understanding of their hysteretic behavior, recently has become of growing interest.[1,2] The characteristic parameters of the hysteresis loop of arrays of nanowires, i.e. the coercive field and the remanence as well as the shape of the hysteresis loop, depend on the particle shape, the parameters of the magnetic material, the microstructure and on the magnetostatic interaction with the neighboring wires. To understand the magnetization reversal mechanism, numerical methods are performed in this chapter to treat isolated wires and an array of interacting wires in the framework of micromagnetism.

In this chapter, first the micromagnetic reversal of individual Co nanowires with different crystalline structures is considered. The effect of changing length (aspect ratio) and the dominant crystal phase are considered to model the resulting coercivity mechanism. After this, magnetic interactions in hexagonal arrays of nanowires are included to improve the comparison with experimental data. Then, a multilayer nanowire with *hcp* and *fcc* layered structure is discussed. Finally, the cases of Co nanopillars are studied as a function of the pore diameter and the crystallographic structure in order to compare with experimental results.

6.2. Micromagnetic background

Equilibrium configurations of the magnetization correspond to local minima of the Gibbs free energy. Therefore, it is possible to calculate magnetic configurations by minimizing the free energy as a function of the continuum magnetization $\boldsymbol{M}$. The relevant magnetic energy contributions are the exchange energy E_{ex}, the magnetocrystalline anisotropy energy E_{an}, the magnetostatic energy E_D and the Zeeman energy E_Z in an external field. The detailed magnetic behavior of a given material depends on the detailed balance between these energy terms. Essentially, it is assumed that the magnetization is a continuous vector field $\mathbf{M}(\mathbf{r})$, with $\mathbf{r}$ the position vector, thus,

$$\mathbf{M}(\mathbf{r}) = M_s\mathbf{m}(\mathbf{r});\ \mathbf{m}\cdot\mathbf{m} = 1, \tag{6.1}$$

where M_s is the saturation magnetization of the material. The basic micromagnetic approach is to formulate the energy in terms of the continuous magnetization vector field and to minimize this energy in order to determine static magnetization structures. The energy terms for the sample of volume V are formulated as follows:

$$E_{tot} = E_{ex} + E_{an} + E_H + E_D, \tag{6.2}$$

$$E_{ex} = \int_V A(\mathbf{r})[(\nabla m_x)^2 + (\nabla m_y)^2 + (\nabla m_z)^2]\,dV, \tag{6.3}$$

with A the micromagnetic exchange parameter,

$$E_{an} = -\int_V K_{an}(\mathbf{r})[\mathbf{m}(\mathbf{r})\mathbf{e}(\mathbf{r})]^2\,dV, \tag{6.4}$$

where K is the macroscopic anisotropy parameter and $\mathbf{e}$ is the unitary vector of the easy axis;

$$E_D = -\int_V (\mathbf{M}(\mathbf{r})\mathbf{H}_D(\mathbf{r}))\,dV, \tag{6.5}$$

where $\mathbf{H}_D$ is the demagnetization field, and,

$$E_Z = \int_V (\mathbf{M}(\mathbf{r})\mathbf{H}_{ext}(\mathbf{r}))\,dV, \tag{6.6}$$

where $\mathbf{H}_{ext}$ is the external applied field.

For a given ferromagnetic material, the total energy is given by the magnetization field within the sample. Numerically, both magnetization and this field are represented in a discretized form. The geometry of nanowires is suitable for the finite elements discretization. Therefore, the sample is subdivided into finite elements of irregular tetrahedral shape. The magnetization is calculated at the nodes of the finite element mesh. Since the magnitude of the magnetization vector is constant, two polar angles (ϑ_i, φ_i, the angles enclosed with the z-axis and with the x-axis in the xy-plane, respectively) are sufficient to describe the direction of the magnetization at each node i: The total energy can then be minimized with respect to the variables (ϑ_i, φ_i). Details on this procedure are described elsewhere.[3] In the Magpar package[4] used in the present study the demagnetizing field is calculated considering a magnetic scalar potential U, which is assigned to each node of the mesh and from which the demagnetizing field $\boldsymbol{H}_d = -\nabla U$ is derived. The magnetic scalar potential is calculated by means of a hybrid boundary element/finite element method.[5] This procedure consists essentially of splitting the potential U in two parts $U = U_1 + U_2$, of which U_1 satisfies Poisson's equation inside the ferromagnetic body $\Delta U_1 = 4\pi \nabla \boldsymbol{M}$ and U_2 is the solution of Laplace's equation $\Delta U_2 = 0$ with appropriate boundary conditions. The boundary element method is employed to determine the Dirichlet boundary conditions for U_2 [6] at the sample surface:

$$\frac{\partial U_1}{\partial n} - \frac{\partial U_2}{\partial n} = 4\pi \boldsymbol{M} \cdot \boldsymbol{n},$$

(6.7)

where **n** is the vector normal to the surface.

6.3. Modeling of magnetization reversal

In order to study the reversal process of a single wire, time-resolved micromagnetic modeling is required. The temporal evolution of the magnetization ***M*** is given by Gilbert's equation, [5]

$$\frac{d}{dt}\boldsymbol{M} = -\gamma\left(\boldsymbol{M} \times \boldsymbol{H}_{eff}\right) + \frac{\alpha}{M_s}\left(\boldsymbol{M} \times \frac{d\boldsymbol{M}}{dt}\right), \qquad (6.8)$$

where γ is the gyromagnetic ratio and α is a damping constant. The effective field $\boldsymbol{H}_{eff}$ follows from the energy density e as the negative variational derivative with respect to the magnetization $\boldsymbol{H}_{eff} = \delta E/\delta \mathbf{M}$. For the purpose of energy minimization large damping constant is used.

6.4. Individual Co nanowires with *hcp* and *fcc* structure phases

In the present study, we have considered the demagnetization process of isolated Co nanowires, as well as ordered with hexagonal symmetry. The hanowires have particular magnetocrystalline anisotropy correlated to their crystalline structure (*fcc* and *hcp* phases) In order to compare the simulations with the experimental results obtained in Chapter 3 the crystalline structure was also correlated to their geometry dimensions. Simulations have been performed using the Magpar package[4] with finite element discretization and using the typical magnetic parameters of bulk Co for both *hcp* and *fcc* crystal phases[7,8] (see Table 6.1). An important feature of the finite element method is that it allows for good geometrical approximations of particles with curved boundaries, such as the cylindrical nanowires[9] (see the mesh in Fig 6.1.). The external field was applied in direction of the wires' axis. Hysteresis loops were simulated for values of the external fields between +400 and -400 kA/m: the field was reduced and incremented in steps of 4kA/m.

Table 6.1. Magnetic parameters for Co, with $J_s = \mu_o M_s$, where μ_o is the permeability of vacuum; A the exchange stiffness constant and K_1, the magnetocrystalline anisotropy constant.

	J (T)	A (J/m)	K_1 (J/m^3)
hcp Co	1.76	1.3e-11	4.5e5
fcc Co	1.76	1.3e-11	6.75e4

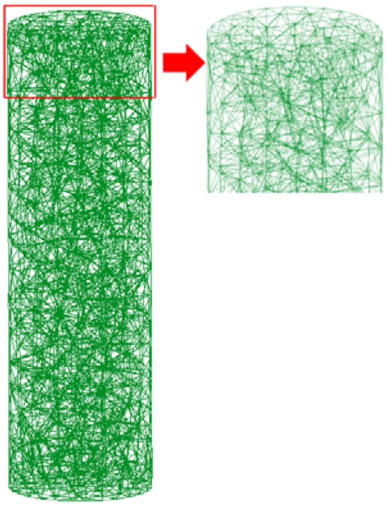

Fig. 6.1. Isolated nanowire illustrating the finite element discretization (left) and enlarged view on the top of the wire (right).

For comparison with the experimental results obtained in section 3.4, the modeled wires in this section are 35 nm in diameter and have lengths from 120 to 1000 nm. It is known that the shape anisotropy resulting from the magnetostatic energy and nanowire geometry increases as a function of the nanowire length. To estimate the shape anisotropy first nanowires without internal anisotropy were simulated [see Fig. 6.2]. The resulting strength of the shape anisotropy was estimated in 7e4 J/m^3 and 1e5 J/m^3 for 120 nm and 1000 nm of length, respectively. It must be noted that from the point of view of the effective anisotropy, for Co (111) *fcc* phase, the magnetocrystalline anisotropy energy is smaller than the shape anisotropy energy density, whereas for a Co *hcp* structure, it is larger. Hence, it can be expected a more pronounced interplay of both magnetocrystalline and shape anisotropies for the *hcp* case.

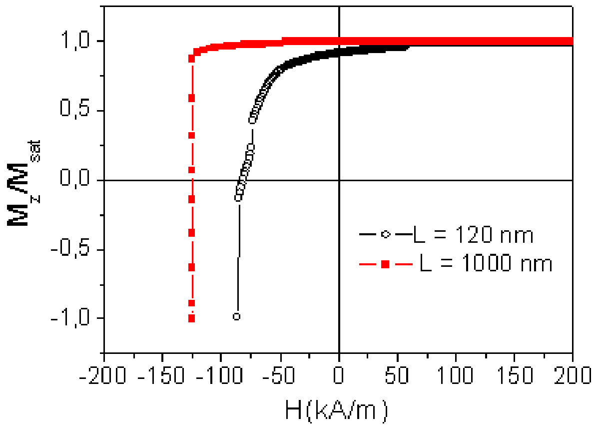

Fig. 6.2. Simulated parallel descending *M(H)* curves for an isolated nanowire without internal anisotropy for $L = 120$ nm and 1000 nm.

In the case of simulated nanowires with *fcc* phase, the remanent state is almost saturated (see Fig. 6.3, right) and two open vortex-like states at the opposite ends are formed. As is generally reported for nanowires,[10] the demagnetization process takes place in a single quasi-curling step, originating a nearly square loop with single large Barkhausen jump (see Fig. 6.3, left). The resulting coercivity increases as a function of the nanowire length in agreement with the general behavior of the shape anisotropy (see Fig. 6.4). Note that in real nanowires the two ends are not equivalent due to the presence of defects and thus we cannot expect a symmetric propagation of the two vortices starting simultaneously from both ends.

In the case of nanowires with *hcp* phase with easy axis perpendicular to its long side, the magnetosrystalline anisotropy competes with the shape anisotropy. The nucleation process also starts with the creation of vortices at the two ends with the same or opposite chiralities. The remanence is characterized by the nucleus magnetized along the nanowire length and a circularly magnetized shell (see Fig. 6.5, right panel). The subsequent demagnetization occurs through the nucleation of a domain wall-like structure in the centre of the nanowire that propagates towards both ends. The coercive field again increases as a function of the nanowire length (see Fig. 6.6).

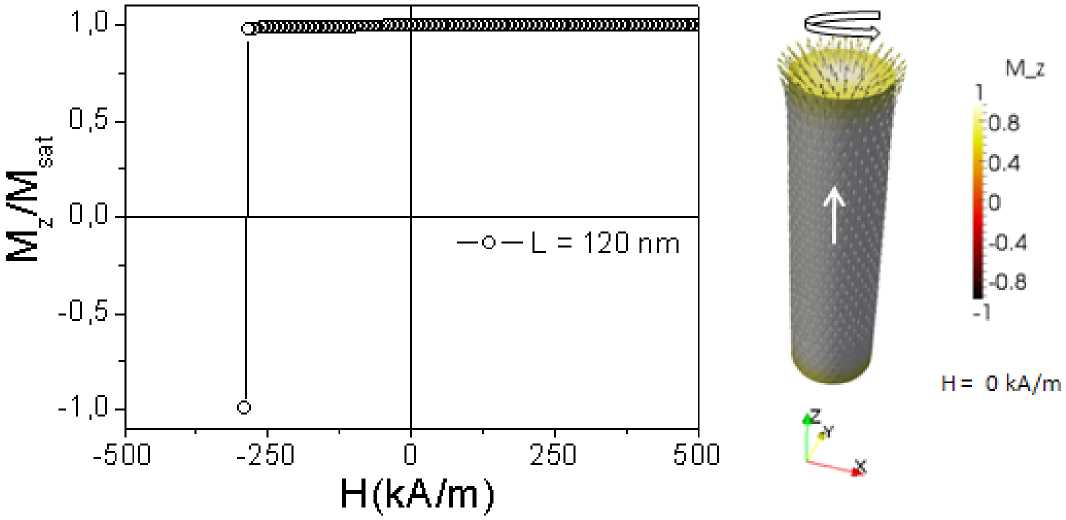

Fig. 6.3. The left panel shows the simulated parallel descending hysteresis branch for a isolated nanowire with *fcc* crystal phase and *L* of 120 nm. The right panel contains the image of the magnetization distribution at the remanence state. The arrows schematically indicate the magnetization direction and the colors indicate the longitudinal magnetization, M_z, value.

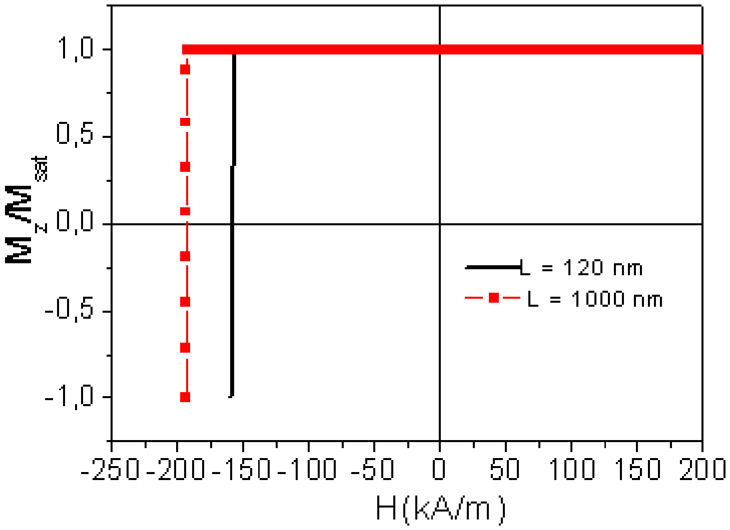

Fig. 6.4. Simulated parallel descending *M(H)* curves for a isolated nanowire with *fcc* crystal phase for *L* = 120 nm and 1000 nm.

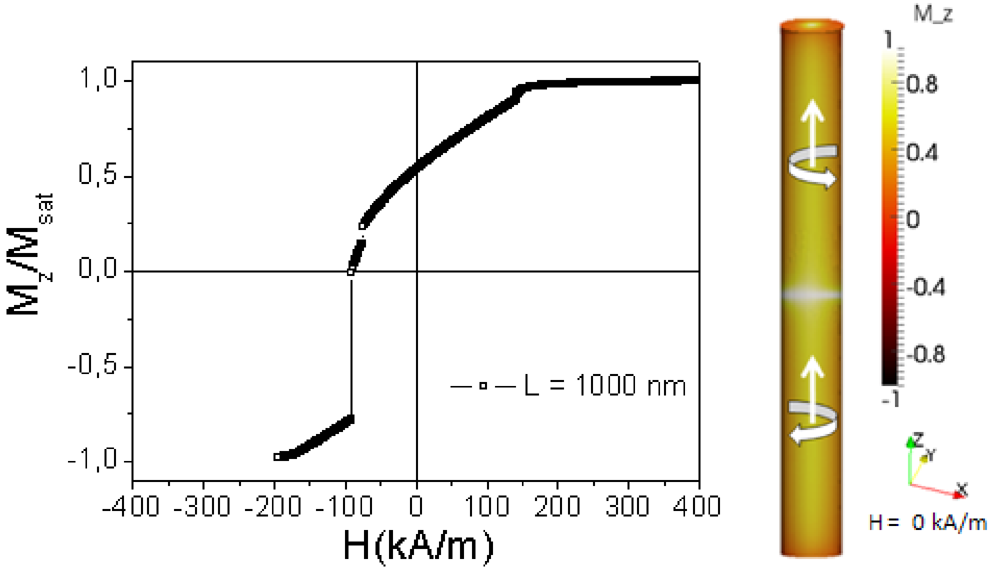

Fig. 6.5. The left panel shows the simulated parallel descending hysteresis branch for a isolated nanowire with *hcp* crystal phase and *L* of 1000 nm. The right panel represents the image of the magnetization distribution at the remanence state. The arrows schematically indicate the magnetization direction and the colors indicate the longitudinal magnetization, M_z, value.

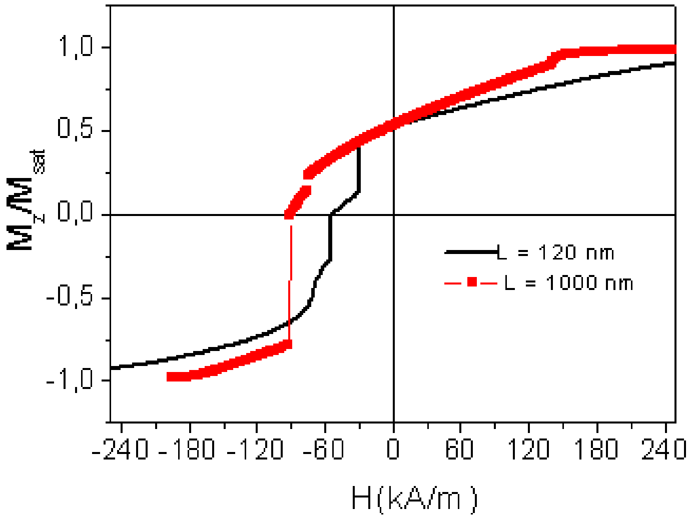

Fig. 6.6. Simulated parallel descending *M(H)* curves for a isolated nanowire with *hcp* crystal phase for *L* = 120 nm and 1000 nm.

6.5. Modeling of arrays of nanopillars and nanowires

To investigate the effect of the magnetostatic interaction between the wires, simulations of the hysteresis loops were performed for a hexagonal array of seven nanowires, with an interpore distance of 105 nm, as it is usual for nanowires inside in a nanoporous membrane anodized in oxalic acid. It has been shown that increase in the number of simulated wires results in a decrease in the coercive field of only less than 10%.[8,9]

Modeling of nanowires assuming a *fcc* structure results in loops with strong effective longitudinal anisotropy. However, a noticeable reduction in coercivity is calculated when considering the interactions among nanowires. The demagnetization takes place via a single quasi-curling process as for an isolated wire, but in this case, the nanowire in the center of the hexagonal arrangemet is the first which switches while the surrounding wires are still magnetized and after that, these nanowires also switch their magnetization in random sequence, as it is represented in Fig. 6.7 (a) and also is seen in the multiple jumps of the corresponding hysteresis cycles [see Fig. 6.7(c)].

In the case of nanowires considering *hcp* crystalline phase with *c*-axis oriented perpendicular to the long nanowire direction, the modification of the coercivity due to interactions is relatively moderated. The reversal process is similar to the one for a single wire: it initiates at the ends of the wire at the high field region. At remanence, the domain structure is characterized by an intermediate state in which the nanowire´s core is magnetized along its axis and is surrounded by a circularly magnetized shell. The nanowires switch randomly. The corresponding remanence is, therefore, smaller than for *fcc* nanowires. The coercivity is determined by the propagation of complex domain walls [Fig.6.7 (b)]. The descending hysteresis branches for arrays of nanowires with both *fcc* and *hcp* crystal phase are presented in Fig. 6.7 (c). In Fig. 6.7(d) the coercivity values obtained from the experiments and the simulations are presented. Both the *fcc* and *hcp* curves for the modeled individual nanowires follow a similar trend but the second one with reduced values, as is expected from the strong perpendicular anisotropy effect. When magnetostatic interactions among nanowires are considered, the coercivity decreases considerably.

6.5.1. Comparison with experimental results

As expected for increased shape anisotropy, and similarly to previously reported results,[10,11] the simulations show that for each case, increasing the aspect ratio, $R = L/D$, results in an increase in the longitudinal shape anisotropy and the coercive field. However, the experimental behavior of the coercivity, H_c, and the remanence, M_r, with L, is just the opposite, namely, a reduction in both parameters is observed (see Fig 6.7 d).

The combined crystallinity/geometry effect can be understood by considering that short nanowires are predominantly *fcc* where the shape anisotropy dominates the total effective anisotropy. For longer *hcp*-symmetry Co nanowires, the transverse magnetocrystalline anisotropy easy axis competes with longitudinal shape anisotropy. However, it is not clear from the experimental results if the *fcc* phase is the only one present up to approximately 350 nm.[12] Besides, the calculations for the *hcp* arrays are more in accordance with the experimental data starting from L of 350 nm. For shorter lengths, the H_c values simulated for *fcc* nanowires neither completely fit the experimental ones. Therefore, in order to take into account the combined crystallinity/geometry effect, we have performed simulations for an array where we introduced a granular structure with the percentage of randomly distributed *hcp* grains increasing monotonically with the increase in L [mix curve in Fig. 6.7(d)]. This model provides the coercive field values more in agreement with the experimental ones.

Additional small remaining discrepancy between the experimental and modeled values may be attributed to several possible contributions: (i) a certain contribution from (002) phase which favors the partial parallel alignment of the *c*-axis with the nanowires and thus, the reinforcement of the uniaxial anisotropy; (ii) small angle between (100) texture and perpendicular to the wire direction (iii) small distribution of easy axes within the (100) texture, (iv) presence of defects and fluctuations of wire diameters and lengths;[11] (v) additional dipolar interactions coming from an infinite array. Finally, it must be note that the modeling also shows that the remanence decrease with the nanowire length [see inset in Fig. 6.7(c)] in qualitative agreement with the experiment.

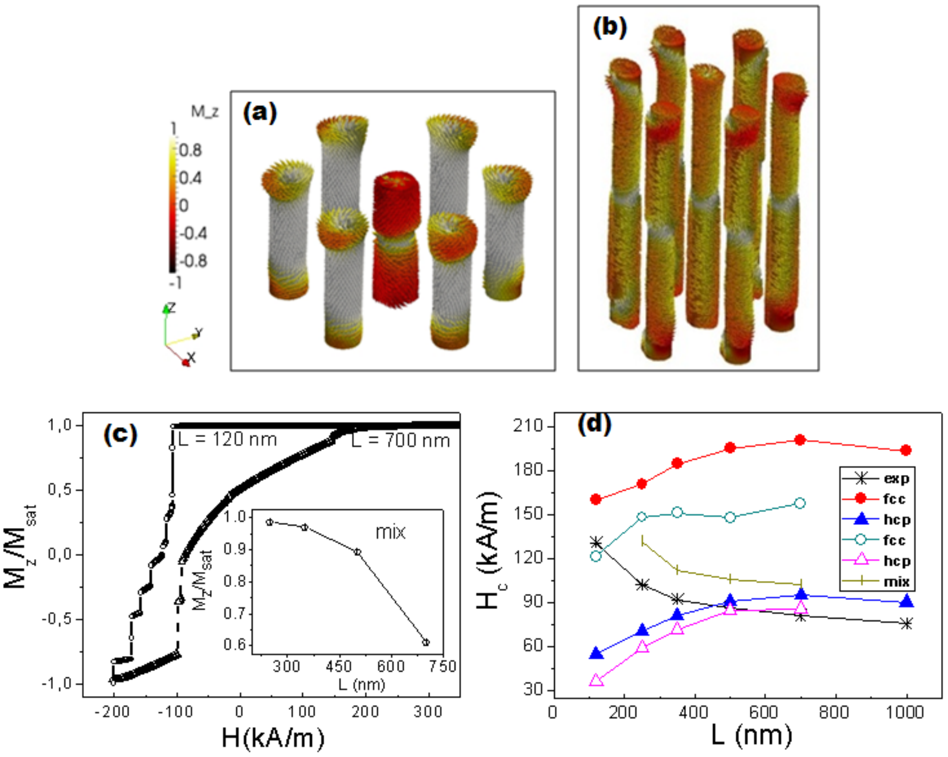

Fig. 6.7. Images of the magnetization distribution at applied field of -80kA/m for nanowires with (a) L=120 nm and (b) L=700 nm. The arrows schematically indicate the magnetization direction and the colors indicate the longitudinal magnetization, M_z, value. (c) Simulated parallel descending hysteresis branches for arrays of seven nanowires. The inset represents the remanence (mix values) as a function of the nanowire length. (d) Parallel coercivity as a function of nanowires length for experimental (exp) and modeled (*fcc* and *hcp*) nanowires. The simulations are made for individual nanowires (full symbols) and hexagonal arrays of seven nanowires (empty symbols). The mix curve represents the values obtained for a different percentage of *hcp* grains (10%, 20%, 50%, and 90% for L=250 nm, 350 nm, 500 nm, and 700 nm, respectively).

6.6. Mixed *fcc/hcp* nanowires

Assuming that Co nanowires present two different possible crystalline structures (*fcc* and *hcp*), [12] it is interesting to study in detail the reversal mechanism of a combined system. When Co nanowires are crystallized in the *hcp* phase, even if the wires can be polycrystalline, the XRD patterns reveal a strong crystal texture, i.e., the relative intensity of one of the *hcp* planes can be significantly larger than the other planes, evidencing a preferred crystallographic orientation along the perpendicular direction to this corresponding plane. In this section, we have performed simulations of the demagnetization process of isolated nanowires with combined crystalline structures of both *fcc* and *hcp* phases, i.e., a modification of the magnetocrystalline anisotropy parameter by segments (a multilayer nanowire, in which each layer can represent a different structure). The understanding of these wires is relevant for the design of hybrid systems, which may be of interest in spintronic and microwaves devices.

From the experimental point of view, it should be remembered what was discussed in Chapter 3: Co nanowire arrays crystalline structure and texture can be tailored by the synthesis process (i.e, pH of the electrolytical bath and plating time). Hence, the sensitivity of the magnetic properties of Co nanowires on electrolytic solution pH opens a route for obtaining the hybrid structures proposed for the simulations in this section. Therefore, using three cobalt solutions of three different pH values, trilayered Co nanowires can, in principle, be fabricated. These nanowires will be constituted of Co layers having different magnetocrystalline structures by segments.

Cobalt trilayer nanowires of D = 40 and L = 1500 nm were modeled using the typical bulk magnetic parameters for Co, as before. For each layer (with a thickness of 500 nm) we considered a specific crystal structure (see the scheme in Fig. 6.8). Four numerical experiments were performed: two of them assuming that the system presents just the *hcp* phase with different orientations in each layer, and the other two, assuming coexistence between the two crystal phases.

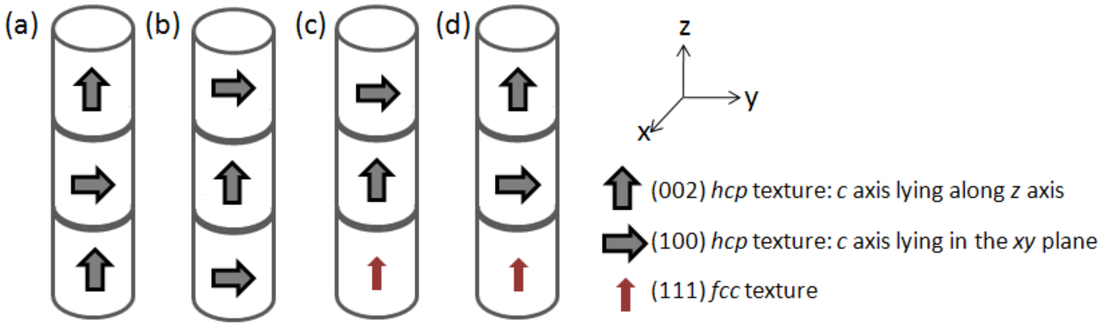

Fig. 6.8. Sketches of trilayer Co nanowires with different crystal structures in each layer. Nanowires in (a) and (b) are textured in the *hcp* phase; (c) and (d) present both *hcp* and *fcc* phases

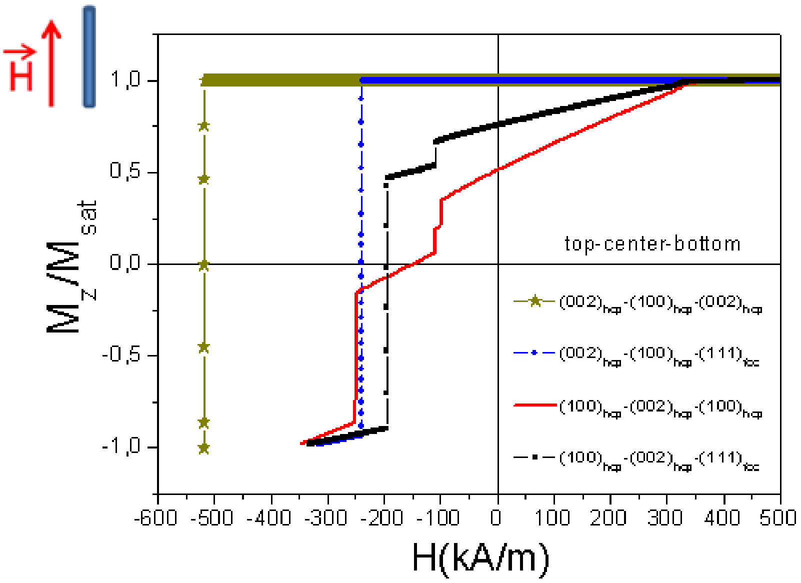

Fig. 6.9. Simulated parallel descending hysteresis branches for four Co trilayer nanowires. Each layer is characterized by a particular Co crystal structure.

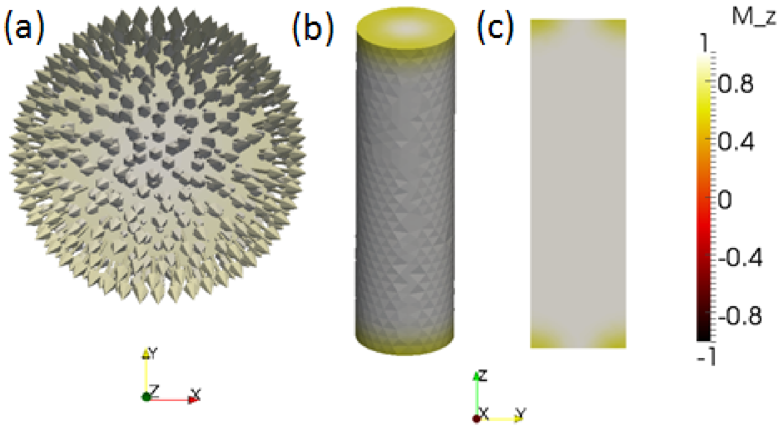

Fig. 6.10. Images of the magnetization distribution for a trilayer Co nanowire [top: (002) *hcp* texture; center: (100) *hcp* texture; bottom: (002) *hcp* texture]. (a) Top view close to the remanence state; the arrows schematically indicate the magnetization direction. (b) Nanowire at remanence and (c) the correspondent slice of the cross section.

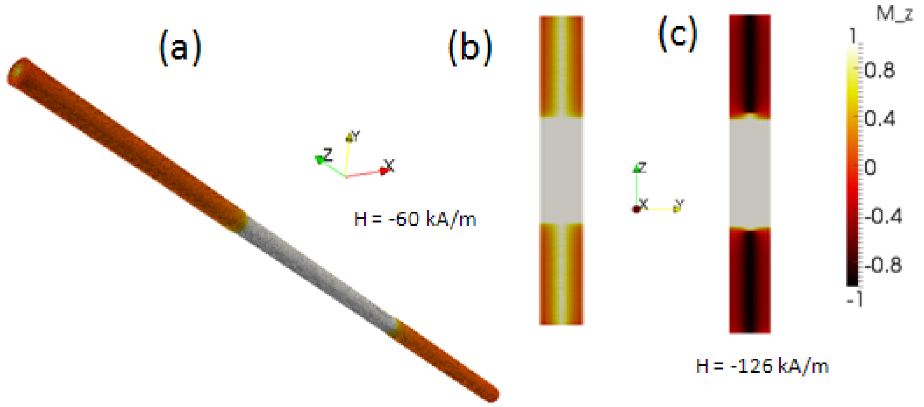

Fig. 6.11. Images of the magnetization distribution for a trilayer Co nanowire [top: (100) *hcp* texture; center: (002) *hcp* texture; bottom: (100) *hcp* texture]. (a) Magnetization configuration in nanowire at H = -60 kA/m, (b) cross section slice at H = -60 kA/m and (c) at H = -126 kA/m.

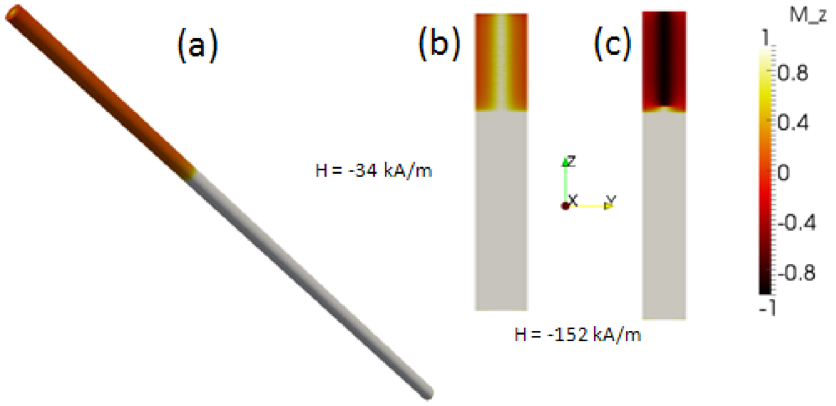

Fig. 6.12. Images of the magnetization distribution for a trilayer Co nanowire [top: (100) *hcp* texture; center: (002) *hcp* texture; bottom: (100) *hcp* texture]. (a) Magnetization configuration in nanowire at H = -34 kA/m, (b) cross section slice at H = -34 kA/m and (c) at H = -152 kA/m.

These segments have been enumerated from top to bottom as 1, 2, and 3, respectively. Due to the large thickness of each segment, segments 1 and 3 don´t interact. So, it is expected just an interaction between segments 1 and 2 and between 2 and 3. Fig. 6.9 shows the descending hysteresis branches for the simulations proposed in this section. For simplicity, we can identify three cases, each of them with a representative characteristic behavior: i) two segments with longitudinal anisotropy separated by another segment with in plane anisotropy [Fig.6.8 (a) and (d)], ii) two segments with in plane anisotropy separated by another segment with longitudinal anisotropy [Fig.6.8 (b)] and, iii) the segment at the top with in plane anisotropy followed by two segments of longitudinal anisotropy [Fig.6.8 (c)].

In the first case (green stars and blue circles in Fig. 6.9), the demagnetization takes place via a single jump, as can be appreciated by the square loops. Around the remanent state, two vortices at the opposite ends are formed (see Fig. 6.10), similar as the simulated *fcc* nanowires in the section above. It may be thought that the segment 2, with in plane anisotropy, is forced by segments 1 and 3 to align their magnetic moments in the *z* direction. However, the coercivity for the nanowire with just *hcp* phase is much higher. Therefore, the role of the middle segment is reduced just to the decrease of the overall effective anisotropy as also happens in soft/hard multilayers layers. Note that the middle segment of the hcp phase can be generally considered as a soft materials since their the magnetocrystalline anisotropy is compensated by the shape anisotropy, while in the segments 1 and 3 they are parallel and thus the overall anisotropy is strong.

On the other hand, the second case (a longitudinal anisotropy segment between two in plane anisotropy segments, red line in Fig.6.9) is characterized by a magnetization curve which presents three kinds of plateaus: the first two correspond to the switching of the segments with in plane anisotropy, top and bottom, respectively; the third plateau correspond to the switching of the segment number 2 (with longitudinal anisotropy) at about -244 kA/m, hence, the remanence is only 0.5. Fig. 6.11 shows images of the magnetization distribution during the reversal process. The domain structure of segments 1 and 3 is characterized by a magnetized core along *z* axis (which inverts first), surrounded by a circularly magnetized shell. The subsequent demagnetization occurs when the segment in the middle of the wire, inverts trough a single jump. This behavior is also consistent with the general theory of soft/hard magnetic trilayers (exchange-spring effect). Indeed in these cases the demagnetization is initiated in the soft layers and is pinned at the soft/hard boundaries. For the subsequent unpinning the applied field increment is necessary.

Finally, we present the discussion of the third case (black squares in Fig.6.9). The *fcc* segment at the bottom and the *hcp* segment with (002) texture, are magnetized as a single segment along the *z* direction, even at an applied field of -180 kA/m. As expected, the first segment with the *hcp* (100) texture reverses its magnetization first, while segments 2 and 3 switch its magnetization at an applied field of -196 kA/m (Fig. 6.12). The remanence is 0.75.

An interesting feature in the last two cases is the possibility of manipulation of the plateau that appears in the hysteresis curves. By varying the length of the magnetic segments the size of the plateau can be varied which may be related to two phenomena (i) the pinning field dependence on the soft phase size (ii) the dipolar interaction between the segments. Dipolar interactions play a significant role in the magnetic behavior of the nanowire array, leading to rich physical phenomena and great application potentials.[14] Besides, in the case of multilayers isolated nanowires, dipolar interactions between segments can be thought as another degree of freedom which can be exploited in order to create additional functions in a complex hybrid system. Also in the trilayer nanowires discussed in this section, it will be interesting to study the reversal mechanism for others applied field angles in order to explore the limits of the different behaviors, that is, the configuration at which the magnetic segments are independent and to establish clearly when it is possible to obtain that one segment reverses after the other. Hence, further studies are needed from the theoretical part, which can be a guide for the future experimental work.

6.7. Modeling of nanopillars as a function of diameter

Through the above sections, the magnetic properties of arrays and isolated nanowires have been investigated with particular emphasis in three questions: (i) factors that determine the effective easy axis of the wires, (ii) magnetization reversal processes within nanowires and (iii) magnetic interaction between wires. The diameter of the magnetic nanowire plays a key role in determining the above three phenomena. The approximate theory of demagnetisation factors basically states that the coercive field is a function of the ratio length/diameter. However, we should note that this approximation is valid for saturated nanowires only. Particularly, the known phase diagrams for nanopilars show that as the ratio length/diameter decreases the vortex state should be stabilized at the remanence.[15]

In this section, the demagnetization process has been studied in Co nanopillars varying their diameter, in order to compare these micromagnetic results with the structural and magnetic properties experimentally measured for Co nanopillars (of similar geometry) in Section 3.5.2. In addition, the influence of magnetostatic interactions have been studied within the model of seven nanopillars arranged with hexagonal symmetry.

6.7.1. Magnetic reversal process for nanopillars without magnetocrystalline anisotropy

Figure 6.13 shows simulated hysteresis curves for both applied field parallel and perpendicular to the main nanopillars axes. In order to study just the effect of increasing the pore diameter in the demagnetization process, the internal anisotropy was set to zero. Besides, the left column in this figure contains the simulations performed for arrays of seven nanopillars, while in the right column the results of the respectively isolated cases are presented. Hence, it is possible to study also the magnetostatic interactions for each specific diameter value. As expected from demagnetized factor approximation, from the comparison of the series of hysteresis curves, it is deduced that the higher diameter results in a decrease in axial coercivity and remanence. That is, the uniaxial anisotropy along the long nanopillar axis decreases, and the shape of the hysteresis curve resembles that of the reorientation of the global axis from out-of-plane towards in-plane configuration (laying in the membrane plane). This reduction of the uniaxial anisotropy is attenuated when the magnetostatic interactions are taken into account. On the other hand, it should be noted that increasing the diameter leads to a crucial difference in the magnetization reversal mechanism, which cannot be described within the demagnetized factor approximation. Fig. 6.14 collects images of the magnetization distribution for isolated nanopillars at specific applied field values, in both parallel and perpendicular configuration, during the demagnetization process. See the hysteresis curves in Fig.13 when it is required in the discussion below.

When *D* is 35 nm, the remanent state of the pillar is characterized by the central part aligned within the direction of the applied field [// field configuration in Fig.6.14(a)]. However, at both ends of the pillar a vortex-like state is created with cores pointing along the applied field and in this particular case with clock-wise chirality. At field values of -73 and -74 kA/m a jump in the hysteresis is observed indicating an irreversible change, corresponding to the rotation of the magnetization at the shell of the nanopillar to negative *z*-values. Due to this rotation a displacement of the core-magnetization at the top and bottom end of the wire in the opposite direction takes place. The jump at a field value of -84 kA/m corresponds to the field in applied in the negative direction. After saturation perpendicular to the wire [right panel in Fig.6.14(a)], the magnetization in the central part of the nanopilar aligns with its easy axis, which is observed as a remarkable step in the *M(H)* curve. Nevertheless, at the edges of the wire the moments are still rotated towards the field direction. Reducing the field further leads to a stronger alignment of the moments with the wire-axis, and finally, to zero magnetization at remanence. Here, similar to the parallel case, the magnetization in the center of the wire is aligned along the easy axes, whereas curling of the moments is observed at both ends of the wire. At negative field values the moments tend to align with the applied field until completion of the reversal. Thus, in this case we obtain almost a rotational cycle corresponding to the magnetization going from perpendicular to the nanowire direction to that of the parallel and again to the perpendicular but in the opposite direction.

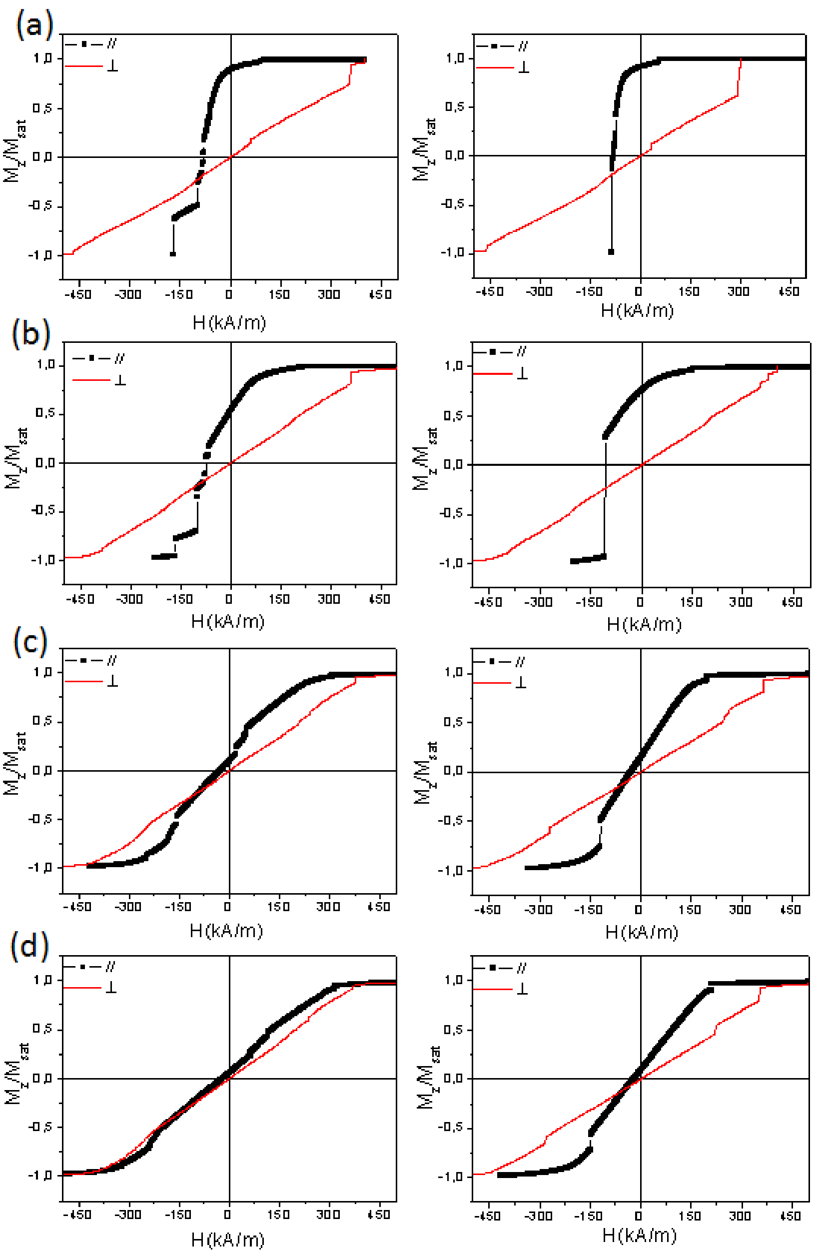

Fig. 6.13. Simulated parallel and perpendicular descending hysteresis branchs for Co nanopillars with diameter of a) 35 nm, b) 44 nm, c) 63 nm and d) 75 nm. The results for arrays of seven nanopillars and isolated nanopillars are presented in the left and right columns, respectively. The simulations were done without internal anisotropy.

In [Fig.6.14(b), left panel], the parallel demagnetization for the nanopillar with *D* of 44 nm is shown. The remanent state is very similar to the case of *D* = 35 nm. Again, in the central part of the pillar the moments are aligned along the wire axis, whereas a vortex-like structure is created at both ends of the wire. However, is remarkable that in this particular case the chirality of both vortices is different. This opposed sense of rotation leads to a *c*-like structure of the magnetization at the outer shell of the wire, which stays in contrast to a more *s*-like state observed for the case discussed above.

Also the perpendicular demagnetization for this nanopillar [Fig.6.14(b), right panel], is comparable to the one with diameter of 35 nm. Decreasing the field from perpendicular saturation, magnetization changes step-wise to a state where the moments align with easy axes of the pillar (*z* direction). Then, a change of the magnetization into a vortex-state can be observed with nucleation field of about 190 kA/m. After nucleation, the core moves within the nanowire perpendicular to the applied field until it annihilates at a field of about -210 kA/m. The movement of the core is a reversible process, which is reflected in the closed central part of the hysteresis. At, remanence, the core is in the center of the nanopillar and thus yields zero magnetization contribution perpendicular to the wire axis *(x-y*-plane). After annihilation, the reversal continues in the same manner as for the wire with 35 nm diameter.

As in the previous parallel cases, for D=63 nm we observe in [Fig.6.14(c), left panel], that two vortices are created at both ends of the nanopillar, and the central part of the magnetization is aligned along of the field direction. One should note that here the chiralities of both vortices are the same. In remanence, the vortex state expands over the entire wire. At the field of -120 kA/m first the core reverses followed by the shell which can be observed by the jump in the hysteresis. The perpendicular case (right panel of the same figure) is comparable with the nanopillar with diameter of 44 nm. Also here, the reversal process takes place by nucleation and annihilation of vortex, with the corresponding field values of 272 and -357 kA/m, respectively. Apparently, the vortex state becomes stabilized by increasing the diameter.

Finally, for the nanopillar with 75 nm of diameter (not shown) the reversal processes for both, parallel and perpendicular geometry are the same as for the wire with 63 nm of diameter. In the parallel case, the nucleation field is about 100 kA/m and the annihilation field is about -348 kA/m, whereby, in the perpendicular case the values are 294 kA/m and -362 kA/m, respectively.

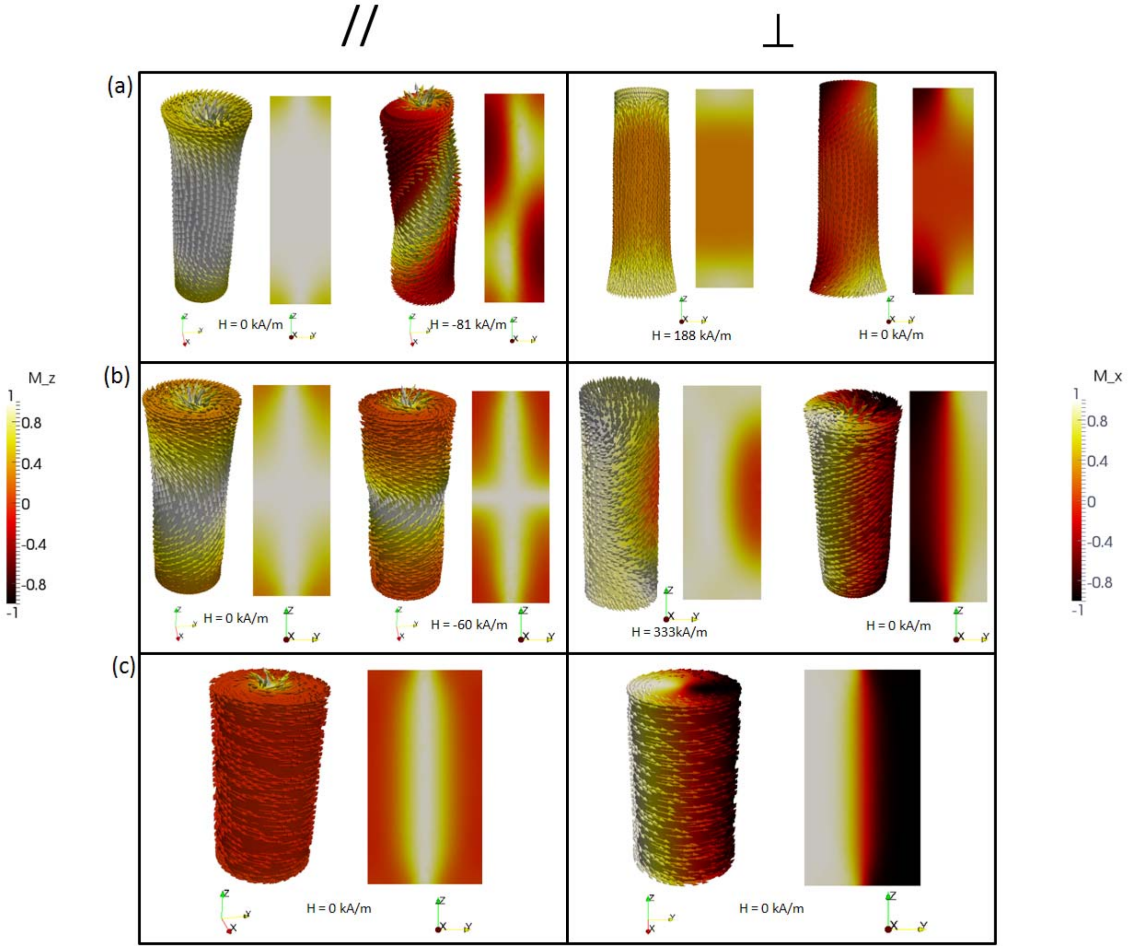

Fig. 6.14. Images of the magnetization distribution at different applied fields for corresponding demagnetization processes of the hysteresis branches for isolated nanopillars in Fig.6.13. The left column (// demagnetization) collects the images of the longitudinal magnetization, M_z, value, while the right column (⊥ demagnetization) collects the images for the in plane magnetization, M_x, value. In the panels the arrows schematically indicate the magnetization direction and the slices are of the cross-section of the nanopillars. The simulation presented here are for diameters of (a) 35 nm, (b) 44 nm and (c) 63 nm.

6.7.2. Magnetic reversal process for nanopillars with different magnetocrystalline anisotropy

The effect of the crystal properties when the diameter *D* was increased from 35 nm to 75 nm, was experimentally investigated showing a strong difference in structural properties which are correlated with magnetic properties. In brief, the crystallographic results show that one obtains the *fcc* crystal Co-phase for Co nanopillars with *D* ~ 35 nm, whereas the *hcp* phase is the only detected in the X-ray reflection patterns when *D* is increased. Besides, the orientation of the crystal hexagonal *c*-axis has been found to change from parallel (*D* ~ 44 nm) to perpendicular to the wire axis (44 nm < *D* ~ 75 nm). When measuring the magnetic properties it was found that both parallel coercivity and parallel remanence decreases as the pillar diameter increases, except for the case of *D* ~ 44 nm. While such reduction is expected in the magnetic parameters due to the increasing role of the magnetostatic interactions among the nanopillars, the magnetic results need to be understood in the light of the crystallographic properties. In the following simulations, a particular crystal contribution for each diameter value, which may represent the experimental anisotropy was considered. For the case of *D* ~ 35 nm it has been considered that the crystal anisotropy present is just the corresponding to the (111) peak of the *fcc* phase. For *D* ~ 75 nm, just the contribution of the (100) *hcp* peak was taken into account. However, it should be mentioned that none of these nanopillars are single crystal or at least, with the crystalinity results presented here, it is not possible to argue such a thing. Hence, some contribution from other peaks that in these measurement were not possible to detect cannot be neglected. Further electron transmission microscopy measurements are recommended in order to investigate this. For the cases in between of the above diameter values, i.e., *D* ~ 44 nm and *D* ~ 63 nm, it was necessary to quantitatively investigate the degree of preferred orientations in the crystallographic results, this is, the texture coefficients (TC) of the *hcp* phase reflections, which were calculated using the following equation:[16]

$$TC(hkl)_i = \frac{I(hkl)_i/I_o(hkl)_i}{\frac{1}{N}\sum_n \frac{I(hkl)_i}{I_o(hkl)_i}}, \tag{6.9}$$

where $I(hkl)_i$ is the observed intensity of the $(hkl)_i$ plane, $I_o(hkl)_i$ is the intensity of the $(hkl)_i$ reflection of a polycrystalline sample, N is the total number of reflections taken into account, and (*hkl*) denotes the Miller indices of the lattice planes of a given signal. TC values larger than 1 indicate a preferred orientation of the crystals/grains in the samples. The maximum value of TC is defined by N. The calculated results are presented in Table 6.2. With these values, the percentage of grains with corresponding crystallographic orientation were estimated and used for the definition of the crystalline anisotropy in the simulations. Table 6.3 resumes the internal anisotropy selected for each simulated case. Thus, in the simulations we assume a granular structure for D= 44 and D = 63 nm.

Table 6.2. Texture coefficients of (100) and (002) planes for *hcp* Co.

D (nm)	TC_{100}	TC_{002}
44	0.4	1.6
63	1.5	0.5

Table 6.3. Different internal anisotropy for the simulated nanopillars as a function of the pore diameter.

D (nm)	*Crystal anisotropy*
35	*fcc* (111) peak
44	80% grains of *hcp* (002) peak and 20% of hcp (100) peak
63	25% grains of *hcp* (002) peak and 75% of *hcp* (100) peak
75	*hcp* (100) peak

Figure 6.15 collects the experimental hysteresis loops of the Co nanopillars in both parallel and perpendicular configuration of the applied magnetic field with the respective simulated *M(H)* curve. Fig. 6.16 shows the corresponding images of the magnetization distribution during the reversal process of the simulated curves for isolated nanopillars. In the following the micromagnetic results will be discussed. As in the previous subsection, see the *M(H)* curves in Fig.6.15 when it is required in the discussion below. For the comparison between experimental and theoretical results we should note that modelling results have abrupt jumps on the loops. In reality, interactions between nanowires, imperfections and distribution of properties smoothen and average over many nanowires the observed behavior.

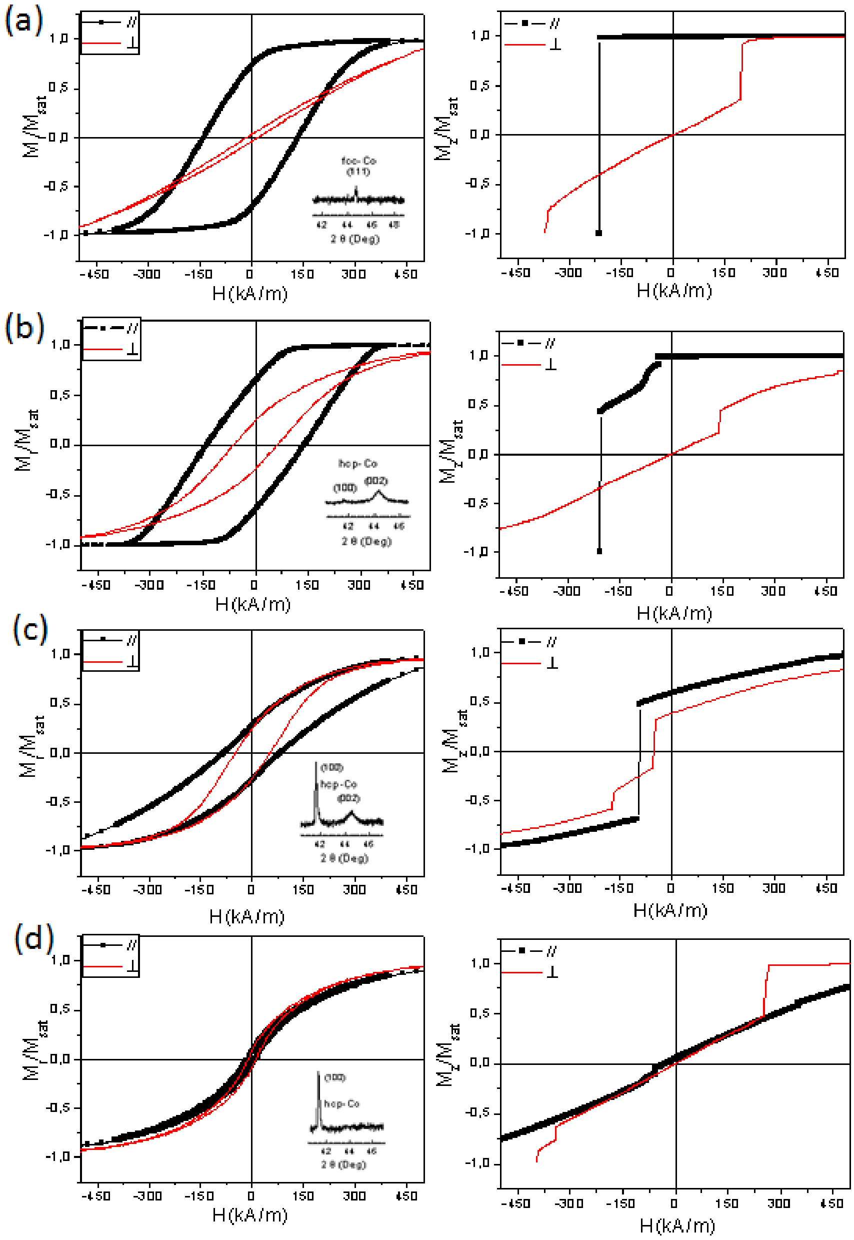

Fig. 6.15. *M(H)* curves for individual Co nanopillars with the applied field parallel and perpendicular to the nanopillars axes. The results for experimental hysteresis loops are presented in the left column, where the insets are the XRD patterns for the respective sampe (see also Section 3.5.2). In the right column the simulation results are collected, where different crystal anisotropy, depending on the pore diameter of the nanopillars: (a) 35 nm, (b) 44 nm, (c) 63 nm and (d) 75 nm. This crystal anisotropy was determined taking into account the experimental XRD results.

Considering the case of D = 35 nm with a parallel applied field (which actually was already discussed in the Section 6.4), the simulated nanopillar with *fcc* phase is almost saturated at remanent state [Fig. 6.16 (a), left panel] and two vortices at the opposite ends are formed. Then, the reversal process proceeds in a single quasi-curling step leading to a nearly square loop with a single jump. In the perpendicular reversal

[Fig. 6.16 (a), right panel], with decreasing magnetic field the magnetic moments at both ends of the pillar tend to align along the *z* direction. Decreasing the field further, also the other moments align with the pillar-axis until at remanence the pillar is almost magnetized along the z direction. By application of a negative field, after reversing the field direction, the demagnetisation also starts at the ends of the pillar.

For of D = 44 nm [Fig. 6.16 (b)], during the parallel demagnetization process it is observed that the magnetization in the top part of the nanopillar is aligned within the field direction, while, at the bottom a vortex is created. This has to be compared to the case without anisotropy, where, vortices were formed at both ends of the wire. Most probably, this happened due to the introduction of the granular structure which leads to the non-equivalence of the nanopillar ends. With decreasing magnetic field the thickness of the vortex increases and expands over the entire pillar. Finally, at a field of -205 kA/m the complete pillar reverses and magnetizes along $-z$ direction, which is manifested in the jump in the *M(H)* curve. Consequently, in the perpendicular case, first, the top part of the nanopillar (with higher anisotropy in the pillar direction) becomes magnetized along the pillar axis, whereas, the bottom part remains aligned perpendicular. Rotation of the latter occurs at 139 kA/m (which can be seen in the jump in the hysteresis) and yields the remanent magnetization state, where nearly all moments are aligned in the *z*-direction. At negative fields, the reversal is completed by first, alignment of the bottom part and second, of the top part of the wire perpendicular to the pillar axis. Note that this situation corresponds to a particular realization of the granular structure. To get a more realistic hysteresis cycle, the averaging over many disorder realizations should be performed.

The parallel case for the nanopillar with 63 nm diameter [Fig. 6.16 (c)] is comparable to that with 44 nm diameter. Again, a vortex with core magnetization parallel to the pillar axis emerges at one end of the pillar (top) and increases in thickness. At a field of -94 kA/m, the lower part of the pillar together with the core of the vortex undergoes a direct reversal, which is pronounced in a significant jump in the corresponding *M(H)* curve. In the top part of the pillar, however, the vortex structure still remains until the reversal completes at higher negative field values. The reversal process of the perpendicular case is governed by nucleation and annihilation of an in-plane vortex, which is characterized by a core-axis perpendicular to the pillar-axis. The vortex nucleates at positive field values at the bottom end and moves through the pillar with decreasing magnetic field. However, at field of -50 kA/m, corresponding to the first jump in the *M(H)* curve, a second vortex is created [Fig. 6.16(c), right panel], at the bottom end and pushes the first to the top end of the pillar. The second jump, at -169 kA/m corresponds to the annihilation of the first vortex resulting in the reversal of the bottom end of the wire. The reversal process is completed by the movement of the second vortex and annihilation at the bottom end of the wire. Again, complete analysis should involve the averaging over many disorder realizations.

Finally, considering the sample with *D* = 75 nm [Fig. 6.16 (d)], for both, parallel and perpendicular geometry, a rather complex reversal process is found. In the parallel case, first two vortices are created at both ends of the wire, as it was observed for the cases discussed above, with an opposed chirality of the vortices. Reducing the field further, the moments in the central part of the sample align perpendicularly to the pillar axis. However, two small areas on the shell of the pillar still remain magnetized in *z*-direction. At the remanent state, two channels emerge connecting the cores of the vortices with these two spots on the shell. Then, at higher negative fields, first, these two channels reverse before the residual parts of the pillar rotate with negative field direction. In the case of the field applied perpendicular to the pillar-axis, an out-of-plane vortex is created at a field of 255 kA/m, which is pronounced in an abrupt change of the magnetization on the *M(H)* curve. Decreasing the field, the movement of the vortex through the pillar reverses the magnetization until it annihilates at a field of -340 kA/m, which is pronounced in the second jump in the *M(H)* curve. However, as it is observed in Fig. 6.16 (d), right panel, a small part of the shell remains magnetized in positive *x*-direction until it switches at a field of -392 kA/m and, thus, completes the reversal of the pillar.

As it has been already mentioned, a complete comparison with the experimental results requires more extensive calculations using an array of nanowires and averaging over different realizations of the granular structure. Nevertheless, a general tendency towards the agreement with the experiment can be already captured in Fig. 6.15. Both modeling and experiment show crucial changes of hysteresis loops when the diameter is increased, related to the changes of both magnetocrystalline and shape anisotropies. Indeed, it is observed a systematic decrement of the parallel coercivity and practically the same hysteresis loops for parallel and perpendicular configurations for the largest diameter D = 75nm. Compared to the case of the shape anisotropy only (where all perpendicular loops had zero remanence), an experimentally observed non-zero perpendicular remanence for D = 63 nm is qualitatively reproduced. The latter should be attributed to the influence of crystallographic changes.

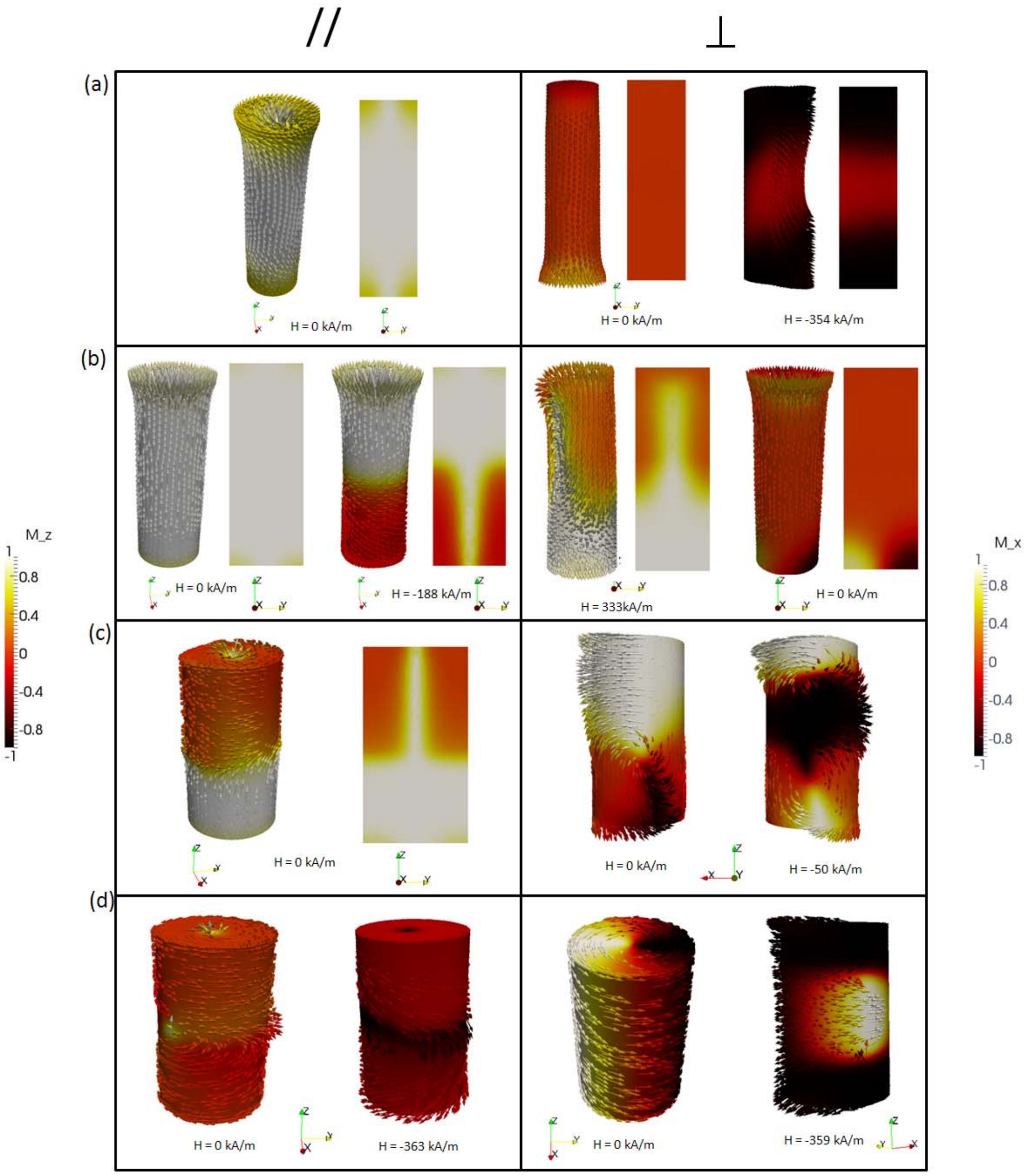

Fig. 6.16. Images of the magnetization distribution at different applied fields for corresponding demagnetization processes of the hysteresis branches for isolated nanopillars in Fig.6.15. The left column (// demagnetization) collects the images of the longitudinal magnetization, M_z, value, while the right column (⊥ demagnetization) collects the images for the in plane magnetization, M_x, value. In the panels the arrows schematically indicate the magnetization direction and the slices are of the cross-section of the nanopillars. The simulation presented here are for diameters of (a) 35 nm, (b) 44 nm, (c) 63 nm and (d) 75 nm.

6.8. Summary

Micromagnetic simulations of magnetization reversal of various Co nanowires with different aspect ratios (from 120 to 1000 nm in length, and 35 to 75 nm diameter) were performed.

The measured aspect ratio dependent coercivity of ordered Co nanowires is interpreted considering the change of preferred crystalline structure from *fcc* cubic to *hcp* hexagonal in small and high aspect ratio nanowires, respectively. The measured coercivity values are in agreement with the micromagnetic simulations, accordingly. The key to the control of the coercivity thus resigns in the control of the crystallographic orientation of easy axis together with the nanowire aspect ratio.

Different complex reversal modes are obtained in micromagnetic simulations, depending on the geometry dimensions and the crystallographic structure. The simulations show that the hysteresis process in almost all nanowires involves the formation of the vortex. For long *hcp* nanowires with perpendicular *c*-axis, it is report the formation of central vortex which extends along its whole length at the remanence. The demagnetization proceeds with the reversible rotation of its shell and the consequent irreversible switching of the core.

6.9. References

[1] F. Zighem,T. Maurer, F. Ott, and G. Chaboussant, J. Appl. Phys.,**109**, 013910 (2011).

[2] X. Han, Q. Liu, J. Wang, S. Li, Y. Ren, R. Liu and F. Li, J. Phys. D: Appl. Phys. **42,** 095005, (2009).

[3] R. Hertel and H. Kronmüller, Phys. Rev. B **60**, 7366 (1999).

[4] W. Scholz, J. Fidler, T. Schrefl, D. Suess, R. Dittrich, H. Forster, and V. Tsiantos, Comput. Mater. Sci. **28**, 366 (2003)

[5] T.R. Koehler, D.R. Fredkin, IEEE Trans. Magn. **27**, 4763 (1991).

[6] R. Hertel and J.Kirschner, Physica B **343**, 206 (2004).

[7] Y. Henry, K. Ounadjela, L. Piraux, S. Dubois, J.-M. George, and J.-L. Duvail, Eur. Phys. J. B **20**, 35 (2001).

[8] M. Darques, A. Encinas, L. Vila, and L. Piraux, J. Phys. D, Appl. Phys. **37**, 1411 (2004).

[9] C. J. García-Cervera, Z. Gimbutas, E. Weinan J. Comp. Phys. **184**, 37 (2003).

[10] R. Hertel, J. Magn. Magn. Mater. **249**, 251 (2002).

[9] F. Zighem, T. Maurer, F. Ott, and G. Chaboussant, J. Appl. Phys. **109**, 013910 (2011).

[10] H. Zeng, M. Zheng, R. Skomski, and D. J. Sellmyer, J. Appl. Phys. **87**, 4718 (2000).

[11] R. Skomski, H. Zeng, M. Zheng, and D. J. Sellmyer, Phys. Rev. B **62**, 3900 (2000).

[12] K. R. Pirota, F. Béron, D. Zanchet, T. C. R. Rocha, D. Navas, J. Torrejón, M. Vazquez, and M. Knobel, J. Appl. Phys. **109**, 083919 (2011).

[13] H. Forster, T. Schrefl, W. Scholz, D. Suess, V. Tsiantos, J. Fidler, J. Magn. Magn. Mater., **249**, 181 (2002).

[14] X. Kou , X. Fan , R. K. Dumas , Q. Lu , Y. Zhang , H. Zhu , X. Zhang , K. Liu , and J. Q. Xiao, Adv. Mater., **23**, 1393(2011).

[15] W. Scholz, K.Yu. Guslienko, V. Novosad, D. Suess, T. Schrefl, R.W. Chantrell, J. Fidler, J. Magn. Magn. Mater., 266, 155 (2003).

[16] F. Maurer, J. Bröetz, S. Karim, M.E. Toimil-Molares, C. Trautmann, H. Fuess, Nanotechnology **18**, 135709 (2007).

Conclusions and Outlook

The objective of this work has been to emphasize the role played by crystalline energy term which is particularly relevant for the magnetization process of Co and Co-base nanowire arrays. From the present study, it can be concluded that:

(i) The dimensions (i.e. length and diameter) of Co nanowires modify the crystalline structure of nanowires. Particularly, for short electroplating time (i.e. reduced length of nanowires) or small diameters, *fcc*-crystal phase is dominant which together with shape anisotropy usually results in longitudinal magnetization easy axis. For longer electroplating time (i.e. longer nanowires) or bigger diameters, *hcp*-crystal phase is formed which determines the appearance of a magnetocrystalline anisotropy nearly at transverse orientation. In this case, a competition between shape and crystalline anisotropy is observed.

(ii) The crystalline structure of electrodeposited Co nanowire arrays and its texture can be tailored by the synthesis process (i.e, pH of the electrolytical bath and plating time).

(iii) An alternative way to tune the magnetic anisotropy without extreme changes in saturation magnetic moment is through the addition of other metallic elements. In this work, it has been paid attention to elements such as Ni and Pd. Particularly in the case of CoNi nanowires, it is concluded that the presence of Ni continuously shift the effective magnetocrystalline anisotropy, originating changes in remanence and corcivity. This effect is even more pronounced in the case of CoPd nanowires but just for small quantities of Pd.

(iv) Temperature is also an important parameter that modifies the effective magnetic anisotropy. Significant reduction of temperature induces changes of magnetoelastic anisotropy owing to stresses induced by thermal strains. That adds to the temperature increase of magnetocrystalline anisotropy energy and in some particular case can lead to change in sign of magnetization easy axis from longitudinal to in-plane of the array.

(v) An analysis of the background in micromagnetism leads to presume a magnetization reversal by magnetization rotation by curling mode. Nevertheless, experimental results together with micromagnetic modelling suggest more complex mechanisms involving magnetization curling (vortex-like) and/or transverse domain wall modes depending on strength and orientation of crystalline anisotropy.

Even though a reasonable set of experiments and modelling trials have been collected, there is still place for further studies to finally unveil the complete reversal mechanism of Co-base nanowire arrays.

Current challenges regarding research on nanowires involve a wide range of topics from semiconductor to biological or energy novel devices. For magnetic nanowire arrays, very new perspectives are being opened with regards to their functionalizing making use of their ferromagnetic character in electromagnetic actuators, biomagnetic patterning and separation or microwave electronics. More specifically, arrays of magnetic nanowires with controlled magnetic response offer quite novel perspectives in future 3D logic devices where knowledge of fundamental domain wall motion is essential. In this regard tailoring the magnetic anisotropy (e.g. longitudinally modulated and multilayered) of individual nanowires together with their interactions plays the essential role. While shape anisotropy is present in all nanowires, magnetic behaviour particularly magnetization reversal and its dynamics process can be further controlled in nanowires with specific crystalline structure.

Conclusiones

El objetivo de este trabajo se ha centrado en estudiar el papel que desempeña la energía cristalina, la cual es determinante en el proceso de inversión de la imanación de nanohilos de Co y nanohilos de aleaciones basadas en Co. Del presente estudio se puede concluir en términos generales lo siguiente:

(i) Las dimensiones geométricas como el diámetro y la longitude los los nanohilos de Co, modifican su estructura cristalina. Particularmente, para tiempos cortos de electrodeposición (nanohilos con longitudes cortas) o para diámetros de poros del orden de 35 nm, la fase cristalina dominante es la *fcc* del Co, la cual sumada con la anisotropía de forma del sistema, resultan en una anisotropía magnética axial. Para tiempos mayores de electrodeposición, es decir, longitudes mayores de nanohilos ó diámetros por encima de los 44 nm, la estructura cristalina dominante en el sistema es la *hcp*, la cual resulta en una anisotropía cristalina con orientación transversal a los nanohilos. En este caso, se da una competición entre las anisotropías de forma y cristalina.

(ii) La estructura cristalina junto con la textura de los nanohilos de Co puede optimizarse en aras de una anisotropía efectiva longitudinal, mediante el proceso de síntesis de los nanohilos. En particular, aquí se ha mostrado el papel que desenvuelven el pH del electrolito usado para la electrodeposición y el tiempo de electrodeposición.

(iii) Las propiedades magnetocristalinas del Co pueden modificarse (sin cambiar significatiamente propiedades como el momento de saturación magnético), a través de la inclusión de elementos como el Ni y el Pd mediante una aleacón con Co. En el caso de alecaiones CoNi, se concluye que la presencia del Ni favorece que la estructura cristalina esté dominada por la fase *fcc* del Co y del Ni. Esto origina cambios significativos en los parámetros magnéticos como la remanencia y el campo coercitivo. En el caso de la aleación de de

CoPd se observan resultados similares pero solo para cantidades reducidas de Pd en la aleación.

(vi) La temperatura es un parámetro fundamental que puede modificar la anisotropía efectiva. En general, a bajas temperturas se observan cambios significativos debido al efecto de estrés térmico en la anisotropía magnetoelástica. Por otro lado, Para nanohilos de Co y de aleaciones ricas en Co, con bajo coeficiente de magnetostricción, el efecto de la anisotropía magnetocristalina puede verse reflejado en un cambio de signo del eje fácil de imanación a bajas temperaturas.

(vii) El analsis micromagnético del mecanismo de inversion de la imanación basado en los resultados experimentales obtenidos revela que la inversión magnética en estos sistemas puede involucrar mecanismos tipo vórtice y de movimiento transversal de paredes dependiendo de la orientación de la anisotropía cristalina en el Co y sus aleaciones.

A pesar de que un conjunto razonable de experimentos y pruebas de modelos han sido realizados en este trabajo, se requieren estudios posteriores para entender de forma totalmente precisa el mecanismo de reversión de la imanación en los arreglos de nanohilos magnéticos de Co.

Los retos actuales en materia de investigación en nanohilos implican a una amplia gama de temas, desde los semiconductores hasta nuevos dispositivos biológicos o de energía. Para los arreglos de nanohilos magnéticos existen perspectivas muy nuevas y prometedoras en lo que respecta a la funcionalización de su carácter ferromagnético en la biomedicina y la electrónica de microondas, por ejemplo. Más específicamente, los arreglos de nanohilos magnéticos con una respuesta magnética controlada ofrecen perspectivas muy novedosas en el futuro los dispositivos de lógica en 3D donde el conocimiento del movimiento fundamental de la pared de dominio es esencial. En este sentido la adaptación de la anisotropía magnética (por ejemplo, longitudinalmente, modulada y de varias capas) de nanohilos individuales, junto con sus interacciones juegan un papel esencial. Mientras que la anisotropía forma está presente en todos los nanohilos, el comportamiento magnético de inversión de la imanación en particular y el proceso de su dinámica puede ser más controlado y optimizado a través del control en la específica estructura cristalina requerida según la aplicación de interés.

List of publications

W. O. Rosa, L. G. Vivas, K. R. Pirota, A. Asenjo and M. Vázquez,
“Influence of aspect ratio and anisotropy distribution in ordered CoNi nanowire arrays”
J. Magn. Magn. Mater. (Accepted).

L. G. Vivas, M. Vázquez, J. Escrig, S. Allende, D. Altbir, D. C. Leitao, and J. P. Araujo,
“Magnetic anisotropy in CoNi nanowire arrays: Analytical calculations and experiments"
Phys. Rev. B, 85, 035439 (2012).

L. G. Vivas, M. Vázquez, V. Vega, J. García, W.O. Rosa, R. P. del Real and V. M. Prida,
“Temperature dependent magnetization in Co-base nanowire arrays: Role of crystalline anisotropy "
J. Appl. Phys.,111, 07A325 (2012).

V. Vega, J. Garca, W.O. Rosa, L. G. Vivas, V. M. Prida, B. Hernando and M. Vázquez,
“Magnetic properties of (Fe,Co)-Pd nanowire arrays "
J. Nanosci. Nanotechnol. (In press).

L. G. Vivas, R. Yanes, O. Chubykalo-Fesenko, and M. Vázquez,
“Coercivity of ordered arrays of magnetic Co nanowires with controlled variable lengths "
Appl. Phys. Lett., 98, 232507 (2011).

M. Vázquez and L. G. Vivas,

“Magnetization reversal in Co-base nanowire arrays "

Phys. Status Solidi B, 248, 2368 (2011).

Agradecimientos

Quiero agradecer a mis directores de tesis Manuel Váquez y Oksana Fesenko por su valiosa e importante guía en estos 4 años y por su incondicional apoyo y amistad.

De manera muy especial también quiero agradecer a mi tutor Dr. Juan José de Miguel y a los miembros del tribunal Dr. José Rivas, Dr. Victor de la Prida, Dr. Agustina Asenjo, Dr. Rafael Pérez, Dr. Joao Pedro Araújo, Dr. Julio Camarero, y al Dr. David Navas.

A los que han sido mis compañeros de grupo y amigos: Karla, Alejandro, Alfredo, Germán, Wagner, Miriam, Mariana, Rhymo, Nacho, Cristina, Oscar, Unai, Pablo, Yurii, Rocío, David y, en Oviedo a Victor y Javi. Muchas gracias al Dr. Giovanni Badini y a la Dr. Diana Leitao por todo su apoyo y lo que me han enseñado este tiempo.

Estos 4 años han sido muy divertidos gracias a Bernd, Leti, Belén, Inma, Javi P., Alex, Fernando, Ana, Stefi, María, Carlos, Gladys, El Paisa, Ivan, Coba, Matias y al grupo itinerante de la comida liderado por Alvaro e Iñigo.

Finalmente quiero agradecer a Valeria, Camilo Alejandro, Lorena, María del Carmen y a Camilo por estar siempre allí.